

Second Harmonic Generation from Antiferromagnetic Interfaces

Dissertation

zur Erlangung des akademischen Grades
doctor rerum naturalium (Dr. rer. nat.)

vorgelegt der

Mathematisch-Naturwissenschaftlich-Technischen Fakultät
(Mathematisch-Naturwissenschaftlicher Bereich)
der Martin-Luther-Universität Halle-Wittenberg

von

Dipl. Ing. Mikołaj Trzeciecki
geb. am 06.02.1974 in Warszawa

Gutachter:

1. Prof. Dr. J. Kirschner
2. Prof. Dr. S. Trimper
3. Dr. hab. L. Adamowicz

Halle a.d. Saale, den 10. März 2000

Tag der mündlichen Prüfung: 10. Juli 2000

This work has been done at the Max-Planck-Institute of Microstructure Physics in Halle, Germany, with the partial financial support of the Institute of Physics at the Warsaw University of Technology, Poland.

Contents

1	Introduction	3
1.1	Oxides and Their Interfaces	3
1.2	Second Harmonic Generation	5
1.3	The Scope of this Work	6
2	Symmetry Analysis	8
2.1	State of the Art	9
2.2	Basic Principles of the Symmetry Analysis	10
2.2.1	Nonvanishing Tensor Elements	11
2.2.2	Reversal of the Order Parameter	15
2.3	Results of the Group Theoretical Analysis	17
2.3.1	“The Table” and How to Read It	17
2.3.2	Case A: Equivalent Atoms	24
2.3.3	Case B: Distortions of Monoatomic Lattice	28
2.3.4	Case C: Structure with Nonequivalent Magnetic Atoms	30
2.3.5	Case D: Distorted Oxygen Sublattice	33
2.3.6	Second Atomic Layer	36
2.3.7	Domain Imaging	40
2.3.8	Possible Experimental Results	42
2.4	Time Reversal	46
2.4.1	Conventional Approach	47
2.4.2	Dissipation in SHG	47
2.4.3	Spatial Operations	50
2.4.4	Practical Implications	51
3	Electronic Theory	54
3.1	Interplay of Symmetry and Electronic Theory	54
3.1.1	The Paramagnetic Phase	55
3.1.2	The Ferromagnetic Phase	56
3.1.3	The Antiferromagnetic Phase	56
3.2	The Hamiltonian	57
3.2.1	Two Holes	59
3.2.2	Three and Four Holes	60
3.2.3	Bulk vs. Surface of NiO	61

3.3	The Nonlinear Spectrum of NiO (001)	64
3.4	Spin and Charge Dynamics	66
3.4.1	Treatment of Pump-Probe Experiments	67
3.4.2	Relaxation of Excited States	68
4	Conclusions and Outlook	71
A	Tables	73

Chapter 1

Introduction

1.1 Oxides and Their Interfaces

From the very advent of human civilization people were dealing with metal oxides. They were admiring the beautiful green color of old copper roofs, fighting against rust on their kettles and swords, attributing magic powers to noble metals since they never oxidize. Ancient Chinese were using magnetite to orientate their boats on high seas, while medieval Europeans were using various metal oxides to illuminate¹ their books. During the past decades of investigation, the research mainly focused on the structural and electronic properties of bulk oxides. The problems of strong electronic correlations have attracted theoreticians towards magnetic oxides already in the 1960's. This investigation resulted in creating theoretical models which describe the ground state of these materials properly (e.g. the Hubbard model [1]). They have been successfully applied also to another important class of oxides, high- T_c superconductors. However, with the advent of high-fluence lasers, which made nonlinear (magneto-)optics possible [2], the description of non-equilibrium states became necessary. On the other hand, the scientific understanding of oxide *surfaces and interfaces* is still in its infancy, although in the last years many scientific programs have been launched in order to clarify the physics of oxide interfaces.

From the beginning of computer technology, long-term (magnetic) data storage and temporary (semiconductor-based) data storage have existed and have been developed separately. Semiconductor industry has been able to fit more and more transistors onto a silicon chip while magnetic-recording industry has been shrinking the size of the reading head, increasing the storage density. Nowadays, the demands of the market seemingly push these two areas together: there is a need for nonvolatile memory chips where the information remains stored even after switching the computer off, and on the other hand the need for the speed of the storage devices may eventually eliminate the designs which rely on the mechanical motion of the elements (like currently used hard disk drives) [3]. The field which marries the two hitherto separate areas is magnetoelectronics, and the devices which are supposed to supersede the conventional random access memories and hard disks are Magnetic Random Access Memories (MRAMs).

¹Illumination is a medieval book illustration in various shades of red.

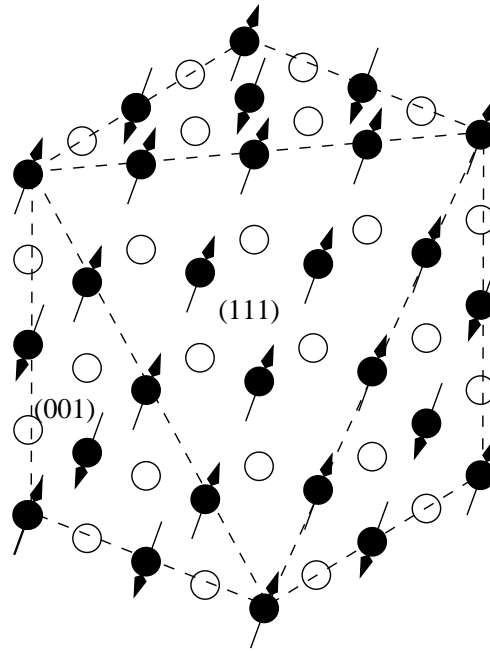


Figure 1: Surfaces of the cubic antiferromagnet NiO.

One of the most important components of the designed MRAMs are tunneling magnetoresistance (TMR) devices, where the read-out current passing through the device depends on the relative magnetization of two ferromagnetic layers. The central layer of this trilayer structure consists of an oxide sandwiched between a soft and a hard magnetic layer². For these technological applications it is necessary to develop a technique to study buried oxide interfaces. Already the preparation of transition-metal oxides is a challenge and requires a method to characterize the structure and magnetism of these materials. Such a technique can be optical second harmonic generation (SHG), which is easy to implement, sensitive to antiferromagnetism and addresses surfaces and interfaces of materials which possess central symmetry. One of the most favored antiferromagnets is nickel oxide (NiO), which is a prototypic system for strong electronic correlations and has a simple crystallographic rock-salt structure (see Fig. 1). However, this material is not easily accessible for the experimental study, since it cannot be grown on nickel due to a large lattice mismatch (20%). To the best of our knowledge, the understanding of its detailed spin structure is scarce - even the spin orientation on the ferromagnetically ordered and antiferromagnetically coupled (111) planes³ are not known. The technique presented in this work can shed some light on that issue, and answer some other important questions related to antiferromagnetic oxide interfaces.

²These two layers are often composed from the same material but of different thicknesses.

³Neither the detailed interatomic distances.

1.2 Second Harmonic Generation

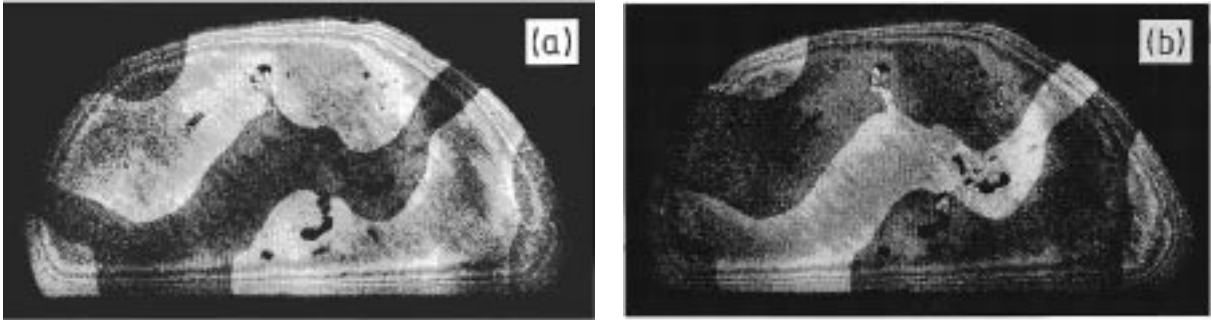


Figure 2: Bulk AF domain imaging by Fiebig *et al.* [4]. Images taken with right (a) and left (b) circularly polarized light.

As stated before, SHG has the unique potential to become a tool for investigating buried oxide interfaces, where other techniques fail. Until now, it has been proven to be a very useful technique for the investigation of ferromagnetism at surfaces. The obvious question is if this technique can also yield some new information in the case of more general spin configurations, such as antiferromagnetic (AF) ordering at interfaces. An experimental answer to this question has been provided by Fiebig *et al.* [4, 5], who obtained a pronounced optical contrast from AF 180° domains of *rhombohedral* bulk Cr_2O_3 . This experiment, which is of great significance for us, will be described later in detail (page 9). Since it is known that, in *cubic* materials, within the electric dipole approximation, optical SHG originates only from surfaces, interfaces, or thin films, an important question is if SHG is also sensitive to antiferromagnetism at surfaces of cubic antiferromagnets.

Experimental techniques for the detection of AF domain *walls* using linear optics in some special geometries were elaborated already in the 1950's [6]. The *interior* of the domains has been visualized in piezoelectric AF crystals using a linear magneto-optical effect [7]. However, linear optical experiments suffer from mixing the desired signal with a contribution from other linear effects, such as birefringence or dichroism. A review of linear optical experimental methods for the investigation of AF domains is given by Dillon [8]. Only neutron diffraction [9] and x-ray crystallography⁴ techniques and SHG are able to address the balanced spin structures. All other techniques are not conclusive, for instance the linear dichroism [10] couples to the order parameter squared and consequently cannot distinguish antiferromagnetism from ferromagnetism.

The observation of the domain structure in antiferromagnets is more complicated than in ferromagnetic materials since the reduction of the spatial symmetry in the antiferromagnetic phase is, unlike for ferromagnets, not linked to an imbalance in the occupation of majority and minority spin states.

⁴X-ray crystallography addresses the structural properties of the sample. In antiferromagnets, it detects the unit-cell doubling rather than antiferromagnetism, and thus it fails in materials like Cr_2O_3 .

Nonlinear optics exhibits an additional degree of freedom, since its elementary process involves three photons instead of two in linear optics. For that reason, some authors, e.g. Fröhlich [11] suggested the application of nonlinear optics even for k-selective spectroscopy, since multi-photon phenomena allow for the “scanning” of a small part of the Brillouin zone, at least for semiconductors. Recently, non-linear optics has attracted more and more attention to the investigation of magnetism due to its enhanced sensitivity to twodimensional *ferromagnetism* [12, 13]. The magnetic effects are usually much stronger than in linear optics (rotations up to 90° , pronounced spin-polarized quantum well state oscillations [14, 15], magnetic contrasts close to 100%) [16, 17]. An example of ferromagnetic effects measurable *only* by SHG deals with the existence of surface magnetism in very thin films of Fe/Cu(001) and is given in Ref. [18]. Nonlinear optical effects were invoked to investigate high temperature superconductors [19, 20] and to study structures composed from alternately ferro- and antiferromagnetically ordered thin films [21]⁵. SHG in strong magnetic fields has been predicted also in vacuum [22], although the size of the effect is questionable [23]. However, the first experiments concerning the detection of the AF domains in materials such as Cr_2O_3 were carried out only recently [4, 24]. Already in the 1970s, it has been proposed [25] that experimental studies of dc magnetic and electric field-induced SHG could become an effective method of determining the crystal structure of solids, the symmetry of which cannot be investigated by other methods. Extending this idea towards surface crystallography provides us with a new technique for determining the spin configuration in a given surface structure. In turn, it permits to use a known magnetic configuration as a reference system for the determination of the surface structure. All the mentioned information is more difficult or even impossible to obtain in linear optics, and moreover other linear methods like neutron scattering, albeit capable to see AF domains, have difficulties to probe AF spin configurations. In addition, the neutron diffraction suffers from large acquisition times and is therefore not suitable for dynamics.

1.3 The Scope of this Work

The arguments mentioned hitherto suggest that the technique of optical second harmonic generation (SHG) will play a key role in the investigation of complicated magnetic sandwich structures. Therefore, our work aims at the theoretical investigation of SHG from antiferromagnetic surfaces and interfaces. The project can be characterized by the following points:

- Symmetry classification. We classify the symmetries of antiferromagnetic surfaces and determine the influence of the symmetries on the nonlinear magneto-optical susceptibility tensor. Using these results we check the possibility of domain imaging. Until now, the group-theoretical classification was devoted to revealing the existing tensor elements for a given symmetry for bulk systems, and without relation to SHG. In the experiment, however, SHG results from the specific tensor elements,

⁵The antiferromagnetic Cr is assumed there to give no contribution to magnetization-induced SHG.

and one often is interested in the particular spin structure rather than the name of the appropriate symmetry group. Our work aims at filling this missing link.

- **Domain imaging.** Closely related to the previous, our work investigates the possibility of domain imaging on antiferromagnetic surfaces. Until now, it has been proven that linear optics cannot yield trustworthy results, and the only other method, neutron scattering, is at least cumbersome in application. Also, the AF bulk domains have been experimentally observed by nonlinear optics. Our work will investigate the conditions under which also the AF surface domains can be imaged in SHG.
- **Spin Reversal.** Until now, the notions of time-reversal and spin-reversal were used indiscriminately in the symmetry analysis. However, in nonlinear optics the applicability of time-reversal is not obvious, on the other hand the spin degree of freedom must show up in the symmetry analysis by space operations. In this work, we propose a consistent description of the dynamic process of SHG and define the notions of reciprocity, time-reversal and moment-reversal for the use in the symmetry analysis of nonlinear optics.
- **Electronic theory.** Based upon the previous points, we will propose a theoretical framework which will allow for the calculation of the nonlinear magneto-optical spectra from antiferromagnetic interfaces. Our theory, aiming at the most general level of description (ability to treat para-, ferro-, and antiferromagnetism on equal footing) will *not* be an *ab initio* theory. Also, ground state features (such as structure optimization) will not be addressed in our approach. However, it successfully identifies the spectral lines favorable for nonlinear optics, and magneto-optics in particular. The theory forms a basis for the description of nearly all elements: only the systems with electronic configuration d^5 and those with f-electrons cannot yet be treated within this framework. The extension of our theory towards d^5 systems is straightforward. The calculations are performed for the NiO (001) surface, but an extension to other AF oxide surfaces is possible.
- **Femtosecond dynamics.** Based on the electronic calculations, we present the results of our simulations of an SHG pump-and-probe experiment. These results concern both spin- and charge-dynamics (dynamics of the antiferromagnetic and paramagnetic tensor elements) and reveal interesting dynamical properties of the antiferromagnetic response within the femtosecond regime.

Chapter 2

Symmetry Analysis

Symmetries determine several important properties of the studied system, they also influence the experimental outcome. In theoretical physics, a proper understanding of the symmetry of the problem considerably reduces the effort to obtain a desired result. For example, a simple symmetry consideration can provide us with the information that two particular quantities are mathematically equivalent, or that a particular value must vanish. Trying to calculate these values without the knowledge obtained from the symmetry analysis one may end up in an unnecessary consumption of the time and effort, or may even prove impossible.

In solid state physics, the symmetries play an especially important role. It is the translational symmetry which allows for a distinction of solids from molecules, for introduction of the reciprocal space and the existence of the band structure. On the other hand, point group symmetries make the difference between molecules and solids on one side, and free atoms and ions on the other.

One determines the symmetry only with respect to an aspect of the investigated object. In the case of this work, we will investigate symmetries of atomic arrangements (along with their magnetic moments) from the geometric and magnetic point of view, while the nuclear forces acting on elementary particles in our systems are not of our interest. For a symmetry to show up, two conditions must be fulfilled [26]:

- An operation, capable of changing the investigated aspect, must be possible to conduct.
- If this operation leaves the investigated aspect of the system invariant, it belongs to the symmetries of the system.

The first point indicates that for a given system under investigation, a reference system must be present which *will not* be immune to the change. In our analysis, such a reference will be the coordinate system in which we describe the surfaces of the crystals. As a consequence, there is no use in investigating, for example, the magnetization-reversal symmetry of paramagnetic systems.

2.1 State of the Art

The first theoretical explanation of *linear* magneto-optic effects in bulk ferromagnets has been given by Argyres [27] in the 50s. He used linear response theory for current-current correlation functions. His microscopic explanation was already based on the combination of spin-orbit and exchange coupling. The application of linear magneto-optics to antiferromagnetism, however, is unsuccessful in all practical cases. An early theoretical work, based on group-theoretical classification, proposed the use of linear optical effects, namely gyrotropic birefringence, for the observation of AF domains related to each other by the space-inversion operation [28]. A theoretical review of the effects found by a group-theoretical approach is presented by Eremenko and Kharchenko [29]. They performed a comprehensive study of linear optical effects for various AF materials. Another effect proposed recently by Dzyaloshinskii *et al.* [30] gives a possibility to detect antiferromagnetism taking advantage from optical path differences from antiferromagnetically coupled but intrinsically ferromagnetic planes, e. g. at (111) surfaces of cubic antiferromagnets.

The literature for *nonlinear* magneto-optics is very rich, both in its theoretical and experimental aspect. However, the applications of nonlinear magneto-optics to antiferromagnetism have not been that numerous so far. One of the first theoretical investigations of the possibility to apply nonlinear optics to *antiferromagnetism* was performed by Kielich and Zawodny [31]. These authors predicted, among other effects, the capability of SHG to determine the crystal structure [25].

The first experimental investigation of SHG from antiferromagnetic oxides was the observation of bulk domains in Cr_2O_3 by the Fröhlich group [5]. They observed that circularly polarized light is absorbed differently in two possible domains depending on the handedness of the polarization. Thus, σ^+ light creates SHG mostly in one of the two antiferromagnetic 180° domains, while σ^- light yields SHG response mostly from the other one. Thus a very pronounced intensity contrast of two AF domains is observed in SHG. The authors attributed this contrast to the interference of magnetic and electric dipole contributions, the latter being present only below the Néel temperature. These contributions are described by the nonlinear magnetic and electric susceptibility tensors, denoted as $\chi_m(i)$ and $\chi_e(c)$ respectively. The interference between the two contributions is constructive in one domain and destructive in the other one (for the given helicity of the light), which reflects the fact that $\chi_e(c)$ changes the sign under spin reversal⁶ (the operation which leads the domains into each other) while $\chi_m(i)$ remains constant.

From the theoretical point of view, in most cases a symmetry analysis has been applied to study the nonlinear magneto-optical susceptibility tensor $\chi_{el}^{(2\omega)}$ (the source for SHG within the electric dipole approximation). A classification following this approach, with tensors of a rank up to six, has been performed by Lyubchanskii *et al.* [16, 32, 33, 34, 35]. In Ref. [16] the authors include the magnetization-gradient terms and apply the group-theoretical classification to higher-rank susceptibility tensors. This approach then

⁶Originally, the authors use the name “time-reversal”, marking by (*i*) tensors which are invariant, and by (*c*) those which change sign under this operation. In our opinion the idea of time-reversal cannot be applied to nonlinear optics, thus we use the notion of “spin-reversal”. These issues are discussed in detail in Sec. 2.4

allows them to consider the thickness and the character (Bloch vs. Néel type) of domain walls. An attempt by Muthukumar *et al.* [36] to calculate the $\chi_{el}^{(2\omega)}$ tensor elements for antiferromagnetic Cr_2O_3 both from group theory as well as *from the microscopic point of view* is rather unique. They implemented a $(\text{CrO}_6)_2$ cluster, thus taking into account only half of the spins present in the elementary magnetic cell. In this approximation they explained the SHG from Cr_2O_3 as observed by Fiebig *et al.* [5] and they were able to give a quantitative estimate for that. Tanabe *et al.* [37], however, pointed out that the occurrence of purely real or imaginary values of the tensor elements plays a decisive role for the existence of SHG from this substance. They found that for a $(\text{CrO}_6)_2$ cluster SHG can take place only in the case where the tensor elements are imaginary, and thus should vanish in Muthukumar's approximation. They proposed to take into account the full unit cell with four inequivalent Cr ions including their "twisting" interaction with the environment. However Tanabe *et al.* neglected the dissipation in the process of SHG⁷, which is a rather crude approximation, in particular close to resonances. In general, dissipation makes the $\chi_{el}^{(2\omega)}$ tensor elements complex and invalidates their separation in purely real and imaginary ones [39].

Lifting the inversion symmetry of a crystal is the source for SHG within the electric dipole approximation. Lyubchanskii *et al.* [32, 34] suggested crystal lattice deformations and displacements as possible reasons for SHG from YIG films. In the case of Cr_2O_3 and $\text{YBa}_2\text{Cu}_3\text{O}_{6+\delta}$, described by Lyubchanskii *et al.* [33, 34], AF ordering lowers the symmetry of an otherwise centrosymmetric crystal. In this work, however, we rely on the idea that, rather than lowering the crystal symmetry in the bulk, SHG may also result from the breaking of inversion symmetry at the surface of a bulk inversion-symmetric system. In the next section, we will present our theory for the symmetry analysis of SHG, along these lines.

2.2 Basic Principles of the Symmetry Analysis

In this section, we outline the method to classify the nonlinear magneto-optical response from the symmetry point of view. This presentation will be done in two steps.

- Firstly, we will explain how the symmetries of the sample determine the presence or absence of the elements of the nonlinear optical susceptibility tensor, which is the source of SHG.
- Secondly, we will examine the dependence of these tensor elements on domain operations and the magnetic order parameter. The fact that some tensor elements preserve their sign while others change it under the change of the order parameter is very important for domain imaging.

⁷The authors perform the analysis of $\chi^{(2\omega)}$ in the frequency space. There are no reasons to neglect the damping in this approach. Moreover, if the dissipation is neglected, and $\chi_{ijk}^{(2\omega)}$ is taken as purely real or imaginary, then the Kramers-Kronig relations cannot be applied. In real time, on the other hand, dissipation does not take place, as stated in [38]. This topic will be analyzed more deeply in Sec. 2.4.

The surfaces of NiO serve as an example and guideline for our analysis. In Sec. 2.3, the results of this analysis are applied to particular magnetic systems.

2.2.1 Nonvanishing Tensor Elements

Based on group theory, Dähn *et al.* [40] proposed a new nonlinear magneto-optic Kerr effect (NOLIMOKE) at the (001), (110), or (111) monolayers of cubic antiferromagnets. They also gave an example of an antiferromagnetic structure (the (001) surface of NiO) and an optical configuration, where this new effect could be observed in SHG. Here, we perform a complete group-theory based analysis of collinear AF fcc low-index crystal surfaces. Surfaces of other crystal structures are as well described by our theory provided they are similar to these fcc crystal surfaces, i.e. squares or hexagons. The results can be used to detect the magnetic phase of a specific surface under investigation (to decide if the surface is para-, ferro-, or antiferromagnetic) and allow for the determination of the surface spin configuration in some important cases. However, in order to calculate the SHG yield quantitatively, it is necessary to go beyond group theory and use electronic calculations⁸ of the nonlinear susceptibility. Such a calculation will be presented in Chapter 3 of this thesis.

In order to be clear with respect to the essential notion of time reversal we would like to emphasize the point of view taken in this paper in the beginning. Here, we do not divide $\chi_{el}^{(2\omega)}$ into even and odd parts in the magnetic order parameter. Instead, the behavior of $\chi_{el}^{(2\omega)}$ with respect to the magnetic order parameter (which for ferromagnetic materials corresponds to the dependence of $\chi_{el}^{(2\omega)}$ on magnetization) is fully taken into account by the consideration of the magnetic point group. At no stage of our consideration we invoke the notion of time reversal, consequently we do not apply the characterization of the susceptibility $\chi^{(2\omega)}$ as c-tensor (changing its sign under time reversal) or i-tensor (invariant under the time-reversal operation) [39].

Before we start our group theoretical classification of the nonlinear optical susceptibilities of antiferromagnetic (AF) surfaces we would like to emphasize the following four important points:

- (i) We are not interested in effects resulting from the *optical path difference* from adjacent crystal planes which are ferromagnetically ordered but only antiferromagnetically coupled to each other. We do not consider this as an intrinsic AF effect.
- (ii) Cubic crystals that we are interested in reveal a center of inversion in the para-, ferro-, and all antiferromagnetic phases. Thus, within the electric dipole approximation, the SHG signal exclusively results from the surface.
- (iii) While in principle linear optical methods can be sensitive to the presence of a spin structure, in practice they are not useful because, within the group theoretical approach, they cannot distinguish the AF phase from either the paramagnetic or the ferromagnetic one, nor can they distinguish different AF configurations from each other. They have to resort to methods like lineshape analysis, where no strong statements characteristic for symmetry analysis can be made.

⁸Such a calculation necessarily exploits group theory, however.

(iv) Although the tensor elements for all the magnetic point groups are known and tabulated in the literature (e.g. [41]), the connection between the different spin configurations described by us and the mentioned symmetry groups has not been made, except for some easy cases [40]. Thus, for SHG from antiferromagnetic surfaces, there has been up to now no connection at all between the group theoretical classification and the real situations found in experiments on oxide surfaces.

The following part of the text explains the fundamentals of applying NOLIMOKE observations to investigate antiferromagnetism of surfaces.

Now we turn to SHG, the source of which is the nonlinear electrical polarization $P_{el}^{(2\omega)}$ given by:

$$P_{el}^{(2\omega)} = \epsilon_0 \chi_{el}^{(2\omega)} : E^{(\omega)} E^{(\omega)}. \quad (2.1)$$

Here, $E^{(\omega)}$ is the electric field of the incident light, while $\chi_{el}^{(2\omega)}$ denotes the nonlinear susceptibility within the electric dipole approximation, and ϵ_0 is the vacuum permittivity. The intensity of the outgoing SHG light is [42]:

$$I^{(2\omega)} \sim (I_0)^2 \left[\begin{array}{l} \left(\begin{array}{l} A_1(\Theta) \cos \Phi \\ A_2(\Theta) \sin \Phi \\ A_3(\Theta) \cos \Phi \end{array} \right) \times \\ \times \left(\begin{array}{cccccc} \chi_{xxx} & \chi_{xyy} & \chi_{xzz} & \chi_{xyz} & \chi_{xzx} & \chi_{xxy} \\ \chi_{yxx} & \chi_{yyy} & \chi_{yzz} & \chi_{yyz} & \chi_{yzx} & \chi_{yyx} \\ \chi_{zxx} & \chi_{zyy} & \chi_{zzz} & \chi_{zyz} & \chi_{zzx} & \chi_{zxy} \end{array} \right) \times \\ \times \left(\begin{array}{l} B_1(\vartheta) \cos^2 \varphi \\ B_2(\vartheta) \sin^2 \varphi \\ B_3(\vartheta) \cos^2 \varphi \\ B_4(\vartheta) \cos \varphi \sin \varphi \\ B_5(\vartheta) \cos^2 \varphi \\ B_6(\vartheta) \cos \varphi \sin \varphi \end{array} \right) \end{array} \right]^2 \quad (2.2)$$

where I_0 is the intensity of the incident light, A_i , B_j ($i = 1..3; j = 1..6$) are Fresnel and geometrical factors for the incident and reflected light, ϑ and Θ angles of incidence and reflection, respectively ($\vartheta = \Theta$), and Φ (φ) is the output (input) polarization angle at frequency 2ω (ω). According to Neumann's principle, "any type of symmetry which is exhibited by the crystal is possessed by every physical property of the crystal" [41]. To examine these physical properties, we determine the magnetic point group of the crystal lattice, thus determine its symmetries. The same symmetries must leave the investigated property tensor (in our case the nonlinear electric susceptibility $\chi_{el}^{(2\omega)}$) invariant. This fact is mathematically expressed by the following condition:

$$\chi_{el, i'j'k'}^{(2\omega)} = l_{i'i} l_{j'j} l_{k'k} \chi_{el, ijk}^{(2\omega)}, \quad i, j, k, i', j', k' = x, y, z. \quad (2.3)$$

Here, $l_{n,n'}(n = i, j, k, n' = i', j', k',)$ is a representation of an element of the magnetic point group describing the crystal, i.e. of its symmetry. For symmetry operations including the time reversal there should be an additional “ \pm ” sign on the right hand side of Eq.(2.3), but we do not use it here since, as stated before, we exclude the time reversal from our consideration. In particular, from Eq.(2.3) it follows immediately that polar⁹ tensors of odd rank (such as $\chi_{el}^{(2\omega)}$) vanish in inversion symmetric structures. This explains why SHG is possible only at surfaces and interfaces, where this symmetry is broken.

For a given spin configuration we apply Eq. (2.3) for every symmetry operation present in the system. Thus, each of these symmetries gives rise to a set of 27 equations with 27 unknown elements of the tensor $\chi_{el}^{(2\omega)}$. This set can be reduced to 18 equations, since

$$\chi_{el,ijk}^{(2\omega)} = \chi_{el,ikj}^{(2\omega)}, \quad (2.4)$$

which expresses the equivalence of the two incident photons of frequency ω in SHG, see also the reduced tensor notation in Eq. (2.2).

As an example, we consider a spin configuration depicted in Fig. 3 which exhibits only one nontrivial symmetry, which is the rotation by 180° degrees around the axis perpendicular to the figure plane (denoted as 2_z). This symmetry operation is represented by the following matrix:

$$l(2_z) = \begin{pmatrix} -1 & 0 & 0 \\ 0 & -1 & 0 \\ 0 & 0 & 1 \end{pmatrix}$$

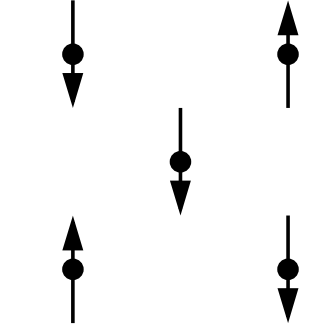


Figure 3: Example of an antiferromagnetic surface spin structure. Arrows represent magnetic moments localized on lattice sites. This fragment, containing 5 lattice sites, fully represents an infinite crystal surface.

⁹ Polar tensors change their sign under the space-inversion operation [41].

Substituting this to Eq. (2.3) one gets the following set of equations:

$$\begin{aligned}
\chi_{xxx} &= -\chi_{xxx} \\
\chi_{xyy} &= -\chi_{xyy} \\
\chi_{xzz} &= -\chi_{xzz} \\
\chi_{xyz} &= \chi_{xyz} \\
\chi_{zxx} &= \chi_{zxx} \\
\chi_{xxy} &= -\chi_{xxy} \\
\chi_{yxx} &= -\chi_{yxx} \\
\chi_{yyy} &= -\chi_{yyy} \\
\chi_{yzz} &= -\chi_{yzz} \\
\chi_{yyz} &= \chi_{yyz} \\
\chi_{yzx} &= \chi_{yzx} \\
\chi_{yxy} &= -\chi_{yxy} \\
\chi_{zxx} &= \chi_{zxx} \\
\chi_{zyy} &= \chi_{zyy} \\
\chi_{zzz} &= \chi_{zzz} \\
\chi_{zyz} &= -\chi_{zyz} \\
\chi_{zzx} &= -\chi_{zzx} \\
\chi_{zxy} &= \chi_{zxy}
\end{aligned} \tag{2.5}$$

Obviously, these equations can be satisfied only if some tensor elements (χ_{xxx} , χ_{xyy} , χ_{xzz} , χ_{xxy} , χ_{yxx} , χ_{yyy} , χ_{yzz} , χ_{yxy} , χ_{zyz} , and χ_{zzx}) vanish. Other tensor elements can have arbitrary values.

Any additional symmetry present in the system will result in a different set of equations which will put additional constraints on tensor elements. We solve the equations for each symmetry separately, since the symmetry operations are independent. In this way, our sets of equations were always limited to 18 equations.

A different symmetry operation than 2_z will result in different constraints. In particular, symmetries whose representations contain off-diagonal matrix elements force some relations between tensor elements in the form of $\chi_{ijk} = \chi_{lmn}$. Generally, if the representation of a symmetry has a complicated form, the set of equations is also complicated. Fortunately, this can always be split into several decoupled subsets. For example, an obvious subset in every case is, due to the existence of the surface, the equation $\chi_{zzz} = \chi_{zzz}$, this tensor element occurs nowhere else. The rank of the other subsets is, as it turns out for our cases, never higher than six. In this manner, one may obtain a set of forbidden elements of the susceptibility tensor as well as relations between allowed ones.

2.2.2 Reversal of the Order Parameter

In the previous subsection we introduced a method which allows to determine the nonvanishing tensor elements (for a given spin configuration). Another interesting issue is the behavior of the tensor elements with respect to the *inversion* or *change* of the AF order parameter \mathbf{L} (for ferromagnetic phases \mathbf{L} should be replaced by the magnetization \mathbf{M}), which is imposed by the operations that transform one domain into another (i.e. domain operations). Let us define the behavior of these tensor elements, which change their sign or are invariant in a given domain operation (which may, but not necessarily does invert the order parameter), as a *domain-parity*. The words “odd” and “even” are used henceforth explicitly with respect to this domain-parity, unless stated differently.

In general, a tensor element can be decomposed in parts odd and even in the domain operation, as shown in Eq. (2.6).

$$\chi_{ijk}^{(2\omega)} = \chi_{ijk}^{(2\omega),odd} + \chi_{ijk}^{(2\omega),even} \quad (2.6)$$

In systems with high symmetry, it is possible to describe an operation which reverses \mathbf{L} (or \mathbf{M}) by a spatial operation \hat{l} . The operation \hat{l} belongs to the point group of the system, but not to its magnetic point group. The application of this operation to a tensor element will change its sign (keep it invariant) if this element is odd (even) in \mathbf{L} . Consequently, each tensor element can be either odd or even in \mathbf{L} , a mixed behavior is forbidden.

Actually, the domain-parity of a given tensor element is a function of the chosen domain operation \hat{l} . In most antiferromagnetic configurations more than one operation leading to different domain structures are possible (this means that the order parameter is a vector). For example, for (001) surface one has 4_z rotations (i.e. 90° rotations) leading to different domains *in addition* to the eventual mirror-domain¹⁰ structure. For the (111) surface, there are three domains resulting from the rotations with respect to the z axis alone. For some configurations, they exist in addition to the mirror-domains. The 4_z domain operation, although it does not reverse the order parameter, allows for addressing the domain-parity in a relatively simple way. After applying this operation, a given tensor element is often mapped onto another one¹¹. In many cases we were able to detect the change of the sign (or its conservation) under such a mapping, and consequently, in many cases, we give the domain-parity information for tensor elements in the 4_z domain operation. This can ease the analysis of the possible 90° domain imaging on antiferromagnetic surfaces.

Domain structures on (111) surfaces are usually more difficult to address from the point of view of domain-parity. The naive notion of an operation with parity requires that the original situation is restored after applying the operation at most twice. Obviously, 2_z is such an operation and, for certain configurations, 4_z satisfies this criterion as well (where 2_z is just a symmetry operation), besides we were able to draw some conclusions on the domain-parity. However, neither 3_z (120° rotation) nor 6_z (60° rotation) have this property - they must be applied at least 3 times to restore the original situation. Also,

¹⁰For the definition of mirror domains, see Subsec. 2.3.7.

¹¹The indices x and y of the tensor element are exchanged, and a sign change may occur, since $x \rightarrow y$ and $y \rightarrow -x$.

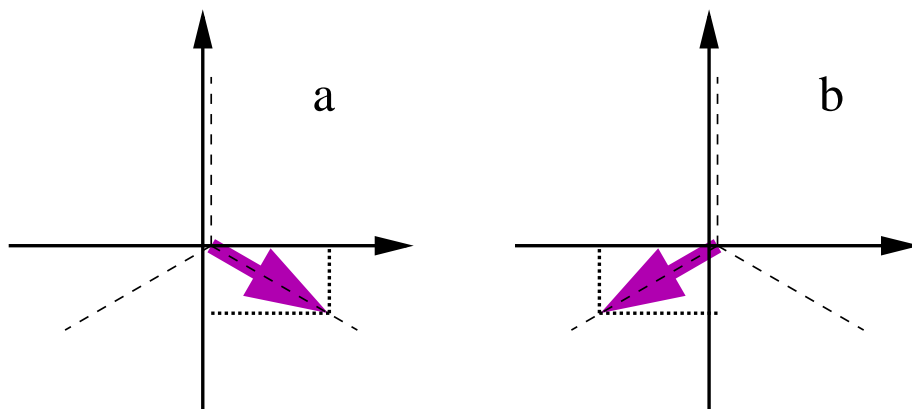


Figure 4: Change of the order parameter (represented by the grey arrow) under operation 3_z . Note that a part of this order parameter changes its sign, while the other remains unchanged.

upon the 3_z operation a single tensor element gets “split” into several tensor elements, and the analysis of the conservation (or not) of the sign of the tensor element loses its sense. The tensor elements are described in the Cartesian coordinate system, where quarters are the elementary entities. Rotation by an angle other than 90° and its multiples cannot be described as interchanging the axes and a possible modification of their signs. However, it is possible to treat the domain-parity of tensor elements in the 3_z and 6_z operation in a more general way. The very fact of having three states prevents us from using the domain-parity in its usual meaning of something simply changing the sign *or* remaining unchanged. Instead, we may allow the domain operation 3_z (for example) to reverse only one part of the order parameter, leaving the other part unchanged (Fig. 4). In other words, we would decompose the order parameter (or an investigated tensor element) into parts whose domain-parity can then be conventionally described. In this way we can deal with the domain-parity of tensor elements on surfaces with arbitrarily complicated domain structure. In this work however, we will not address the domains on (111) surfaces in detail.

In many occasions, it is convenient to define one order parameter that describes equally well all the magnetic phases and spin configurations of a given crystal structure [33, 43]. In this work, we define the order parameters separately for each of the addressed spin configurations¹². The order parameters defined in this way are, although vectors themselves, components of the order parameter in the sense of [43].

Note, the presence of dissipation (redistribution of response frequencies) does not influence the considerations about the domain-parity. In general, dissipation in frequency space is responsible for the mixing of the real and imaginary parts in the tensor elements (as described in Sec. 2.4), while point-group symmetry governs the (non)existence of tensor elements purely odd or even in the magnetic order parameters \mathbf{L} or \mathbf{M} .

¹²For the definition of configurations see Subsec. 2.3.1.

So far we have presented the method used in our symmetry analysis of the surfaces. We know how the symmetries determine the sets of non-vanishing tensor elements and (in some cases) the relations between them. In the next section we will present the results we obtained by applying this method.

2.3 Results of the Group Theoretical Analysis

In the previous section, we presented the method used for the symmetry classification of the surfaces of cubic antiferromagnets. We now apply this method to all distinct spin configurations of low-index surfaces of fcc crystals, including ferro- and paramagnetic surfaces for the sake of completeness. Here, we would like to present the results of this study. This presentation involves:

- nonvanishing tensor elements (and if applicable their domain-parity) for each spin configuration for low index surfaces of fcc crystals,
- influence of different kinds of distortions,
- role of a second layer of atoms,
- conditions for domain imaging,
- considerations about experimental geometries.

The results of the symmetry analysis, presented in this section, can be used in an experiment according to Fig. 5. The detailed description of an experimental use of our results is presented in Subsec. 2.3.8.

2.3.1 “The Table” and How to Read It

The main results of our symmetry analysis is presented in Table I. It displays the non-vanishing tensor elements and the relations between them for each of the spin structures addressed by us. In the current subsection, we explain how this Table should be read. First, we will define the notions of “phase”, “case”, and “configuration”, used henceforth to classify our results.

- “Phase” describes the magnetic phase of the material, i.e. paramagnetic, ferromagnetic, or AF.
- Secondly, the word “configuration” is reserved for the description of the magnetic ordering of the surface. It describes various possibilities of the spin ordering, which are different in the sense of topology. The configurations cannot be transformed into each other by point-group operations, therefore we define the (ferromagnetic or antiferromagnetic) order parameter separately for each configuration. We describe up to 18 AF configurations, denoted by little letters a) to r), as well as several ferromagnetic configurations, denoted as “ferro1”, “ferro2”, etc. The number of possible configurations varies depending on surface orientation.

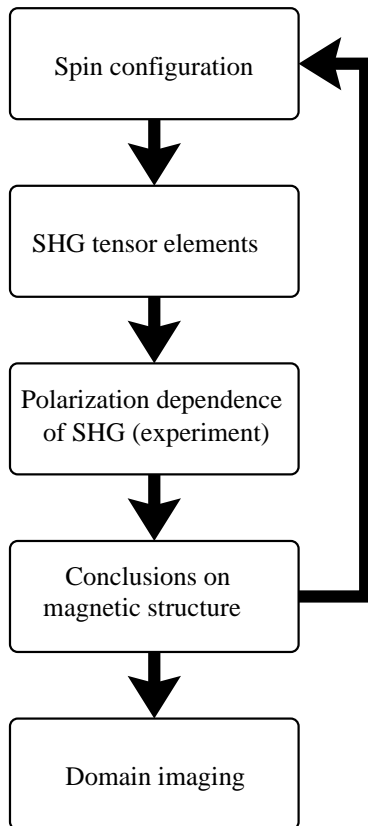


Figure 5: An SHG experiment on an AF surface. Initial assumption about the examined structure is verified by a proper choice of experimental geometry and polarization dependence.

- Thirdly, we describe different “cases”, i.e. additional structural features superimposed on the symmetry analysis. “Case A” does not have such additional features - it describes usual surfaces of fcc crystals. In “case B” we address distortions of the lattice of the magnetic atoms. “Case C” deals with two kinds of magnetic atoms in an undistorted lattice. In “case D” we take into account a distorted sublattice of nonmagnetic atoms, keeping the magnetic sublattice undistorted. All the analysis is restricted to collinear antiferromagnets.

The results are displayed by (i) pictures (which define each of the addressed configurations) and (ii) tables (which describe the SHG response of the given configuration).

(i) Presentation in figures. The figures present the spin configurations for the (001), (110), and (111) surfaces. The philosophy of this presentation is that, to avoid extensive length, we show the spin structure in one figure for each surface (Figs. 8, 9, and 10) for all the four cases (A-D), and depict the effects taken into account in the cases B-D only for the paramagnetic phase (Figs. 11, 12, and 13).

Several spin structures depicted in Fig. 8 and Fig. 10 are distinct configurations only in case B, and they are addressed in the tables that concern only this case. For the rest of the cases they are domains of other, fully described configurations, thus they are left out from consideration in these cases.

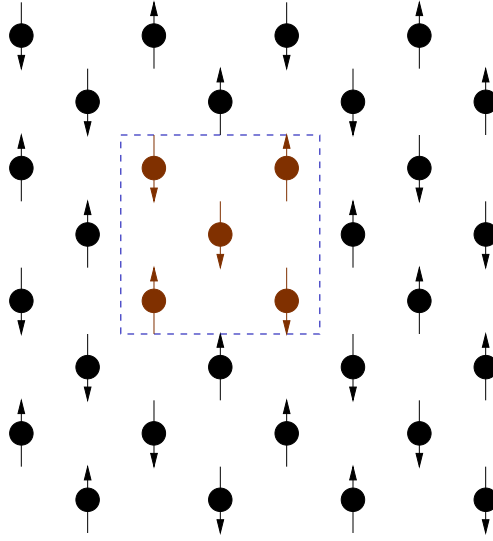


Figure 6: Conventional unit cell as a fragment of an infinite surface.

The figures display “conventional unit cells” with a limited number of lattice sites, however they represent an infinitely extended surface. No oxygen atoms are displayed here. To obtain the whole surface from the depicted fragment, we use the following convention: about the spin structure is presented in Fig. 7¹³; this neighboring spins along the x and y directions point the same way (alternate) if they are parallel (antiparallel) on the plaquette in these two directions. The spins in rows and columns where only one spin is presented are continued in the same way as the corner spins. This is shown in Fig. 6, for the conf. c) of the (001) surface. This convention will be maintained henceforth (for a (111) surface one has to alter or keep the spins along three axes, instead of two). The smallest set that gives a complete idea “magnetic Wigner-Seitz cell” does not give a clear picture of the crystal symmetries, however. Thus we show the “conventional unit cell” instead (in the sense of crystal lattice theory) as outlined for one example in Fig. 6. The whole crystal lattice can be reproduced by translations of this cell, without performing other operations such as reflections or rotations.

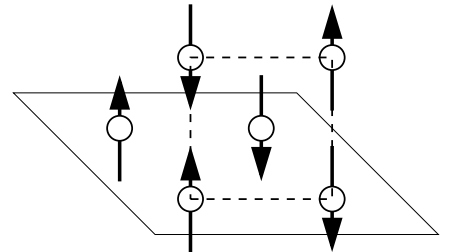


Figure 7: Top view of a spin structure on a (001) surface. The dashed line depicts a conventional unit cell, while the solid one outlines the primitive unit cell.

(ii) Presentation in the tables. First, let us describe briefly the notation¹⁴ used for the symmetry operations. N_i describes a proper rotation, where N is an integer and defines the angle of rotation by $\frac{2\pi}{N}$, and i describes the axis of rotation. The axes are defined in the Figure presenting the corresponding surface. Spatial inversion is described by $\bar{1}$, and combinations of this operation with proper rotations define *improper* rotations, which we

¹³Although our primitive cell contains 4 magnetic atoms they do not fall on a straight line, and thus we still have a two-sublattice antiferromagnet. The primitive cell of a typical four lattice antiferromagnet, like Cr_2O_3 contains 4 magnetic atoms placed on a straight line.

¹⁴It is commonly called “International Notation”.

use describe all the mirror operations in this work. The bar is then put over the multiplicity factor of the rotation.

The tables show the SHG response types for each configuration. The various response types are “encoded” by a “key”, which is then “decoded” in Tab. I. This table presents the symmetries, domain operations, and nonvanishing tensor elements for each response type. This is done in order to shorten the overall length of tables, because a given response type can appear in several different cases.

Table I also contains the information on the domain-parity of the nonvanishing tensor elements: the odd ones are printed in boldface. If two or more domain operations have the same effect, we display all of them together. To make the Table I shorter and more easily readable these domain operations (and the corresponding domain-parity information for the tensor elements), that can be created by a superposition of the displayed domain operations, are not displayed. Usually, if more than one domain pattern is possible for a given configuration, the domain-parity of tensor elements is different in different domain operations. For example, if both 90° domains and mirror domains with operation $\bar{2}_x$ are possible, some tensor elements may be, say, odd in 4_z and even in $\bar{2}_x$. This is accounted for by different entries for the domain operations of a given configuration in Table I.

Also, a situation is possible that a tensor element is even in the presented domain operation but is odd in the inverse operation. This fact is expressed by use of italics, and the use of bold- or lightface describes the domain-parity of the tensor element in this operation which is listed in the table. Italic font just hints that the domain-parity changes in the operation which is the inverse of the displayed one. For example, the entry j) of Table I shows a tensor element χ_{xxx} displayed as *xxx*, which is even under the operation 4_z , this means that tensor element χ_{xxx} is odd under -4_z . This behavior of tensor elements may seem strange at first sight. However, it is caused by the fact that under these operations, tensor elements are not mapped on themselves. In our example, after applying 4_z the tensor element χ_{xxx} becomes χ_{yyy} , without changing its sign. If we now apply -4_z , χ_{yyy} (which is under -4_z) becomes χ_{xxx} , again without changing the sign. In order to keep the presentation short, we present the information about the domain-parity of the tensor elements concerning only one domain operation from each pair of mutually inverse operations.

The domain-parity of the elements has been checked in the operations 2_z , 4_z , and in the operation connecting mirror-domains to each other (for the definition of the mirror-domain structure see Subsec. 2.3.7). We do not address the domain-parity of tensor elements in the 6_z nor 3_z operations for (111) surfaces nor any other operation that “splits” tensor elements, although these operations also lead to a domain structure (see Subsec. 2.2.2). As was discussed earlier, it is possible to define a parity of the tensor elements for the 3_z and 6_z operations, however the tensor elements then undergo more complicated changes. The situations where the domain-parity of the tensor elements is too complicated to be displayed in the Table are indicated by a hyphen in the column “domain operation”. For some configurations, there is no operation that leads to a domain structure - in those configurations we display the information “one domain”.

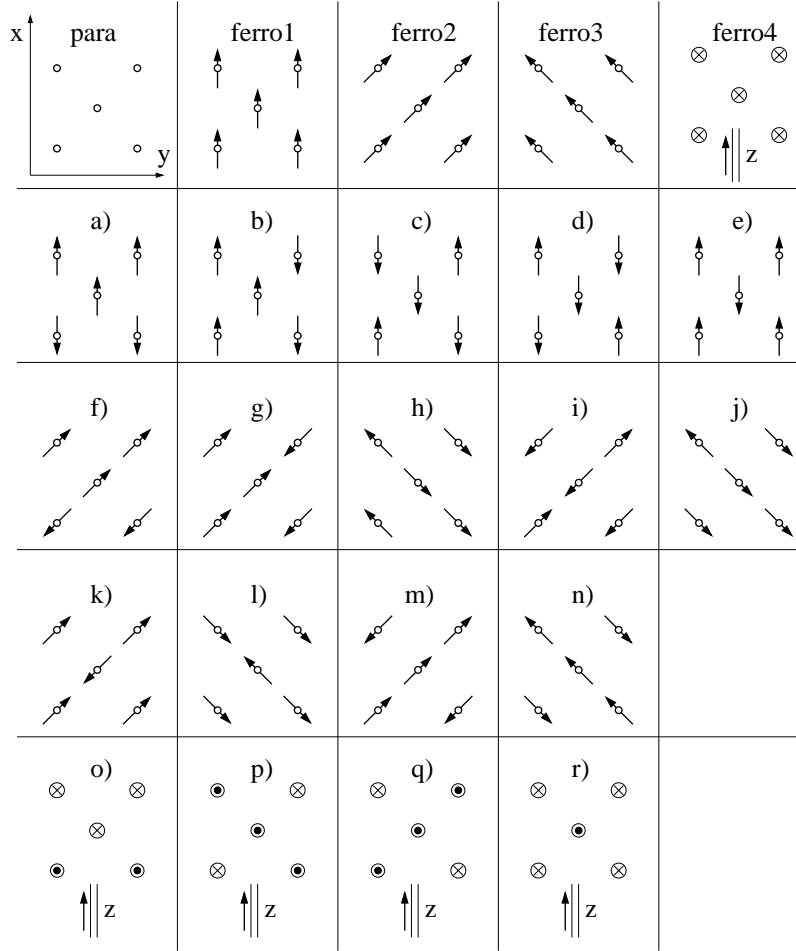


Figure 8: Spin configurations of an fcc (001) surface. Except for confs. “ferro4” and o) - r), the arrows always indicate in-plane directions of the spins. In confs. “ferro4” and o) - r) \otimes (\odot) denote spins pointing along the positive (negative) z-direction, respectively.

Scope of the presentation. As far as the first layer is concerned, we address all the collinear spin configurations of the low index surfaces of fcc antiferromagnets, with order parameter \mathbf{L} lying in plane or perpendicular to it and antiferromagnetic coupling between nearest neighbors. For the (001) surfaces we also discuss the configurations, where the antiferromagnetic coupling exists between the second-nearest neighbors (configurations a), b), c), f), and o), along with d), g), and h) for case B.). We do not consider the coupling to the third and further neighbors. This would not give rise to configurations of different symmetries in two dimensions. It may at most replace spins by grains (blocks) of spins in the configurations described by us. *Thus, our symmetry analysis is complete.*

In this work we thoroughly discuss the spin structure of the first (uppermost) atomic layer. This is sufficient to study all the symmetries of (001) and (110) surfaces both in the paramagnetic and ferromagnetic phases. For the (111) surface it is necessary to recognize the atomic positions (but not the spins) in the second layer for the same purpose. For the sake of completeness we also present a study of (111) surfaces without this extension.

However, in the antiferromagnetic phase, the spin structure of the second and deeper layers plays a role in determining the symmetry of the surface [44]. This is presented in Subsec. 2.3.6, for the simple (undistorted) case, i.e. case A. These structures can serve as simple models for deriving predictions for more complicated cases (B, C, and D), while the full consideration of the second layer would not bring any new interesting results. Taking into account the spin structure of the second layer (deeper layers do not bring up anything new to the analysis) results in creating several (up to two for the (001) surface and three for the (111) surface) configurations out of each one addressed here by us. The symmetry of these configurations may remain the same or be lowered (sometimes even below the symmetry of the ferromagnetic phase) with respect to the “two-dimensional” configurations they are generated from. The results of this analysis are described in Subsec. 2.3.6.

In the next subsections, we will discuss the results of our symmetry analysis.

Table I. Details of SHG response types. We denote $\chi_{ijk}^{(2\omega)}$ by ijk . Odd elements are in bold if a domain operation exists.

key	pt. group	symmetry operations	domain operation	non-vanishing tensor elements
a	4mm	$1, 2_z, \pm 4_z, \bar{2}_x, \bar{2}_y, \bar{2}_{xy}, \bar{2}_{-xy}$	one domain	$xxz = xzx = yyz = yzy, zxx = zyy, zzz$
b	m	$1, \bar{2}_x$	$2_z, \bar{2}_y$	$xzx = xxz, \mathbf{xyx} = \mathbf{xyx}, \mathbf{yxx}, \mathbf{yyy}, \mathbf{yzz},$ $yyz = yzy, zxx, zyy, zzz, \mathbf{zyz} = \mathbf{zyz}$
c	m	$1, \bar{2}_{xy}$	$4_z, \bar{2}_{xy}$ $2_z, \bar{2}_{-xy}$	no information about the domain-parity $\mathbf{xxx} = -\mathbf{yyy}, \mathbf{xyy} = -\mathbf{yxx}, \mathbf{xzz} = -\mathbf{yzz},$ $xyz = yxz = xzy = yzx,$ $xxz = xzx = yyz = yzy,$ $\mathbf{xxy} = -\mathbf{yyx} = \mathbf{xyx} = -\mathbf{yxy},$ $zxx = zyy, zzz,$ $\mathbf{zxx} = \mathbf{zxx} = -\mathbf{zyz} = -\mathbf{zzy}, zxy = zyx$ $\mathbf{xxx} = -\mathbf{yyy}, xyy = yxx, xzz = -\mathbf{yzz},$ $\mathbf{xyz} = \mathbf{xzy} = \mathbf{yxz} = \mathbf{yzx},$ $xxz = xzx = yyz = yzy,$ $xyx = -\mathbf{yxy} = xyx = -\mathbf{yxy}, zxx = zyy,$ $zzz, \mathbf{zxx} = \mathbf{zxx} = zyz = zzzy, \mathbf{zxy} = \mathbf{zyx}$ $\mathbf{xyz} = \mathbf{xzy} = -\mathbf{yxz} = -\mathbf{yzx},$ $xzx = xxz = yzy = yyz,$ $zxx = zyy, zzz$
d	4	$1, 2_z, \pm 4_z$	$\bar{2}_x, \bar{2}_y, \bar{2}_{xy}, \bar{2}_{-xy}$	$xxz = xzx, yyz = yzy, zxx, zyy, zzz$ $\mathbf{xyz} = \mathbf{xzy}, \mathbf{xxz} = \mathbf{xzx}, \mathbf{yyz} = \mathbf{yzy},$ $\mathbf{yzx} = \mathbf{yxz}, zxx, zyy, zzz, \mathbf{zxy} = \mathbf{zyx}$ $xyz = xzy, \mathbf{xxz} = \mathbf{xzx}, \mathbf{yyz} = \mathbf{yzy},$ $yzx = yxz, zxx, zyy, zzz, \mathbf{zxy} = \mathbf{zyx}$ $xxz = xzx = yyz = yzy,$ $\mathbf{zxy} = \mathbf{xyz} = \mathbf{yzx} = \mathbf{yxz},$ $zxx = zyy, zzz, \mathbf{zxy} = \mathbf{zyx}$
e	mm2	$1, 2_z, \bar{2}_x, \bar{2}_y$	$\pm 4_z, \bar{2}_{xy}, \bar{2}_{-xy}$	$xxz = xzx, yyz = yzy, zxx, zyy, zzz$
f	2	$1, 2_z$	$\bar{2}_x, \bar{2}_y$	$\mathbf{xyz} = \mathbf{xzy}, \mathbf{xxz} = \mathbf{xzx}, \mathbf{yyz} = \mathbf{yzy},$ $\mathbf{yzx} = \mathbf{yxz}, zxx, zyy, zzz, \mathbf{zxy} = \mathbf{zyx}$ $xyz = xzy, \mathbf{xxz} = \mathbf{xzx}, \mathbf{yyz} = \mathbf{yzy},$ $yzx = yxz, zxx, zyy, zzz, \mathbf{zxy} = \mathbf{zyx}$ $xxz = xzx = yyz = yzy,$ $\mathbf{zxy} = \mathbf{xyz} = \mathbf{yzx} = \mathbf{yxz},$ $zxx = zyy, zzz, \mathbf{zxy} = \mathbf{zyx}$
g	mm2	$1, 2_z, \bar{2}_{xy}, \bar{2}_{-xy}$	$\pm 4_z, \bar{2}_x, \bar{2}_y$	$xxz = xzx, yyz = yzy, zxx, zyy, zzz$ $\mathbf{xyz} = \mathbf{xzy}, \mathbf{xxz} = \mathbf{xzx}, \mathbf{yyz} = \mathbf{yzy},$ $\mathbf{yzx} = \mathbf{yxz}, zxx, zyy, zzz, \mathbf{zxy} = \mathbf{zyx}$ $xyz = xzy, \mathbf{xxz} = \mathbf{xzx}, \mathbf{yyz} = \mathbf{yzy},$ $yzx = yxz, zxx, zyy, zzz, \mathbf{zxy} = \mathbf{zyx}$ $xxz = xzx = yyz = yzy,$ $\mathbf{zxy} = \mathbf{xyz} = \mathbf{yzx} = \mathbf{yxz},$ $zxx = zyy, zzz, \mathbf{zxy} = \mathbf{zyx}$
h	m	$1, \bar{2}_y$	$2_z, \bar{2}_x$	$\mathbf{xxx}, \mathbf{xyy}, \mathbf{xzz}, \mathbf{xxz} = \mathbf{xzx}, \mathbf{yyz} = \mathbf{yzy},$ $\mathbf{yyx} = \mathbf{yxy}, zxx, zzz, \mathbf{zxx} = \mathbf{zxx}$ $xxx, xyy, xzz, \mathbf{xxz} = \mathbf{xzx}, \mathbf{yyz} = \mathbf{yzy},$ $yyx = yxy, zxx, zzz, zxx = zxx$
i	1	1	2_z	All the elements are allowed: $\mathbf{xxx}, \mathbf{xyy}, \mathbf{xzz}, \mathbf{xyz} = \mathbf{xzy}, \mathbf{xzx} = \mathbf{xxz},$ $\mathbf{xxy} = \mathbf{xyx}, \mathbf{yxx}, \mathbf{yyy}, \mathbf{yzz}, \mathbf{yyz} = \mathbf{yzy},$

key	point group	symmetry operations	domain operation	non-vanishing tensor elements
j	m	$1, \bar{2}_{-xy}$	$\bar{2}_x$ $\pm 4_z, \bar{2}_{xy}, \bar{2}_{-xy}$ $2_z, \bar{2}_{xy}$	$yzx = yxz, \mathbf{yxy} = \mathbf{yyx}, zxx, zyy, zzz,$ $\mathbf{zyz} = \mathbf{zzy}, \mathbf{zxx} = \mathbf{zxx}, zxy = zyx$ $\mathbf{xxx}, \mathbf{xyy}, \mathbf{xzz}, \mathbf{xyz} = \mathbf{xzy}, xzx = xxz,$ $xxxy = xyx, yxx, yyy, yzz, yyz = yzy,$ $\mathbf{yzx} = \mathbf{yxz}, \mathbf{yxy} = \mathbf{yyx}, zxx, zyy, zzz,$ $zyz = zzy, \mathbf{zxx} = \mathbf{zxx}, \mathbf{zxy} = \mathbf{zyx}$ no information about the domain-parity $\mathbf{xxx} = \mathbf{yyy}, \mathbf{xyy} = \mathbf{yxx}, \mathbf{xzz} = \mathbf{yzz},$ $xyz = yxz = xzy = yzx,$ $xxz = xzx = yyz = yzy,$ $\mathbf{xxxy} = \mathbf{yyxy} = \mathbf{xyxx} = \mathbf{yxy},$ $zxx = zyy, zzz,$ $\mathbf{zxx} = \mathbf{zxx} = \mathbf{zyz} = \mathbf{zzy}, zxy = zyx$ $xxx = \mathbf{yyy}, xyy = \mathbf{yxx}, xzz = \mathbf{yzz},$ $\mathbf{xyz} = \mathbf{yxz} = \mathbf{xzy} = \mathbf{yzx},$ $xxz = xzx = yyz = yzy,$ $\mathbf{xyy} = \mathbf{xyx} = \mathbf{yyx} = \mathbf{yxy}, zxx = zyy, zzz,$ $zxx = zxx = \mathbf{zyz} = \mathbf{zzy}, \mathbf{zxy} = \mathbf{zyx}$ $xxz = xzx, yyz = yzy, zxx, zyy, zzz$ $xzx = xxz, \mathbf{xxxy} = \mathbf{xyxx}, \mathbf{yxx}, \mathbf{yyy}, \mathbf{yzz},$ $yyz = yzy, zxx, zyy, zzz, \mathbf{zyz} = \mathbf{zzy}$ All the elements are allowed: $\mathbf{xxx}, \mathbf{xyy}, \mathbf{xzz}, xyz = xzy, xzx = xxz,$ $\mathbf{xxxy} = \mathbf{xyxx}, \mathbf{yxx}, \mathbf{yyy}, \mathbf{yzz}, yyz = yzy,$ $yzx = yxz, \mathbf{yxy} = \mathbf{yyx}, zxx, zyy, zzz,$ $\mathbf{zyz} = \mathbf{zzy}, \mathbf{zxx} = \mathbf{zxx}, zxy = zyx$ $\mathbf{xxx}, \mathbf{xyy}, \mathbf{xzz}, \mathbf{xyz} = \mathbf{xzy}, xzx = xxz,$ $xxxy = xyx, yxx, yyy, yzz, yyz = yzy,$ $\mathbf{yzx} = \mathbf{yxz}, \mathbf{yxy} = \mathbf{yyx}, zxx, zyy, zzz,$ $zyz = zzy, \mathbf{zxx} = \mathbf{zxx}, \mathbf{zxy} = \mathbf{zyx}$ $\mathbf{xyz} = \mathbf{xzy}, xxz = xzx, yyz = yzy,$ $\mathbf{yzx} = \mathbf{yxz}, zxx, zyy, zzz, \mathbf{zxy} = \mathbf{zyx}$ $\mathbf{xxx}, \mathbf{xyy}, \mathbf{xzz}, xxz = xzx, yyz = yzy,$ $\mathbf{yyx} = \mathbf{yxy}, zxx, zyy, zzz, \mathbf{zxx} = \mathbf{zxx}$ $xxz = xzx = yyz = yzy, zxx = zyy, zzz$ $\mathbf{xyz} = \mathbf{xzy} = \mathbf{-yxz} = \mathbf{-yzx},$ $xxz = xzx = yyz = yzy, zxx = zyy, zzz$ $zxx = zyy, xxz = xzx = yyz = yzy, zzz,$ $xxx = -xyy = -yxy = -yyx$ All the elements are allowed: $xxx, xyy, xzz, \mathbf{xyz} = \mathbf{xzy}, xzx = xxz,$ $\mathbf{xxxy} = \mathbf{xyxx}, \mathbf{yxx}, \mathbf{yyy}, \mathbf{yzz}, yyz = yzy,$ $\mathbf{yzx} = \mathbf{yxz}, yxy = yyx, zxx, zyy, zzz,$ $\mathbf{zyz} = \mathbf{zzy}, zxx = xzx, \mathbf{zxy} = \mathbf{zyx}$ $xxx, xyy, xzz, xxz = xzx, yyz = yzy,$ $yyx = yxy, zxx, zyy, zzz, zxx = xzx$ $xxx = -xyy = -yxy = -yyx,$ $\mathbf{xyz} = \mathbf{xzy} = \mathbf{-yxz} = \mathbf{-yzx},$ $xzx = xxz = yyz = yzy,$ $\mathbf{xxxy} = \mathbf{xyxx} = \mathbf{yxx} = \mathbf{-yyy},$ $zxx = zyy, zzz$ All the elements are allowed
k	mm2	$1, 2_z, \bar{2}_x, \bar{2}_y$	one domain	
l	m	$1, \bar{2}_x$	$2_z, \bar{2}_y$	
m	1	1	2_z	
n	2	$1, 2_z$	$\bar{2}_x, \bar{2}_y$	
o	m	$1, \bar{2}_y$	$2_z, \bar{2}_x$	
p	6mm	$1, 2_z, \pm 3_z, \pm 6_z, 6(\bar{2}_\perp)$	one domain	
q	6	$1, 2_z, \pm 3_z, \pm 6_z$	$\bar{2}_x, \bar{2}_y$	
r	3m	$1, \pm 3_z, \bar{2}_y, \bar{2}_{S(xy)}, \bar{2}_{S(-xy)}$	one domain	
s	1	1	$\bar{2}_y$	
t	m	$1, \bar{2}_y$	-	
u	3	$1, \pm 3_z$	$\bar{2}_y$	
w	1	1	-	

2.3.2 Case A: Equivalent Atoms

The predicted new nonlinear magneto-optical effects result from the fact that the magnetic point groups of antiferromagnetic configurations are different from those describing paramagnetic or ferromagnetic phases of the same surface. Since, depending on the magnetic phase, different tensor elements vanish, it is possible to detect antiferromagnetism optically by varying the polarization of the incoming light.

The current subsection discusses nonvanishing elements of the nonlinear susceptibility tensor for an fcc crystal consisting of only one kind of magnetic atoms. The influence of nonmagnetic atoms in the material will be discussed later. The configurations considered here are “ferro1”, “ferro2”, “ferro4”, a), b), c), e), f), i), k), m), o), p), and r) for the (001) surface (see Fig. 8), “ferro1”, ferro3”, “ferro5”, a), c), f), i), and k) for the (111) surface (see Fig. 10), and all configurations depicted in Fig. 9 for the (110) surface. Other depicted spin structures form domains of these configurations and are not referred to in this subsection nor in the tables concerning the current subsection.¹⁵

(001) surface. All possible configurations of a fcc (001) surface are shown in Fig. 8. The SHG response types for the (001) monolayer are given in Table II, for the paramagnetic, ferromagnetic, and all AF phases. We can observe several sets of allowed tensor elements.

configuration	key (response type)
para	k
ferro1	l
ferro2	m
ferro3	n
ferro4	o
AF:	
a), b), c), g) - l)	k
d), e), f)	n

Table III. SHG response for all spin configurations of the (110) surface of a fcc lattice [45]. For the detailed description of the response types see Tab. I. The configurations are depicted in Fig. 9.

Conf. “ferro4” presents a completely different, distinguishable set of the nonvanishing

configuration	key (response type)
para	a
ferro1	b
ferro2	c
ferro4	d
AF:	
a), b), e), o)	e
c), f)	f
i), k), m), p)	g
r)	a

Table II. SHG response for all spin configurations of the (001) surface of a fcc lattice [45]. For the detailed description of the response types see Tab. I. The configurations are depicted in Fig. 8.

Configuration (conf.) r) will produce the same signal as the paramagnetic phase. Conf. “ferro1” reveals a completely different, distinguishable set of tensor elements. In addition, conf. “ferro2” produces another set of tensor elements, different from any other configuration. It is equivalent to the conf. “ferro1” rotated by 45°. In the confs. a), b), e), and o) we find the same tensor elements as for the paramagnetic phase. However, due to the lower symmetry, their values are no longer related to each other. Confs. c) and f) bring new tensor elements, thus allowing for the distinction of these confs. from the previous ones. Confs. i), k), m), p) reveal the same tensor elements as c) and f) but some of these elements are related. Thus one may possibly distinguish these two sets of configurations.

¹⁵If a spin structure is not described within this subsection (nor in the tables relevant to this subsection), it is a domain of the last displayed configuration that precedes the omitted one. This applies to all the Subsections 2.3.2, 2.3.3, 2.3.4, and 2.3.5.

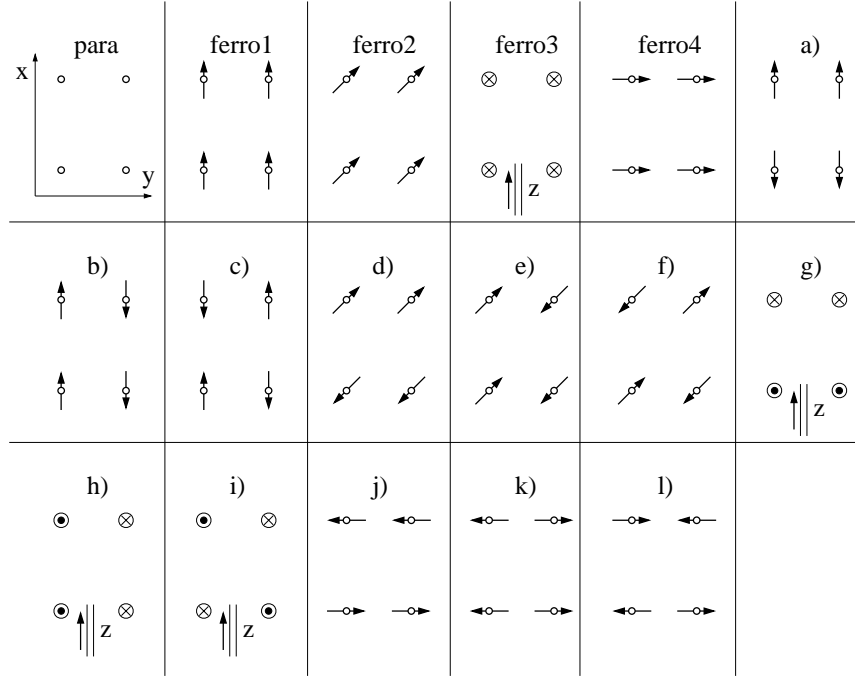


Figure 9: Spin configurations of an fcc (110) surface. Except for confs. “ferro3”, g), h), and i), the arrows always indicate in-plane directions of the spins. In confs. “ferro3”, g), h), and i) \otimes (\odot) denote spins pointing along the positive (negative) z-direction, respectively.

tensor elements. Consequently, in six configurations (i.e. c), f), i), k), m), and p)) some susceptibility tensor elements appear only in the AF phase, allowing for the detection of this magnetic phase by varying the incident light polarization, as will be outlined in Subsec. 2.3.8. In addition, all other antiferromagnetic configurations but r) reveal the breakdown of some of the relations between the different tensor elements, compared to the paramagnetic phase, and thus can be detected as well. Generally, all the magnetic phases can be distinguished from each other. There exists as well the possibility to distinguish different AF configurations provided the corresponding tensor elements can be singled out by the proper choice of the experimental geometry.

(110) surface. We now turn to the (110) surface (Fig. 9), which, in the paramagnetic phase, reveals a lower symmetry than the (001) surface. On the other hand, the number of symmetry operations in the AF configurations is comparable to the (001) surface. In addition, as shown in Table III, the resulting SHG response types are not very characteristic, so the detection possibilities for this surface are very limited. In particular, confs. a), b), c), g), h), i), j), k), and l) give the same tensor elements as the paramagnetic phase. Confs. d), e), f), and “ferro3” bring new tensor elements. Other ferromagnetic configurations (“ferro1” and “ferro2”) present different sets of new tensor elements, making these configurations distinguishable from the others as well as from each other. Conf. “ferro4” yields a completely different set of tensor elements, however this set is related to the one of conf. “ferro1” by a 90° rotation.

In short, the (110) surface presents very limited possibilities for any analysis due to a

of “ferro3” by 90° rotation does not affect the possibility to distinguish these two configurations. The ferromagnetic conf. “ferro5” brings up the same tensor elements as AF confs. c) and f), but the relations between the elements are different. The *second* subcase (more layers taken into account) gives different sets of allowed tensor elements (compared to the first subcase) for each but the “ferro3” configuration. Confs. a), i), k), and “ferro3” share the same set of allowed tensor elements and can be easily distinguished from the paramagnetic phase. Confs. c), f), and “ferro1” reveal all tensor elements, with their values unrelated. Similarly, conf. “ferro5” presents another, distinguishable set of tensor elements. The (111) surface presents less possibilities for distinction of the magnetic phases than the (001) surface, but there exist a certain possibility to distinguish the particular AF spin configurations, once the magnetic phase of the material is known.

The symmetry analysis of nonvanishing tensor elements for ferromagnetic surfaces in the case A has been performed by Pan *et. al.* [12]. Our analysis yields the same results, taking into account the corrections made by Hübner and Bennemann [46].

From the above discussion we can state that clearly the best possibilities to distinguish the magnetic phases and spin structures by SHG are presented by the (001) surface. There, the magnetic spin structure of NiO surface - its magnetic phase as well as the particular spin configuration - can be detected unambiguously.

In brief,

- the (001) surface offers good possibilities to distinguish the magnetic phases as well as the particular spin configurations,
- the (110) surface presents poor possibilities for the analysis,
- the (111) surface presents good possibilities for the distinction of the spin configurations, once the magnetic phase of the surface is known.

This concludes the discussion of the simple, undistorted antiferromagnetic surfaces. In the next subsection, we will investigate the influence of the rhombohedral distortion of the lattice.

configuration	key (response type)
para	r
ferro1	s
ferro3	t
ferro5	u
AF:	
a), i), k)	t
c), f)	u

Table V. SHG response for all spin configurations of the (111) surface of a fcc lattice [45]. More monolayers are taken into account. For the detailed description of the response types see Tab. I. The configurations are depicted in Fig. 10.

2.3.3 Case B: Distortions of Monoatomic Lattice

configuration	key (response type)
para	k
ferro1	m
ferro2	o
ferro3	l
ferro4	n
AF:	
a), b) - h), o)	n
i) - n), p) - r)	k

Table VI. SHG response for all spin configurations of the (001) surface of a fcc lattice, distorted to a rhombohedral structure. For the detailed description of the response types see Tab. I. For the surface structure see Fig. 11, for the spin configurations see Fig. 8.

The rhombohedral distortion of the atomic lattice, described here and shown in Fig. 11, makes the x and y axes of the (001) surface inequivalent, even in the paramagnetic phase. On the (111) surface, the y axis is not equivalent any longer to other axes connecting the nearest neighbors. These inequivalences of axes are the reasons for the reduction of the number of symmetry operations already in the paramagnetic phase. Because of this reduction some spin structures that previously formed different domains of a single configuration now cannot be transformed into each other and become “independent” configurations. This happens for almost every of the previously addressed configurations of the (001) and (111) surfaces. Consequently, all the depicted spin structures are in fact configurations, and are addressed in this subsection.

(001) surface. The resulting SHG response types for the (001) surface are listed in Table VI. For this surface, only two of the ferromagnetic configurations, namely “ferro1” and “ferro2” can be easily distinguished from both the paramagnetic as well as the antiferromagnetic phases. These ferromagnetic configurations can also be distinguished from each other. On the contrary, all the AF configurations yield only two types of response, and in addition one of them is equivalent to the response of the paramagnetic phase. Consequently, it will not be possible to determine the surface spin structure, and the distinction of the AF phase from the paramagnetic one can be successfully performed only in confs. a)-h) and o). Compared to the case A, there is an important symmetry breaking for most configurations. Thus, the distinction between the two cases (A and B) is possible (compare Tabs. II and VI).

(110) surface. All the (110) surfaces of an fcc crystal with a rhombohedral distortion are

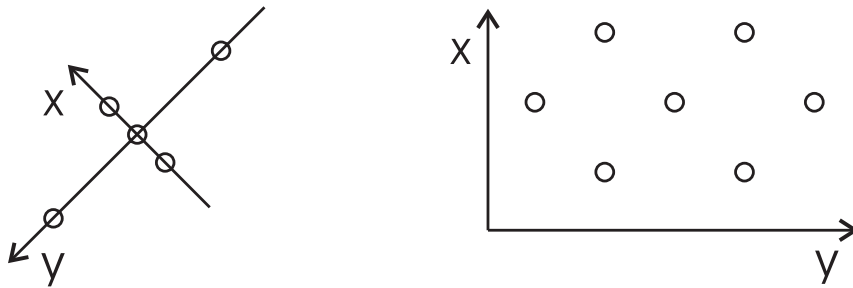


Figure 11: Structure of the (001) and (111) surfaces of a fcc crystal with a rhombohedral distortion in the paramagnetic phase. Note the changed orientation of the coordinate system for the (001) surface.

topographically equivalent to the (110) surface of the case A. The distortion only stretches the x or y axis, so the structure remains rectangular.

(111) surface. The analysis of the (111) surface (also depicted in Fig. 11 in the paramagnetic phase) in the subcase of only one monolayer reveals sets of symmetries very similar to the (110) surface, as it follows from the Table VII. In fact, the (111) surface of a fcc crystal with a rhombohedral distortion can be treated as two rectangular lattices superimposed on each other. In turn, due to the distortion, it is no longer convenient to describe the spin structures using “S” and “H” axes. The possibility to distinguish AF configurations is very poor, and two of the AF configurations (a) and k)) yield the same signal as the paramagnetic surface. In confs. b) - j), l), and m) the AF phase can be distinguished from the paramagnetic one, but they give the same signal as conf “ferro5”. Conf. “ferro2” can be easily distinguished since it reveals a characteristic set of (all) tensor elements. Confs. “ferro1” and “ferro3” yield different sets of tensor elements, but they are related to each other by a 90° rotation. Most of the configurations allow for the distinction of the cases A and B (compare Tabs. III and VII).

configuration	key (response type)
para	t
ferro1, ferro2, ferro4, ferro5	s
ferro3	t
AF:	
a), i), k)	s
b) - h), j), l), m)	t

Table VIII. SHG response for all spin configurations of the (111) surface of a fcc lattice, distorted to a rhombohedral structure. More monolayers are taken into account. For the detailed description of the response types see Tab. I. For the surface structure see Fig. 11, for the spin configurations see Fig. 10.

As the conclusion of the case of the distorted sublattice of magnetic atoms, the surfaces give extremely limited possibilities to investigate the magnetic properties, because of the limited symmetry already in the paramagnetic phase. In our further study, we will limit ourselves to lattices of undistorted magnetic atoms.

configuration	key (response type)
para	k
ferro1, ferro4	l
ferro2	m
ferro3	o
ferro5	n
AF:	
a), k)	k
b) - j), l), m)	n

Table VII. SHG response for all spin configurations of the (111) surface of a fcc lattice, distorted to a rhombohedral structure. Only one monolayer is taken into account. For the detailed description of the response types see Tab. I. For the surface structure see Fig. 11, for the spin configurations see Fig. 10.

In the subcase of two monolayers of the (111) surface, the symmetry is dramatically reduced (see Tab. VIII). Even in the paramagnetic phase the group of symmetries consists of only one nontrivial operation, and this occurs also in the AF configurations a), i), k), and “ferro3”. In all the other configurations all tensor elements are allowed due to the lack of any symmetry. Only confs. paramagnetic and “ferro5” allow for the unambiguous distinction of the cases A and B (compare Tabs. V and VIII). Consequently, this surface is not very useful to an analysis of the magnetic structure, with the exception of stating the distortion itself.

In brief, if the monoatomic lattice of magnetic atoms is distorted,

- all the surfaces, (001), (110), and (111), present poor possibilities for detection of the magnetic phase and the spin structure,
- the rhombohedral distortion can easily be detected, regardless of the magnetic phase of the material.

2.3.4 Case C: Structure with Nonequivalent Magnetic Atoms

We assume now that not all the magnetic atoms in the cell are equivalent. An example of such a structure is a material composed of two magnetic elements, but also a situation when the magnetic lattice sites are inequivalent due to different bonds to a nonmagnetic sublattice. Distortions of the sublattice of nonmagnetic atoms that preserve the center of twodimensional inversion (in the paramagnetic phase) produce the same effect. Other distortions of the sublattice of nonmagnetic atoms will be discussed in Subsec. 2.3.5. The magnetic moment at the distinguished positions can be changed or not - this does not affect the results obtained by the symmetry analysis. The configurations considered here are “ferro1”, “ferro2”, “ferro4”, a), b), c), e), f), i), k), m), o), p), and r) for the (001) surface (see Fig. 8), “ferro1”, ferro3”, “ferro5”, a), c), f), i), and k) for the (111) surface (see Fig. 10), and all configurations depicted in Fig. 9 for the (110) surface. Other depicted spin structures form domains of these configurations and are not referred to in this subsection nor in the tables concerning the current subsection.

configuration	key (response type)
para	a
ferro1	b
ferro2	vc
ferro4	d
AF:	
a), o)	h
b), e)	b
c)	f
f)	i
i), m), p)	e
k)	j
r)	d

Table IX. SHG response for all spin configurations of the (001) surface of a fcc lattice, with one atom distinguished. For the detailed description of the response types see Tab. I. For the surface arrangement see Fig. 12. For the confs. see Fig. 8.

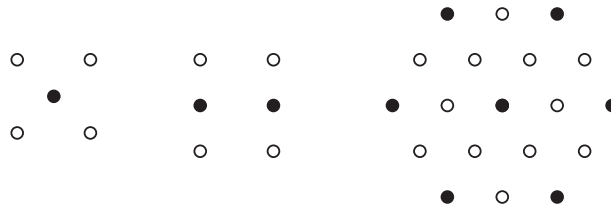


Figure 12: Surface structure of the non-equivalent magnetic atoms case in the paramagnetic phase. Pictures present the (001), (110), and (111) surfaces, respectively. Filled and empty circles represent the two kinds of magnetic atoms. Note, the fragment representing the (111) surface does not show the conventional unit cell but a bigger set of atoms in order to give a clear idea about the surface structure.

The structure is depicted in Fig. 12. For the sake of brevity, we show the structure of the distinguished atoms only for the paramagnetic phase. All the configurations are the

same as in case A, for all surface orientations. The already mentioned “convention” of alternating (or not) spin directions along certain axes is applied regardless of the atom type. This allows us to obtain the whole crystal surface from the small displayed fragment.

(001) surface. Our analysis starts with the (001) surface of an fcc crystal. The SHG response types for each configuration are listed in Table IX. In general, we can observe seven types of response. The first of them is represented by the paramagnetic phase alone. The second type of response, exhibited by the ferromagnetic “ferro1” and the AF a), b), e), o) confs., differs from any other type by some tensor elements. The confs. a) and o) reveal different tensor elements than the other configurations from the mentioned group. However, the signal from confs. a) and o) is the same as for the confs. b), e), and “ferro1” if one exchanges the axes x and y . Thus, if the directions of the spins cannot be determined by another method, confs. a) and o) cannot be distinguished from b), e), and “ferro1”. The next type consists of conf. f) and reveals all tensor elements, while no relations between them are enforced by the symmetry analysis. A completely different type of response is presented by conf. c) alone. Another type, where confs. i), m) and p) belong to brings the same tensor elements as conf. c), but there exist more relations between the elements due to a higher symmetry in these configurations. The next type is given by confs. “ferro2” and k). As in conf. f) all the tensor elements are present but this time there are some relations between them. In addition, confs. r) and “ferro4” yield a completely new set of tensor elements due to the preserved fourfold rotational symmetry.

Thus, assuming one atom as distinguished may reduce the symmetry. New tensor elements appear in confs. a), b), e), f), k), o), and r) compared to case A (compare Tabs. II and IX). In these configurations it is therefore possible to distinguish the cases of equivalent and nonequivalent magnetic atoms, provided the tensor elements that make the cases different can be singled out by the experimental geometry. There exists also a possibility to distinguish different AF configurations in case C. The antiferromagnetic *phase* can be undoubtedly detected in the surface configurations c), f), i), m), and p).

(110) surface. For the (110) surface, there are more possibilities to distinguish the configurations with nonequivalent magnetic atoms than in the case A. However, the configurations still produce ambiguous signals (see Tab. X). Confs. b), c), h), i), k), and l) are equivalent to the paramagnetic phase. Conf. a) is equivalent to the ferromagnetic “ferro1” configuration, and conf. d) to “ferro2”. In addition, the confs. e), f), and g) are equivalent to the conf. “ferro3” and conf. j) gives the same signal as conf. “ferro4”. Even the presence of nonequivalent atomic sites in the lattice cannot be detected by SHG on

configuration	key (response type)
para	k
ferro1	l
ferro2	m
ferro3	n
ferro4	o
AF:	
a)	l
b), c), h), i), k), l)	k
d)	1m
e), f), g)	n
j)	o

Table X. SHG response for all spin configurations of the (110) surface of a fcc lattice, with one atom distinguished. For detailed description of response types see Tab. I. For the surface arrangement see Fig. 12. For the confs. see Fig. 9.

this surface, since the symmetry of the (110) surface is usually not lowered further by the existence of nonequivalent magnetic sites (compare Tables III and X). The only exception are the confs. a), d), g), and j) which give different tensor elements in the two cases. As in the case of equivalent atoms, the (110) surface is not very useful for the analysis.

(111) surface. The study of the (111) surface must again be divided in the two subcases of one or more monolayers, respectively. Fig. 12 depicts the situation in the paramagnetic phase. The SHG response types are listed in Tables XI and XII for the first and the second subcase respectively.

In the first subcase (one monolayer) the symmetry establishes six different types of nonlinear response. The “paramagnetic” type (for the paramagnetic configuration only) is characteristic - all the other configurations have additional tensor elements. The next type of response (the ferromagnetic conf. “ferro1” and the antiferromagnetic conf. a)) brings some new tensor elements. Other tensor elements appear in the conf. k). Configurations “ferro3” and i) show another set of nonvanishing tensor elements. The confs. c) and f) reveal all tensor elements in an unrelated way. In addition, conf. “ferro5” presents a characteristic set of tensor elements.

configuration	key (response type)
para	p
ferro1	l
ferro3	o
ferro5	q
AF:	
a)	l
c), f)	m
i)	o
k)	n

Table XI. SHG response for all spin configurations of the (111) surface of a fcc lattice, with one atom distinguished. Only one monolayer taken into account. For the detailed description of the response types see Tab. I. For the surface arrangement see Fig. 12. For the confs. see Fig. 10.

configuration	key (response type)
para	r
ferro1	s
ferro3	t
ferro5	u
AF:	
a), c), f), k)	s
i)	t

Table XII. SHG response for all spin configurations of the (111) surface of a fcc lattice, with one atom distinguished. More monolayers are taken into account. For the detailed description of the response types see Tab. I. For the surface arrangement see Fig. 12. For the confs. see Fig. 10.

In the second subcase, only four different SHG responses are possible. Firstly, the paramagnetic phase is characteristic - all the other configurations bring additional tensor elements into play. The next type of response is presented by confs. “ferro3” and i) - they yield some additional tensor elements. Confs. “ferro1”, a), c), f), and k) reveal all tensor elements and no relations between them appear from our symmetry analysis. Again, the conf. “ferro5” presents a unique set of nonvanishing tensor elements.

Consequently, for the (111) surface, the symmetry breaking due to the presence of a second kind of magnetic atoms has even more important consequences than for the (001) surface. In the situation of only one monolayer, the distinction between the cases may be possible for all the AF configurations (compare Tables III and XI). Considering additional layers leads to further symmetry breaking and renders the distinction between the

configurations impossible. The distinction between the cases A and C is possible in confs. a) and k) (compare Tables V and XII). Besides, in most configurations it is possible to decide if these additional layers play any role (compare Tables XI and XII).

In the Case C, the conditions to distinguish the magnetic structure of the surface are less favorable than in the Case A. The presence of the second kind of atoms reduces the symmetry and can be (in most situations) detected by SHG. Also, one may distinguish AF spin configurations, at least at the (001) surface. In the next Subsection, we will address surfaces where, like in NiO, only one kind of magnetic atoms are present, but the distortion of the oxygen sublattice may result in a different SHG signal.

In brief, if two kinds of magnetic atoms are present (alloying),

- the (001) surface presents good possibilities to distinguish the spin configurations. In some configurations, a possibility to detect the AF phase exists,
- the (110) surface presents poor possibilities to detect of the magnetic structure,
- the (111) surface shows nearly no possibilities to detect of the spin structure, and the SHG signal of the AF phase is the same as for the ferromagnetic phase,
- the presence of the second kind of magnetic atoms can be detected in most situations (except for the (110) surface),
- the presence of the second kind of magnetic atoms slightly reduces the possibilities of detection of the AF phase.

2.3.5 Case D: Distorted Oxygen Sublattice

Due to the strong charge-transfer between nickel and oxygen in NiO the sublattices may be distorted. This effect can lower the symmetry of the surface. A point-charge model calculation by Iguchi and Nakatsugawa [47] presented a shift of the oxygen sublattice (“rumpling”) in the direction perpendicular to the surface. Their method did not show any in-plane displacement and thus no change of the surface symmetry. However, if the “rumpling” also has an in-plane component, i.e. if the oxygen atoms are displaced also in the x and y directions, it will also have a considerable effect on the symmetry of the crystal surface. For our analysis, we have chosen a distortion that can lower the symmetry of the surface and besides can be represented within one conventional unit cell. A slight non-stoichiometry of NiO (oxygen vacancies) can produce results qualitatively similar to the ones described in this subsection, however we will not focus on this issue. The configurations considered here are “ferro1”, “ferro2”, “ferro4”, a), b), c), e), f), i), k), m), o), p), and r) for the (001) surface (see Fig. 8), “ferro1”, ferro3”, “ferro5”, a), c), f), i), and k) for the (111) surface (see Fig. 10), and all configurations depicted in Fig. 9 for the (110)

surface. Other depicted spin structures form domains of these configurations and are not referred to in this subsection nor in the tables concerning the current subsection.

As will be shown later, the best conditions for the detection of this kind of distortion are presented by the (110) surface. The (111) surface could show equally good possibilities if only a monolayer of magnetic atoms is present.

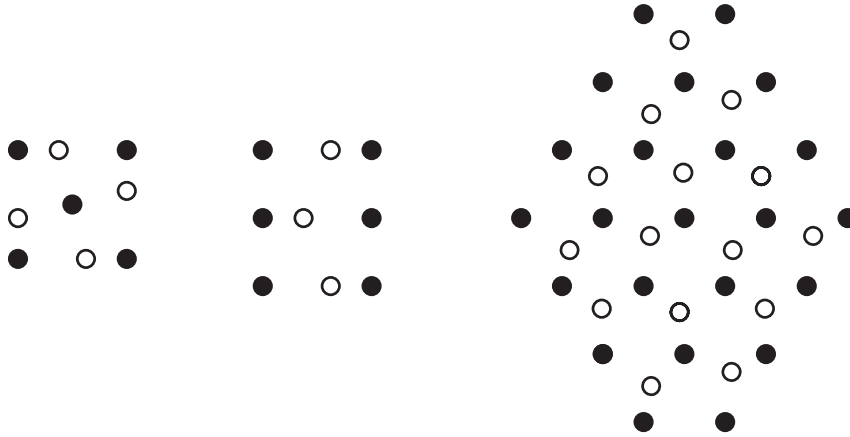


Figure 13: Surface structures of the case with a distorted oxygen sublattice (white circles). Pictures present the paramagnetic phase of (001), (110), and (111) surfaces, respectively. Note, the fragment representing the (111) surface does not show the conventional unit cell but a bigger set of atoms in order to give a clear idea about the surface structure.

In the presence of an oxygen sublattice distortion, the chemical unit cell is also doubled. This effectively means that magnetic unit-cell-doubling (describing the fact that the magnetic unit cell is twice as big as the chemical one) is lifted. In general, taking into account distorted oxygen atoms in the paramagnetic phase does not lower the symmetry of the problem. The exception is the (111) surface, where the six-fold axis is replaced by the three-fold one.

In the case of the distorted oxygen sublattice, the symmetry group for each configuration is a subgroup of the corresponding “non-distorted” configuration, i.e. of the corresponding spin configuration in the case A. As in case C we display only the paramagnetic phase in Fig. 13 to depict the atom positions. All the spin configurations are the same as for the corresponding surfaces in case A, and the spins are assumed to be equivalent.

(001) surface. As Table XIII shows, six different responses can be expected from the (001) surface. The paramagnetic surface will give a characteristic response. The second group is formed by the confs.: a), b), e), o), and “ferro1”. Although confs. a) and o) have elements

configuration	key (response type)
para	a
ferro1	b
ferro2	c
ferro4	d
AF:	
a), o)	h
b), e)	b
c), f)	i
i), k)	c
m)	j
p)	e
r)	d

Table XIII. SHG response for all spin configurations of the (001) surface of a fcc lattice, with a distortion of oxygen sublattice. For the detailed description of the response types see Tab. I. For the surface arrangement see Fig. 13. For the confs. see Fig. 8.

different from the remaining configurations in this group, this fact corresponds simply to rotating the sample by 90° with respect to the z axis. Confs. c) and f) reveal all tensor elements without relations between them. Confs. “ferro2”, i), k), and m) reveal all tensor elements with some relations. The only difference between conf. m) and others from this group is like for the previous group a 90° rotation with respect to the z axis. Another group consists of conf. p) alone. It reveals the same tensor elements as the paramagnetic phase, but certain relations between tensor elements are broken due to a lower symmetry of the conf. p). The confs. r) and “ferro3” form the last group. All the configurations but k) and “ferro3” can be distinguished from those of case A (compare Tabs. II and XIII). However only confs. c) and g) can be distinguished from case C (compare Tables IX and XIII). Thus, only in these configurations it will be possible to detect oxygen sublattice distortions by SHG.

configuration	key (response type)
para	k
ferro1	l
ferro2	m
ferro3	n
ferro4	o
AF:	
a), b), g), h), k), l)	k
c)	o
d), e), i), j)	n
f)	m

Table XIV. SHG response for all spin configurations of the (110) surface of a fcc lattice, with oxygen sublattice distorted. For the detailed description of the response types see Tab. I. For the surface arrangement see Fig. 13. For the confs. see Fig. 9.

(110) surface. The SHG response types for the (110) surface are presented in Table XIV. One can observe that only configurations c), f) and i) give rise to new (compared to case A, Table II) tensor elements. Compared to case C (Table X), confs. c), f), and i) bring new tensor elements, and, surprisingly, confs. a) and g) have less tensor elements, due to higher symmetries in the case D. Consequently, the confs. a), c), f), g), and i) allow for an unambiguous determination of the oxygen sublattice distortion from the (110) surface. The possibility to distinguish different configurations is rather limited.

(111) surface. Oxygen sublattice distortion similar to the one presented in Fig. 13 for a (111) surface was found by Renaud *et al.* [48] and calculated by Gillan [49] in M_2O_3 materials ($M = Al, Fe$). Since the nonmagnetic sublattice symmetry group has an influence on SHG this distortion can be detected also on surfaces of fcc crystals. In the previous cases A and C we divided the study of (111) surfaces in two subcases, considering either one or more atomic layers. Taking into account a distorted oxygen sublattice leads us immediately to the subcase of “more atomic layers”. It is caused by the fact that, on (111) surfaces, the oxygen and magnetic atoms belong to mutually exclusive planes. The resulting SHG response types are listed in Table XV. For the AF and ferromagnetic phases, all tensor elements are allowed for every configuration. Thus SHG cannot detect the magnetic phase of the surface nor distinguish different configurations. Only confs. paramagnetic, “ferro3”,

“ferro5”, and d) allow to decide unambiguously whether the oxygen sublattice is distorted or not (compare Tabs. V, XII, and XV).

For both the (001) and (111) surfaces, the symmetry groups of case D appear to be the subgroups of the corresponding configurations of case C. This means that the oxygen sublattice distortion makes some (one half of all) magnetic atoms distinguished as in case C, even though we did not apply this distinction explicitly in case D. On the other hand, the symmetry groups of the case D differ clearly from those of case B. This is caused by the difference in distortions assumed in these cases: the rhombohedral one in case B and rotation-like in case D.

The distortion of the oxygen sublattice diminishes the possibilities to detect the magnetic structure of the surface. Only for the (001) surface one may distinguish the magnetic phases by SHG.

configuration	key (response type)
para	u
ferro1, ferro3	w
ferro5	u
AF:	
All confs.	w

Table XV. SHG response for all spin configurations of the (111) surface of a fcc lattice, with oxygen sublattice distorted. For the detailed description of the response types see Tab. I. For the surface arrangement see Fig. 13. For the confs. see Fig. 10.

In brief, the distortion of the oxygen sublattice¹⁶

- is possible to detect on (110) and (111) surfaces,
- renders the determination of the spin structure impossible (on all surfaces),
- makes the distinction of the magnetic phases difficult. Only on the (001) surfaces the AF phase can be unambiguously detected.

2.3.6 Second Atomic Layer

In the previous subsections, we took into account the spin structure only for the first (uppermost) atomic layer. For the (111) surfaces, we also addressed the role of the presence (but not the spin structure) of magnetic atoms lying deeper, since this could (and usually did) change the symmetry of the described structure even in the paramagnetic phase. On the other hand, taking into account the positions of the atoms in deeper layers does not change the symmetry for the (001) and (110) surfaces. In this subsection, we present a study of the low index surfaces with more than one layer taken into account, addressing also the spins of the magnetic atoms for the simple (undistorted) case, i.e. case A. The structures described here can serve as simple models for deriving predictions for

¹⁶Or the mentioned non-stoichiometry.

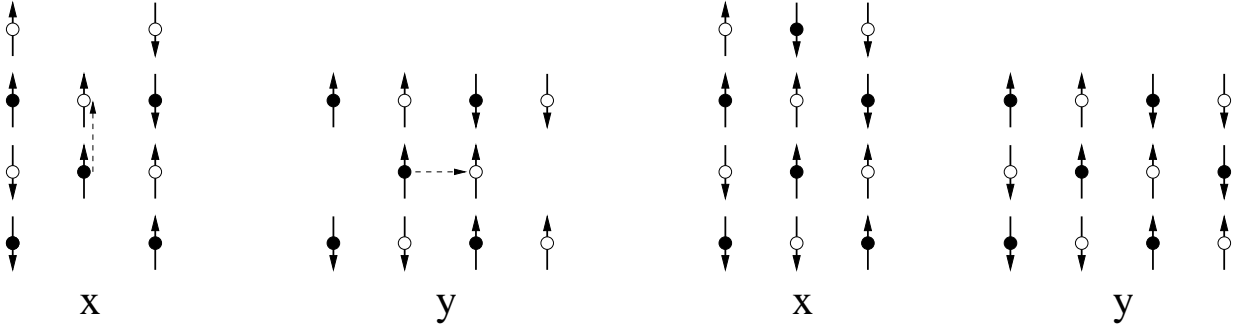


Figure 14: Spin structure of an antiferromagnetic (001) bilayer constructed from a shift of the monolayer along the positive x (y) axis. Filled (empty) circles represent the topmost (second) layer. On the right hand side the conventional unit cells for the resulting bilayer structure are presented. Here, conf. c) of the (001) monolayer serves as an example.

more complicated cases, while the full consideration of the second layer in the other cases (B, C, and D) would not bring any new interesting results. Also, considering more than two layers will not bring any new results, thus our analysis *completely* describes the antiferromagnetic surfaces.

Taking into account the spin structure of the second layer results in creating several (up to two for the (001) surface and three for the (111) surface) configurations out of each one addressed here by us. The symmetry of these configurations may remain the same or be lowered (sometimes even below the symmetry of the ferromagnetic phase) with respect to the “two-dimensional” configurations they are generated from. Consequently the distinction of the configurations from each other may be limited, but the possibility to detect the magnetic phase is not severely affected. Also our remarks on domain imaging remain valid, however the number of domains is increased.

(001) surface. The paramagnetic phase and all the ferromagnetic configurations of the (001) surface remain unchanged with respect to the results of the Subsec. 2.3.2 (for the (001) monolayer). However, most of the AF configurations previously addressed break up into two different configurations (sometimes even with a different symmetry). These configurations are constructed from the ones of the previous paragraph by assuming that the structure of the second atomic layer is identical with that of the topmost one but shifted along the positive x axis (indicated by x after the name of the original configuration) or positive y axis (indicated by y after the name of the “parent” configuration) in a proper way to form a fcc structure; if only one configuration can be produced in this way we

configuration	key (response type)
para	a
ferro1	b
ferro2	c
ferro4	d
AF:	
ax), ox)	h
ay), oy), r)	e
bx), by), ex), ey)	b
c), fx), fy)	i
i)	j
k)	f
m), p)	c

Table XVI. SHG response for all spin configurations of the (001) surface of a fcc lattice, with the spin structure of the second layer taken into account. For the detailed description of the response types see Tab. I. For the confs. see Fig. 8.

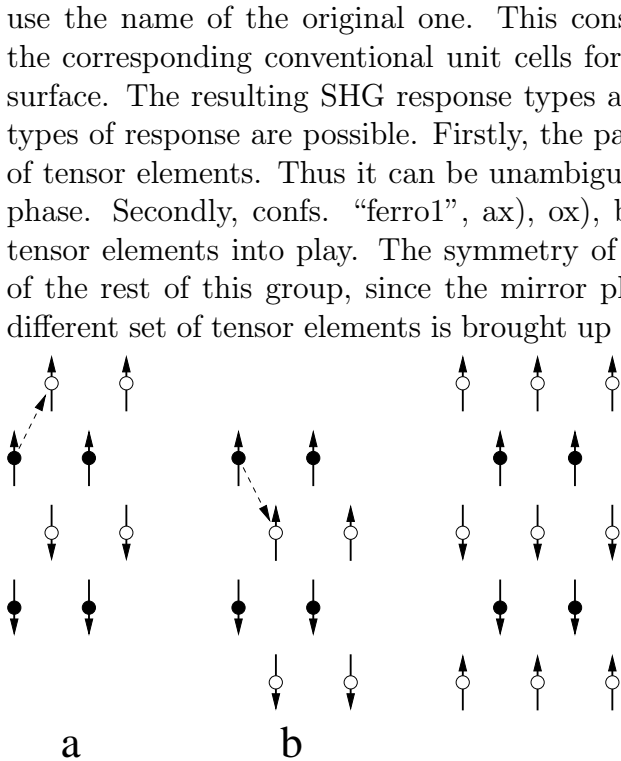


Figure 15: Spin structure of an antiferromagnetic (110) bilayer constructed from a shift of the monolayer, where two different shiftings are applied. Filled (empty) circles represent the topmost (second) layer. The rightmost panel shows the conventional unit cell for the resulting bilayer structure. Here, conf. a) of the (110) surface serves as an example.

are slightly worse than those for a monolayer. Especially, a difficulty in distinguishing the ferromagnetic phase from the antiferromagnetic one may arise for some configurations where then the combination of SHG with other methods is definitely required. There exists a possibility to distinguish AF configurations from each other, similarly to the previous situation. In most configurations, the difference (in terms of the SHG response) between the bilayer structure described here and the previously addressed (001) monolayer can be detected.

(110) surface. The previously described AF configurations of the (001) monolayer most commonly get split into two different configurations when a bilayer structure is considered. For the (110) bilayer it is not the case - only two of twelve AF configurations get split in this way, thus one obtains 14 AF configurations of the (110) bilayer. Describing the results of our analysis we use the nomenclature of our previous article, i.e. the antiferromagnetic configurations are labeled by small letters. Only the four configurations that result from splitting of the two configurations of the monolayer structure are labeled by small letters with subscripts that carry the information about how they have been constructed from the (110) monolayer. For configurations with subscript “a” the lower layer is constructed by translation of the topmost layer by vector $(0.5a, 0.5b)$, where a and b are interatomic

use the name of the original one. This construction is depicted in Fig. 14, along with the corresponding conventional unit cells for the two topmost layers of the AF fcc (001) surface. The resulting SHG response types are presented in Table XVI. In general, seven types of response are possible. Firstly, the paramagnetic phase reveals a characteristic set of tensor elements. Thus it can be unambiguously distinguished from any other magnetic phase. Secondly, confs. “ferro1”, ax), ox), bx), by), ex), and ey) bring some additional tensor elements into play. The symmetry of confs. ax) and ox) is different from the one of the rest of this group, since the mirror plane is rotated by 90° around the z axis. A different set of tensor elements is brought up by confs. “ferro2”, i), m), and p). The difference between the response yielded by conf. i) and the other confs. in this group, due to a different symmetry, can be compensated by rotating the sample by 90° around the z axis. Another, characteristic set of tensor elements is presented by conf. “ferro4” alone. The fifth type of SHG response is given by confs. ay), oy), and r). Tensor elements, that do not vanish in these configurations, are the same as for the paramagnetic phase but some relations between them are broken due to a lower symmetry in the AF phase. Confs. cx), fx), and fy) yield all tensor elements in an unrelated way. The last, characteristic type of response is presented by conf. k) alone. Consequently, the detection possibilities of an antiferromagnetic bilayer

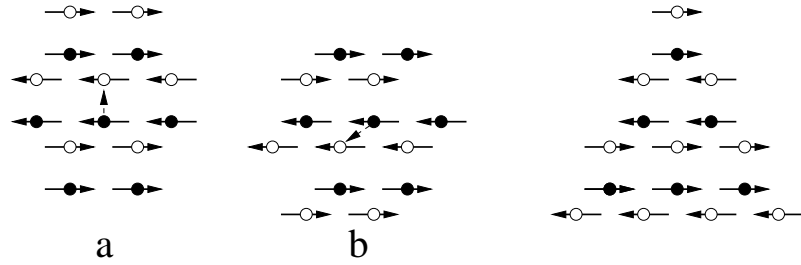


Figure 16: Spin structure of an antiferromagnetic (111) bilayer constructed from a shift of the monolayer, where two different shiftings are applied. Filled (empty) circles represent the topmost (second) layer. Here, conf. f) of the (111) monolayer serves as an example. The rightmost panel displays the conventional unit cell for the resulting bilayer structure of conf. f_a).

distances *within* the (110) plane along x and y axes, respectively. For configurations with subscript “b” the vector of translation is $(-0.5a, 0.5b)$. This corresponds to the way we constructed the (001) bilayers.

The configurations of the (110) monolayer structure are depicted in Fig. 9, and the way the bilayer is constructed is depicted in Fig. 15. The tensor elements are presented in Table XVII. In general, we can observe five types of response. However, the possibility to distinguish AF configurations is not much improved compared to the (110) monolayer. Even the possibility to detect the magnetic phase of the surface is not evident.

As for the (001) surface, there is no difference in SHG signal between the monolayer and bilayer for the paramagnetic and ferromagnetic phases. For most AF configurations, however (confs. a), b), c), e), f_a , f_b), g), h), j), k), and l)) such a difference is present due to a lower symmetry of the bilayer.

configuration	key (response type)
para	k
ferro1	l
ferro2	m
ferro3	n
ferro4	o
AF:	
a), g), j)	o
b), h), k)	l
c), d), l)	n
e), f_a), f_b)	m
i_a), i_b)	k

Table XVII. SHG response for all spin configurations of the (110) surface of a fcc lattice, with the spin structure of the second layer taken into account. For the detailed description of the response types see Tab. I. For the confs. see Fig. 8.

(111) surface. The spin configurations of the (111) bilayer are constructed from the configurations of the (111) surface of our previous work in the way that the spin structure in the second atomic layer is the same as in the topmost layer, but shifted accordingly to

configuration	key (response type)
para	r
ferro1	s
ferro3	t
ferro5	u
AF:	
$a_a), a_b), i_a),$	
$i_b), k_a), k_b)$	t
$c_a), c_b), f_a), f_b)$	s

Table XVIII. SHG response for all spin configurations of the (111) surface of a fcc lattice, with the spin structure of the second layer taken into account. For the detailed description of the response types see Tab. I. For the confs. see Fig. 10.

atoms in the second layer does.

form a hcp structure. Taking into account the spin structure of the second layer causes all the AF configurations to split, thus one obtains 10 AF configurations of the (111) bilayer. The configurations are labeled by small letters (indicating their “parent” configuration) with subscript “a” if the mentioned shifting is along the positive x axis, and “b” if the shifting is along the negative S_{xy} axis.

The configurations of the (111) monolayer are depicted in Fig. 10 and the construction of the bilayer is depicted in Fig. 16. The corresponding tensor elements are displayed in Tab. XVIII. The results are identical to those of the Subsec. 2.3.2, where the second layer of the (111) surface was present but treated as nonmagnetic. This means that the spin structure of the second layer does not play any role for SHG, however the presence of the

In brief,

- (001) surface presents the best possibilities to detect the magnetic phase and the spin structure of the material.
- These possibilities on the (110) surface are limited.
- The results for the (111) surface are the same as in Subsec. 2.3.2.
- In general, the presence of the second atomic layer (and deeper ones) does not invalidate our remarks that SHG is able to detect the magnetic phase and the spin structure of the surface.

2.3.7 Domain Imaging

So far, we have described the possibilities to detect the AF phase and various spin structures on AF surfaces by means of SHG. Another interesting application of SHG is domain imaging in AF materials. As we already pointed out, Fiebig *et al.* [4] were the first to image AF bulk domains in Cr_2O_3 . Here, we will analyze the possibilities for the domain imaging on AF *surfaces*.

For simplicity, we will consider here only surfaces described hitherto by the case A of our analysis. In this case, for AF surfaces, no 180° domains can be expected due to the presence of magnetic unit-cell doubling. The allowed domains can be detected by surface-sensitive SHG under the following two conditions.

First, domains can be imaged by our method only if they manifest themselves at the surface, i.e. if the surface spin ordering changes while passing from one domain to another¹⁷. It is necessary to note, however, that the spin orderings for different domains must belong to the same *configuration* in the sense of our classification. We do not consider it as a domain structure if one portion of the surface is in one configuration and another portion is in a different configuration. Under such conditions, we can encounter two different types of domains: 90° domains (for the (111) surface they are rather 60° domains), resulting from the rotations around the z axis, and the second type (called by us mirror-domains, characteristic for antiferromagnets), where spins point along the same axis in all domains, but the ordering is still different (they are no 180° domains!). The tables contain the complete information about the domain-parity of tensor elements in mirror-domain operations, and also for 90° type domains, but not for 60° domains. The 90° type domains will be addressed later on. In the mirror-domain structure, the magnetic point group describing the configuration must lack an operation that, while belonging to the (nonmagnetic) point group of the system *and* leaving the spin axes invariant, only flips some of the spins. Note, the flipped subset of the spins must be antiferromagnetically ordered in itself. Configurations, the symmetry groups of which *lack* one of these operations can reveal surface domains, related to each other by this operation.

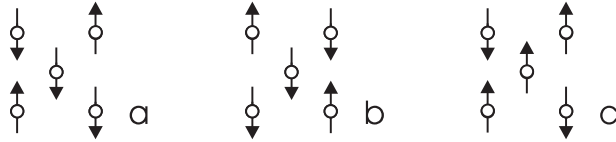


Figure 17: Two surface mirror domains for an AF configuration - panels b) and c) depict the same AF domain, related to the panel a) by different mirror operations.

For an illustration we choose the configuration c) of the (001) surface (see Fig. 8), one of the configurations characteristic for NiO. The spins point along the x axis. Thus operations leaving the axis invariant are $\bar{2}_x$, $\bar{2}_y$ and 2_z . Of them, $\bar{2}_x$ and $\bar{2}_y$ are absent in the magnetic point group of the considered configuration (see Tab. II, conf. c), and Tab. I). The flipped subset of spins consists of the four outer spins for the $\bar{2}_x$ operation, and of the central spin for $\bar{2}_y$ (see Fig. 17 b) and c), respectively). In fact, there are two domains possible in this configuration: one with the spins kept invariant under translations by the vector $(-\frac{a}{2}, \frac{a}{2}, 0)$ (this domain is shown) and the other with the spins kept invariant under translations by the vector $(\frac{a}{2}, \frac{a}{2}, 0)$. Here, a denotes the lattice constant. These domains are depicted in Fig. 17.

The second condition for domain imaging is an interference. It can be created internally by different elements of the tensor $\chi^{(2\omega)}$ or by external reference [50, 51]. The interfering elements should be of a similar magnitude for the largest possible image contrast. Group theory, however cannot account for the amplitudes. With external as well as internal reference, a tensor element that changes its sign under the reversal of the antiferromagnetic order parameter \mathbf{L} is necessary. Actually, every \mathbf{L} dependence of $\chi^{(2\omega)}$ can be represented

¹⁷It is also possible for different bulk domains to yield the same spin ordering at the surface.

by splitting the tensor elements into odd and even ones in \mathbf{L} ; even if a tensor element is not purely odd or even we can always decompose it according to Eq. (2.6), i.e. a tensor element consists of parts which are odd and even in \mathbf{L} , respectively. In a system with many terms of that kind the possibility of detecting domains may be limited, since they can influence the signal with opposite sign, thus diminishing the interference. In highly symmetric structures, such as an fcc crystal, the situation is more comfortable: every tensor element is either odd or even in \mathbf{L} (see Subsec. 2.2.2). By the appropriate set of experiments an element can be singled out and give a clear image of AF domains.

Using our example, conf c) of the (001) surface, we see that in the s-output polarized light only two tensor elements are present¹⁸: $\chi_{yyz}^{(2\omega)}$ and $\chi_{yzx}^{(2\omega)}$. The first of them is even while the second is odd under the domain operation $\bar{2}_x$. The resulting SHG light I_S can thus be expressed as (compare Eq. (2.2)):

$$I_S \sim (\chi_{yyz}^{(2\omega)})^2 + (\chi_{yzx}^{(2\omega)})^2 \pm 2\chi_{yyz}^{(2\omega)} \cdot \chi_{yzx}^{(2\omega)} \quad (2.7)$$

where “+” stands for one domain, “-” for a different one. The change of sign of one tensor element results in the domain contrast.

Now, we turn to the 90° domain structure. Again, we take the conf. c) of the (001) surface as an example. The operation connecting the domains is 4_z . Under this operation, the tensor element $\chi_{zxy}^{(2\omega)}$ changes its sign, thus again we have an interference which renders the domain imaging possible. This tensor element is even in the domain operation $\bar{2}_{xy}$ (which is equivalent to the superposition of $\bar{2}_x$ and 4_z), which means that domains related to each other by this operation cannot be imaged using this particular tensor element. Similarly, if a tensor element is odd in one domain operation and even in another, it must be odd in their superposition.

It is necessary to mention at this point that taking into account the spin structure in the *second layer* would not change the validity of the analysis presented in this subsection. The only modifications would result from addressing bulk domains rather than surface domains, and the symmetry of the AF configurations would be changed. Yet it would still be possible to find domain operations as well as odd and even tensor elements leading to interference and AF domain contrast. Only in some cases the possibility to identify each of the domains may be limited due to the increased number of domains.

2.3.8 Possible Experimental Results

In this subsection, we propose and discuss possible experimental setups for the detection of AF configuration and the imaging of AF domains from low-index surfaces of NiO that exhibit magnetic unit-cell doubling in contrast to bulk Cr_2O_3 [5, 24]. We propose an experimental setup for the *detection* of antiferromagnetism in the following way: both the incident and reflected beams may lie in the xz plane (optical plane), and form the angle ϑ with the z -axis (normal to the sample surface). In the plane perpendicular to the outgoing

¹⁸For simplicity, the result of the symmetry analysis of a monolayer (case A) are used here. The tensor elements resulting from a bilayer (Subsec. 2.3.6) do not hamper the possibility of domain imaging, but would make the presentation more cumbersome due to the enhanced number of tensor elements.

beam axis, the electric field of the second-harmonic generated light has two components, $E_p^{(2\omega)}$ and $E_s^{(2\omega)}$, given by the formulae

$$\begin{aligned} |E_p^{(2\omega)}| &= |\cos \vartheta E_x^{(2\omega)} - \sin \vartheta E_z^{(2\omega)}| \\ |E_s^{(2\omega)}| &= |E_y^{(2\omega)}| \end{aligned} \quad (2.8)$$

$E_x^{(2\omega)}$, $E_y^{(2\omega)}$, and $E_z^{(2\omega)}$ are the components of the electric field resulting from SHG in the coordinate system of the sample. The dependence of these components on the input electric field is indicated by the tensor $\chi^{(2\omega)}$. The aim of the experiment is the determination of vanishing and nonvanishing tensor elements. The easiest way to do this is to analyze the output signal intensity as a function of the input polarization in both output polarizations s and p , for a fixed angle of incidence and reflection. The dependence of the output second-harmonic electric field on the input polarization is schematically displayed in Fig. 18 for all tensor elements. The intensity of SHG light is the square of the linear combination of these partial responses. Examples of the intensity dependence on the input polarization is presented in Fig. 19 for all the magnetic phases. The intensity need not be symmetric with respect to $\varphi = 90^\circ$, this results from the influence of the electric field depicted in Fig. 18c). The coefficients of the mentioned combination are the products of the $\chi^{(2\omega)}$ tensor elements and the corresponding Fresnel coefficients, according to Eq. (2.2). Thus performing a best fit of these coefficients to the experimental results will give (after taking into account the Fresnel and geometrical coefficients, known for the given experimental geometry and material [42]) a set of non-vanishing elements of the $\chi^{(2\omega)}$ tensor. Thus for instance, the magnetic phase can be determined.

Concerning another experimental geometry, with input polarization fixed and intensity measured as a function of the output polarization, it is possible to determine whether the nonlinear Kerr effect takes place. For instance, with the input polarization $\varphi = 90^\circ$, the output electric field is given as follows [42]:

$$E^{(2\omega)} = \sin \Phi (A_2(\Theta) \chi_{yyy}^{(2\omega)} B_2(\vartheta)) + \cos \Phi (A_1(\Theta) \chi_{xyy}^{(2\omega)} B_2(\vartheta) + A_3(\Theta) \chi_{zyy}^{(2\omega)} B_2(\vartheta)) \quad (2.9)$$

As the result, maximum of the intensity is for $\Phi \neq 90^\circ$, if at least one of the tensor elements $\chi_{xyy}^{(2\omega)}$ or $\chi_{zyy}^{(2\omega)}$ does not vanish. Actually, tensor element $\chi_{xyy}^{(2\omega)}$ is even in all the investigated order parameters, but the tensor element $\chi_{zyy}^{(2\omega)}$ can be odd. For such configurations the Kerr effect (change of polarization caused by inversion of the magnetic order parameter) takes place. Thus, it is possible to determine which tensor elements are associated with the spin-orbit coupling.

The geometry with p polarization of the reflected SHG light seems to be less useful, since there the tensor element $\chi_{zzz}^{(2\omega)}$ is always present, regardless of the configuration. Besides, this polarization mixes the $\chi_{x..}^{(2\omega)}$ and $\chi_{z..}^{(2\omega)}$ tensor elements. This mixing, however, can be tuned by varying the angle of incidence ϑ and taking into account the influence of the Fresnel coefficients. For smaller ϑ only the $\chi_{x..}^{(2\omega)}$ elements are important, while for larger ϑ the $\chi_{z..}^{(2\omega)}$ dominate. If the experiment does not show any difference for these two situations, the tensor elements must be related. This is the possibility to distinguish the configurations with some relations between the tensor elements from those without such

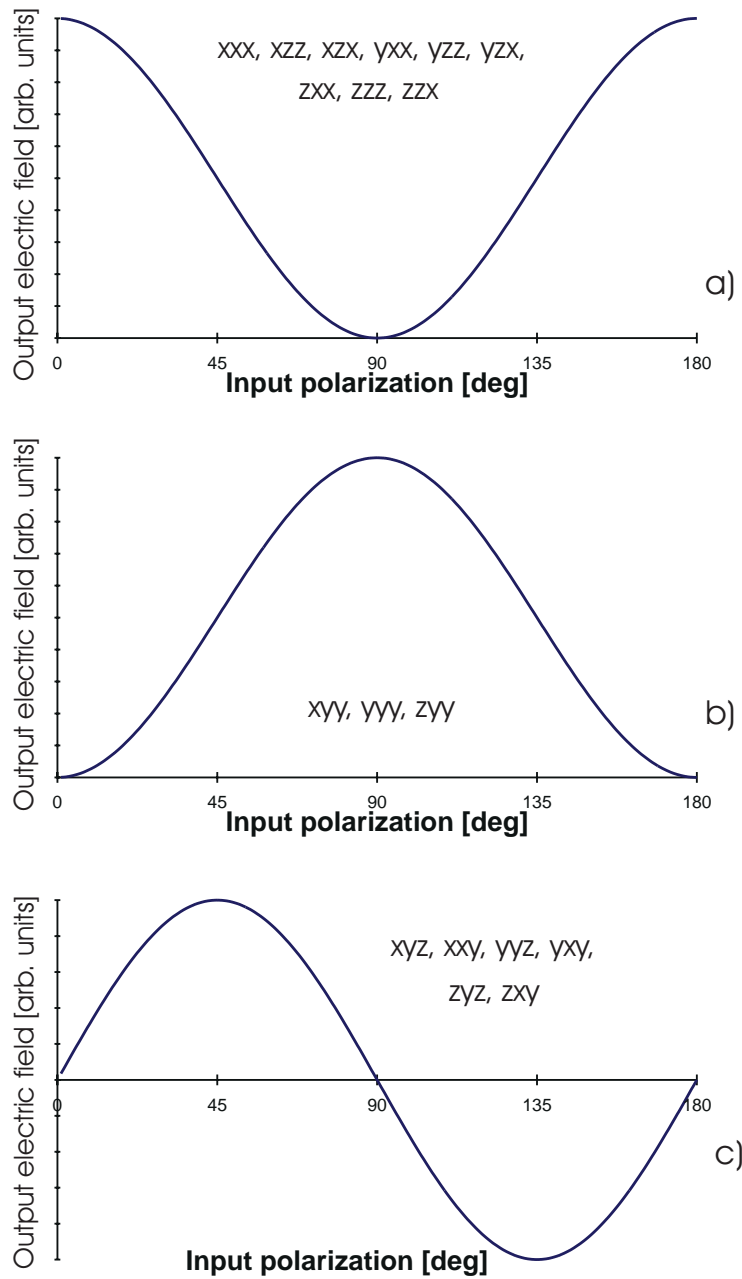


Figure 18: Electric field response of single tensor elements as a function of the input polarization. Tensor element $\chi_{ijk}^{(2\omega)}$ is denoted as ijk .

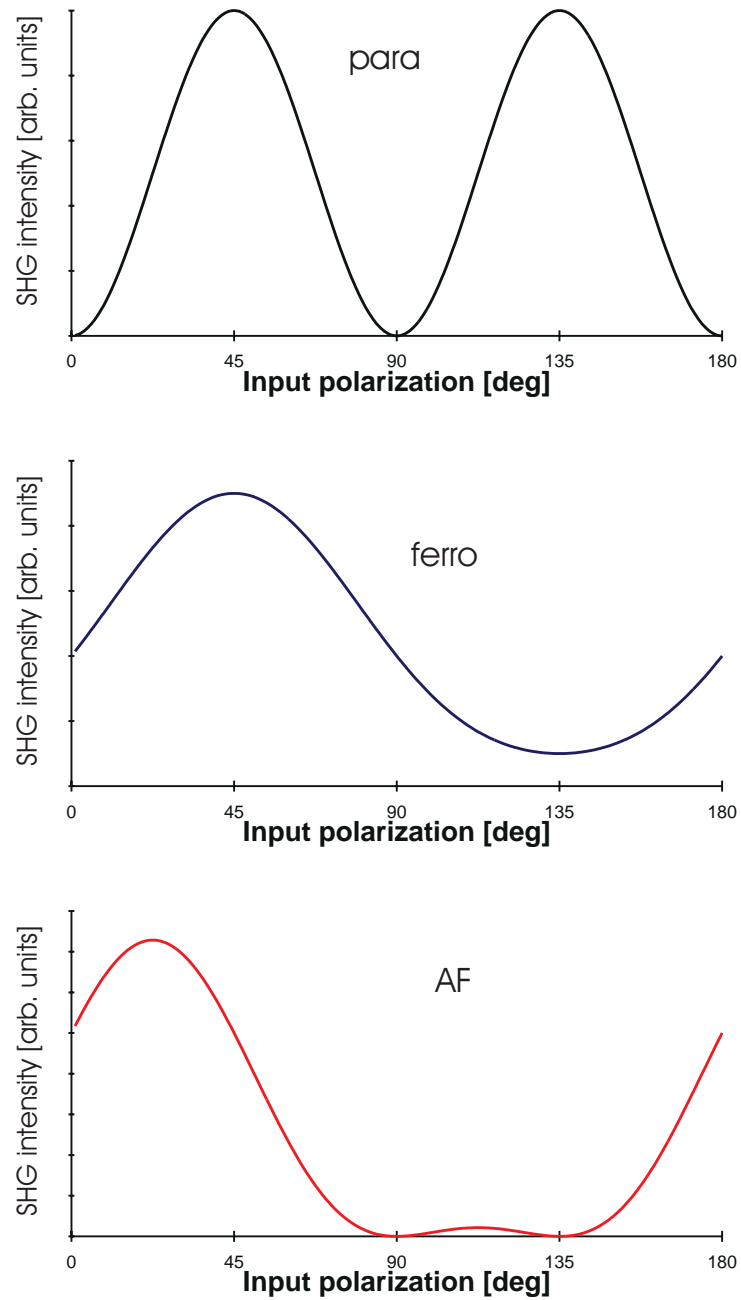


Figure 19: SHG intensity in S-output geometry for different magnetic phases.

relations. On the other hand, the s polarization gives better chances for singling out the desired tensor elements.

The surface, which gives the best possibilities of drawing practical conclusions in an experiment, is the (001) surface. This is true not only for monolayers with an undistorted structure, as described by Dähn *et al.* [40], but also in case of a real surface (as represented by our analysis of a bilayer structure). In particular, Fig. 19 shows the possibility of distinguishing magnetic phases of the (001) surface¹⁹, which, in the case of the structures presumed for NiO, remains valid both for the monolayer and the surface. The most important difference between the paramagnetic and the both magnetically ordered phases is the fourfold symmetry of the SHG response for the first one. Two minima in the response of the AF surface clearly distinguish it from the ferromagnetic phase. In the real experiments, these minima need not be separated by 45° , nor the response needs to fall to zero. Both these features depend on the relative complex phase and magnitude of the tensor elements. As our electronic calculation in Chapter 3 hints, one can choose such a wavelength that the tensor elements are similar, with respect to the complex phase *and* the magnitude. Thus, one can expect the experimentally obtained polarization dependence of SHG to be similar as in Fig 19c).

In brief, the features of the experimental s-polarized SHG response from the (001) surface are expected to be as follows:

- paramagnetic phase: fourfold symmetry.
- ferromagnetic phase: twofold symmetry, one minimum.
- antiferromagnetic phase: twofold symmetry, two minima.
- domain imaging: both 90° and mirror domains possible to image.

2.4 Time Reversal

As was discussed in the previous sections, symmetries determine the optical response of a crystal. In magnetic materials, time-reversal is believed to be of fundamental importance since this operation reverses all magnetic moments [8, 24, 29]. However, the consequences of applying time-reversal are more profound than a simple inversion of localized magnetic moments. As it will turn out in the current section, there is a deep interrelation between the absence of conventional dissipation in even-order (e.g. second) harmonic generation and the influence of time-reversal on spin ordering. This brings about a subtle difference between time-reversal and spatial symmetries in nonlinear optics. The benefit of this difference makes optical second harmonic generation (SHG) a rather unique probe of antiferromagnetism, while linear optics (where dissipation in the conventional sense is possible) is blind for such balanced spin structures. The recent discussion about the influence

¹⁹The ferromagnetic configuration “ferro1” and the AF configuration c) were used to obtain the graphs.

of micro-irreversibility on macro-reversibility and reciprocity ([52, 53, 54]) shows that the issue of time-reversal, although extensively discussed, is far from being understood.

In this section, we will:

- present the contemporary status of applying of the time-reversal operation in the symmetry analysis,
- discuss the issue of two kinds of dissipation in nonlinear magneto-optics,
- analyze the reversibility of an elementary process of SHG, and
- propose a novel operation which is better suited for the symmetry analysis of non-linear magneto-optics.

2.4.1 Conventional Approach

In considering the time-reversibility of an experimental situation, three approaches are possible: (i) time-reversal is applied to the sample, but all the processes resulting from the experiment are unchanged. In particular, the magnetic moments in the sample are reversed, but the direction of the light propagation through the sample is not affected. This approach is presented e.g. in [55, 56]. We consider this approach as incomplete, since it does not equally treat the sample and the light propagating through it. (ii) The second approach, usually encountered in the so called Sagnac-interferometry, addresses time-reversal by reversing the propagation of the light through the sample (see, e.g. [57, 58, 59]). Clearly, such procedure probes the *reciprocity* [60] of the sample rather than its time-reversal symmetry. It can also be proven that the second approach is equivalent to the first one. (iii) According to the third approach, presented e.g. in [61], time reversal acts on *both*: the sample and the experimental setup. In this work, we follow approach (iii).

2.4.2 Dissipation in SHG

In the processes of even-order harmonic generation, dissipation in the conventional sense, converting radiation into heat, does not exist, since the energy loss of the electromagnetic field is the time average [38]

$$-\left\langle \frac{dP(t)}{dt} E(t) \right\rangle, \quad (2.10)$$

which vanishes for SHG (and all even-order harmonics), since

$$\begin{aligned} P(t) &\sim P_0 e^{i\omega t} \\ E(t) &\sim E_0 e^{i2\omega t} \end{aligned} \quad (2.11)$$

Here, P and E denote the polarization of the medium and the electric field, respectively²⁰. The lack of dissipation in the conventional sense does not mean that the process of SHG is reversible. Already the analysis by Armstrong *et al.* [62] assumes a unique time direction. There, the nonlinear polarization \mathbf{P}^{NL} and the electric field \mathbf{E}_3 of a light beam resulting from Sum Frequency Generation at a point r_0 is given by:

$$\mathbf{P}^{NL}(\omega_3) \sim \frac{1}{2} \text{Re} \left[e^{i(\Delta \mathbf{k} \cdot \mathbf{r}_0 + \Delta \phi)} e^{i(\mathbf{k}_3 \mathbf{r}_0 - \omega_3 t + \phi_3)} \right] \quad (2.12)$$

$$\mathbf{E}_3 \sim \text{Re} \left[e^{i(\mathbf{k}_3 \cdot \mathbf{r}_0 - \omega_3 t + \phi_3)} \right], \quad (2.13)$$

see eqs. (3.1) and (3.2) of Ref. [62]. Here, ω_3 and k_3 describe the frequency and wave vector of the generated light ($\omega_3 = \omega_1 + \omega_2$ and $\mathbf{k}_3 \approx \mathbf{k}_1 + \mathbf{k}_2$). The authors introduce the idea of “work done on this wave” by the nonlinear polarization of the medium, equal to

$$W_3 = \frac{\omega_3}{2\pi} \int_{\text{cycle}} \mathbf{E}_3 \frac{d\mathbf{P}^{NL}(\omega_3)}{dt} dt = \frac{1}{2} \omega_3 \mathbf{E}_3 \mathbf{P}^{NL}(\omega_3, \text{out-of-phase}), \quad (2.14)$$

if the polarization is exactly 90° out of phase with the electric field (which requires that $\Delta k_z z + \Delta \phi = \pi/2$). The work done on the generated wave *determines the direction of time*. This presents a new kind of dissipation, namely “dissipation in the frequency space”, which invalidates time-reversal symmetry.

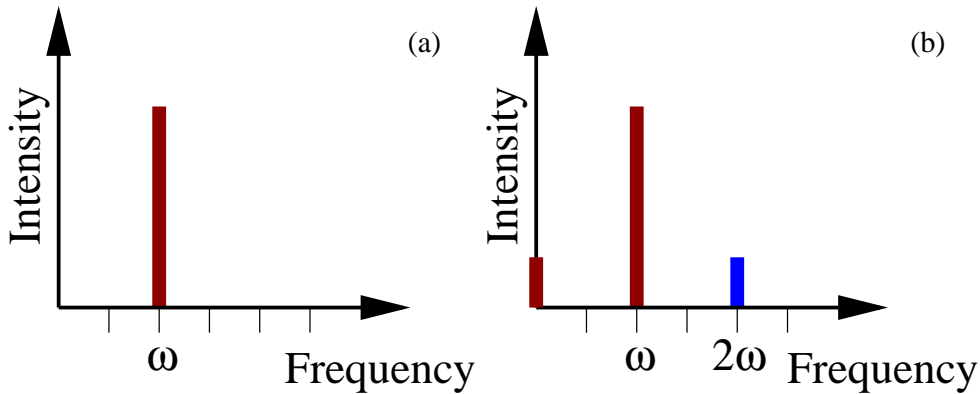


Figure 20: Light intensity distribution on the input (a) and on the output (b) of the SHG.

²⁰Both ω and 2ω beams can be attenuated during their propagation, but this is merely dissipation in the linear propagation of the wave through a medium. In our analysis, we neglect this kind of dissipation. Under this condition, linear optics is reversible. This can be seen for example in the Faraday effect, which (in the absence of dissipation) consists only of the rotation of the polarization plane (no induced ellipticity). After applying the time-reversal operation, the polarization of the light at the output (of the reversed process) is the same as the polarization at the input of the original process, thus time-reversal symmetry is preserved. This is true if one follows our convention and applies the time reversal *both* to the sample and to the measurement process.

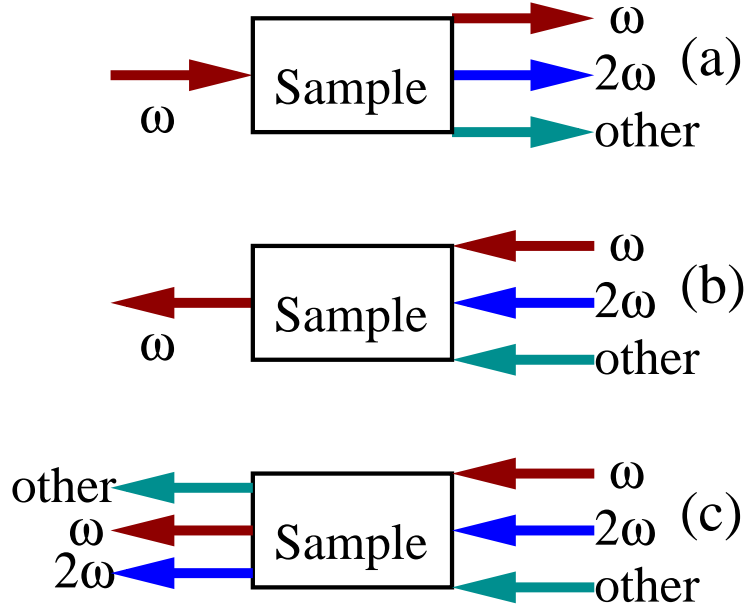


Figure 21: Time-reversal asymmetry in SHG. Panel (a) presents the original process, panel (b) a process in reversed time which would restore the symmetry, panel (c) presents a physically valid process described in reversed time.

As stated before, there is no dissipation in the process of SHG in the usual meaning, i.e. the amount of energy in the radiative form is constant. However, there is a transfer of energy between the frequencies, in particular energy flows from the frequency ω to other frequencies (see Fig. 20). We call this *dissipation in frequency space*, in contrast to the more usual *dissipation in real time*. Dissipation in frequency space can mix real and imaginary parts of the nonlinear susceptibility tensor. The distinction between these two types of dissipation is often encountered in the literature. We consider them here on an equal footing stating that the presence of any of them (in our case it is the dissipation in frequency space) causes the system to have dynamical [63] and thus irreversible properties. In this case, time-reversal does not apply to the symmetry analysis [36, 40, 41].

This fact becomes even more obvious if one takes the global picture of SHG. Radiation acting on an *ensemble of atoms* may excite and deexcite them in many ways *simultaneously*. Thus contributions of many frequencies are always present (see Fig. 21(a)). One has a unique source of ω light but several detectors for beams of different frequencies: 2ω , 3ω , etc, resulting from sum frequency generation (in particular SHG); linearly propagating ω light; and a DC current resulting from difference frequency generation. This is due to the expansion of the source term (polarization \mathbb{P}) in terms of the electric field:

$$\mathbb{P} = \mathbf{P}_1 + \mathbf{P}_2 + \dots = \chi^{(1)}(\omega)\mathbf{E}^{(\omega)} + \chi^{(2)}(\omega):\mathbf{E}^{(\omega)}\mathbf{E}^{(\omega)} + \dots \quad (2.15)$$

Imposing time reversal, the detectors become sources and vice versa. Thus, in the time reversed process, one ends up with a single detector, the one which receives the light of frequency ω (Fig. 21(b)). In order to obtain this single frequency one has to redirect all these (previously generated) beams back to the sample, conserving their phase. The source

term now becomes:

$$\mathbb{P} = \chi^{(1)}(\omega)\mathbf{E}^{(\omega)} + \chi^{(1)}(2\omega)\mathbf{E}^{(2\omega)} + \dots + \chi^{(2)}(\omega): \mathbf{E}^{(\omega)}\mathbf{E}^{(\omega)} + \chi^{(2)}(2\omega): \mathbf{E}^{(2\omega)}\mathbf{E}^{(2\omega)} + \dots \quad (2.16)$$

Since the phases of the now incident electric fields are the same as for the previously outgoing electric fields, all the terms but those with $\chi^{(1)}$ cancel (which means that in the outgoing light one now has only the contribution at the frequency ω) and the original situation at the input of the process is restored. This description, though mathematically correct, is physically invalid, since there is no practical way to detect an infinite array of frequencies along with the beam phases and to revert it with arbitrary accuracy (Fig. 21(c)). Tracing out the “bath” degrees of freedom (frequencies other than ω and 2ω) causes a transition from a pure to a mixed state of the system, which means that some memory is lost. This happens because the traced subsystem and the bath are not statistically independent [64]. Thus, in any practical situation, there is no possibility to generate only the frequency ω out of a whole array of frequencies. The process of SHG looks different in time t than in the reversed time $-t$. Such a process is called *dynamical*.

2.4.3 Spatial Operations

So far we have reasoned that the time-reversal operation has to be excluded from the symmetry analysis of SHG. However, *magnetism* may bring an additional complication, since the magnetic spin structure is an additional aspect the symmetry analysis must account for, and it is the time-reversal which is conveniently applied to flip the local magnetic moments. This is, however, not correct: it is the classical covering symmetry [65] of the magnetic crystal which should be addressed in a symmetry analysis rather than the quantum-mechanical symmetry of the wavefunctions²¹. This means that the operation applied to reverse the localized magnetic moments should be performed in real space rather than Hilbert spin space. Consequently, time-reversal cannot be used for the symmetry classification of magnetic moments.

Taking into account that time-reversal is not suitable for the description of dynamical phenomena, one needs an operation which merely flips the localized magnetic moments without inverting the time-flow. This can be accomplished by purely spatial point-group operations. In many *antiferromagnetic* (e.g. transition-metal-oxide) crystals a simple translation by a lattice vector reverses the magnetic moments. In many ferromagnetic and anti-ferromagnetic systems this may be accomplished by a mirror operation. The spatial operation, which reverses the localized magnetic moments, is called by us “moment-reversal”. This operation is obviously unitary, in contrast to the time-reversal operation, which is anti-unitary. Consequently, one does not need to invoke the time-reversal operation to describe the full symmetry of magnetic crystals.

²¹According to [65], both the σ_x and σ_y operations cause reversal of the spin part of the quantum-mechanical fermionic wavefunction. Of them, σ_y is conveniently used to describe time-reversal, since it is an anti-unitary operation [66].

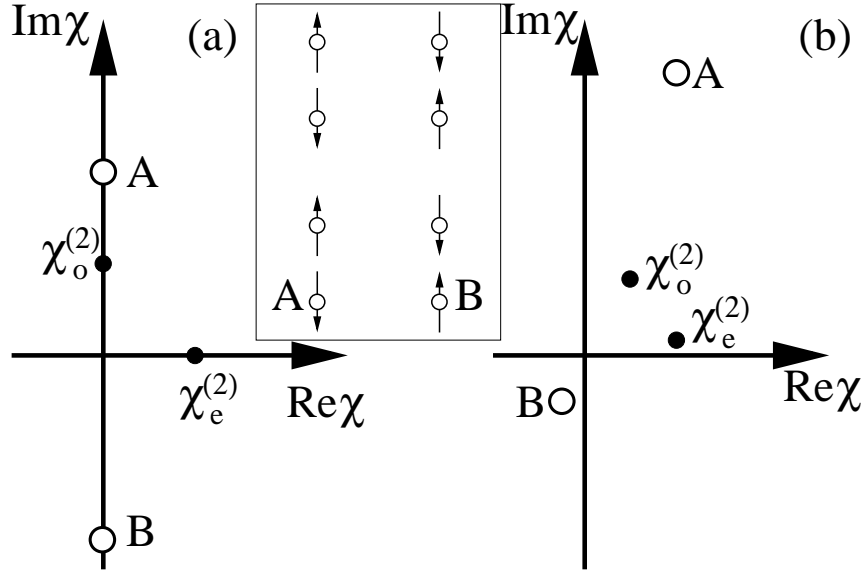


Figure 22: Nonlinear susceptibility tensor elements and resulting SHG intensity using time-reversal (panel (a)) and spin-reversal (panel (b)). Position of the points “A” and “B” is given by $(\chi_e^{(2)})^2 + (\chi_o^{(2)})^2 \pm 2\chi_e^{(2)} \cdot \chi_o^{(2)}$, and the distance of the points “A” and “B” from the origin of the complex plane corresponds to the intensity of SHG from the domains A and B, respectively (see inset for an example of domains in Cr_2O_3). For simplicity, the moduli of the tensor elements have been taken as equal to 1, but the argumentation also holds in the general case.

2.4.4 Practical Implications

Next, we support our reasoning by an example where the application of time-reversal and “moment-reversal” in the symmetry analysis yields different results (see Fig. 22). Let us assume a spin structure with two domains, A and B, related to each other by spin-reversal²². A symmetry analysis, similar to the one in [67], provides us with the set of nonvanishing elements of the nonlinear susceptibility tensor (i.e. $\chi^{(2)}$ tensor) along with the parities of these elements. Let us assume that for a certain experimental geometry only two tensor elements, called $\chi_o^{(2)}$ and $\chi_e^{(2)}$, contribute to the resulting SHG light, and that $\chi_o^{(2)}$ is odd while $\chi_e^{(2)}$ is even in the domain operation. The intensity of SHG light at a fixed polarization is given by:

$$I_p \sim |(\chi_e^{(2)})^2 + (\chi_o^{(2)})^2 \pm 2\chi_e^{(2)} \cdot \chi_o^{(2)}| \quad (2.17)$$

where “+” stands for domain A, “-” for domain B. In the conventional approach, where *time-reversal* is the operation mapping domains into each other and dissipation is absent, $\chi_o^{(2)}$ must be purely imaginary and $\chi_e^{(2)}$ purely real (Fig. 22(a)), since then dissipation is necessarily absent. In this traditional approach, the first two components of the sum in eq. (2.17) are real, while the last one is imaginary. Because it is the modulus of the whole sum that determines the output intensity, the domain contrast is lost since

$$|a+ib| = |a-ib|, \quad (2.18)$$

²²This is possible e.g. in antiferromagnets like Cr_2O_3 or those with inequivalent magnetic sites.

which is in odds with experiment [5]. This is not the case if one uses the correct operation of “moment-reversal” for the symmetry classification, since then both tensor elements $\chi_o^{(2)}$ and $\chi_e^{(2)}$ are just complex numbers without any constraints on their relative phase, see Fig. 22b, and domain imaging is possible, as described in [67]. Consequently, the symmetry analysis yields very different predictions if one uses time- or spin-reversal. For the frequencies far from resonances, however, the complex phase difference between $\chi_o^{(2)}$ and $\chi_e^{(2)}$ approaches 90° , and the domain contrast is lost also in the “moment-reversal” description (in agreement with experiment [5]).

Finally we would like to remark on the validity of previous work on the group-theoretical classification of (magneto-)optical tensors. According to Pan *et. al.* [12], the time-reversal operation forces the tensor elements to decouple into mutually exclusive sets of purely real and imaginary ones (if all the kinds of dissipation are neglected). In addition, the crystal symmetry forces the tensor elements to decouple into mutually exclusive sets of elements odd and even in *magnetization*-reversal, these two divisions are equivalent in the absence of conventional dissipation, i.e. real (imaginary) elements are even (odd) in the magnetization. These are the results of a purely quantum-mechanical approach, where the Hamiltonian is Hermitean (non-dissipative). In a real experiment, the laser spot size is much bigger than the Wigner-Seitz cell, thus the experimental response is of macroscopic character. In order to describe this macroscopic response one should not apply uniquely microscopic conclusions to the analysis of these tensor elements. Consequently, taking into account the dissipation in frequency space (i.e. redistribution of the response frequencies) and thus the nature of SHG as a dynamical process (which rules out the applicability of the time-reversal operation) will prevent the classification of tensor elements as real or imaginary ones, although for systems with higher symmetry the classification of tensor elements as odd and even ones in the magnetization (or in the antiferromagnetic order parameter \mathbf{L}) can still apply. The nonlinear susceptibility tensor $\chi^{(2\omega)}$ was usually approximated to be real far from resonances. This was justified for the crystals previously mostly used for SHG, and even more extensively as textbook examples [68, 69], which were usually wide-bandgap insulators. This approximation is not valid in the systems described by us: metals and transition metal oxides, where at any frequency one is close enough to one of the resonances (this will be shown in Sec. 3.3). Thus, the only choice for an operation which accounts for the spin structure is “moment reversal”, realized as a spatial operation.

Summary of symmetry analysis:

In our symmetry analysis, we took into account all the spin configuration of low index surfaces of fcc antiferromagnets. As the result, we determined

- the nonvanishing elements of the nonlinear optical susceptibility tensor
- the behavior of those tensor elements in domain operations (domain-parity)

Knowing these results we can state that

- SHG is able to detect the surface antiferromagnetism
- distinguish it from any other magnetic phase
- the particular spin structure at the surface can be detected by SHG in many cases
- domain imaging of antiferromagnetic surfaces can be performed experimentally

These interesting results of our symmetry analysis do not complete our work on SHG from antiferromagnets. So far we cannot say anything about the magnitude nor complex phase of the nonvanishing tensor elements. Their frequency dependence (spectrum) remains uncovered as well. In order to solve these problems, we need an electronic calculation. For the purposes of achieving our ultimate goal, which is the description of the dynamics of SHG, we also need an electronic many-body theory. This theory will be presented in the next chapter of this thesis.

Chapter 3

Electronic Theory

In the previous chapter, we described the important results brought by symmetry analysis. We have also stated its deficiencies, namely the lack of quantitative conclusions. These deficiencies can be overcome by performing an electronic calculation *based upon the results of our symmetry analysis*. This electronic calculation, described in the current chapter of this work, is the next step of developing our theory of SHG from antiferromagnetic surfaces.

We set up the theory and perform our calculation having a particular material, NiO, in mind. However, taking into account the electronic configurations $3d^8$, $3d^7$, and $3d^6$ opens the way to describe properly not only the highly excited states of NiO, but also other materials. With only slight modification of this work, nearly all elements²³ of the periodic table can be addressed, which overcomes earlier limitations of that theory. Especially, the extension to other cubic metal oxides is straightforward.

Our ligand-field-theory approach allows us to fully consider the *surface* of the material. We are not restricted to a monolayer of NiO.

The results of our calculations concern the SHG response of the sample in the equilibrium state. We present the spectra of the nonlinear magneto-optical susceptibility tensor which governs this response. Furthermore, we develop a theory and perform a simulation of a pump-and-probe experiment. During such an experiment, the dynamical behavior of electrical charges and magnetic moments of antiferromagnetic NiO can be investigated on the time scale of femtoseconds.

3.1 Interplay of Symmetry and Electronic Theory

One of the important results of our symmetry analysis (Chapter 2) is the determination of the nonvanishing elements of the nonlinear optical susceptibility tensor for a given surface spin configuration. The existence or vanishing of certain tensor elements has, besides the classical covering symmetry, also microscopical reasons. Here, we will discuss the interplay between these symmetry-related and microscopic origins of the nonlinear magneto-optical

²³Systems which escape the analysis within this framework are atoms with the electronic configuration d^5 (Cr, Mn, Mo, Re), and those where valence band includes f electrons (actinides).

susceptibility tensor. The argumentation presented here applies to the (001) surface, but the extensions to other low-index surfaces can be performed without difficulties.

In general, the tensor element $\chi_{ijk}^{(2)}(2\mathbf{q}, 2\omega)$ can be expressed as follows [13, 70]:

$$\chi_{ijk}^{(2)}(2\mathbf{q}, 2\omega) = \frac{e^3}{2q^3V} \sum_{\mathbf{k}, l, l', l''} \left[\langle \mathbf{k} + 2\mathbf{q}, l'' | i | \mathbf{k} l \rangle \langle \mathbf{k} l | j | \mathbf{k} + \mathbf{q}, l' \rangle \langle \mathbf{k} + \mathbf{q}, l' | k | \mathbf{k} + 2\mathbf{q}, l'' \rangle \times \right. \\ \left. \times \frac{\frac{f(E_{\mathbf{k}+2\mathbf{q}, l''}) - f(E_{\mathbf{k}+\mathbf{q}, l'})}{E_{\mathbf{k}+2\mathbf{q}, l''} - E_{\mathbf{k}+\mathbf{q}, l'} - \hbar\omega + i\hbar\alpha} - \frac{f(E_{\mathbf{k}+\mathbf{q}, l'}) - f(E_{\mathbf{k}l})}{E_{\mathbf{k}+\mathbf{q}, l'} - E_{\mathbf{k}l} - \hbar\omega + i\hbar\alpha}}{E_{\mathbf{k}+2\mathbf{q}, l''} - E_{\mathbf{k}l} - 2\hbar\omega + 2i\hbar\alpha}} \right], \quad (3.1)$$

where V is the volume of the unit cell (because we treat the surface, we integrate over one half of the unit cell) and f is the Fermi distribution. The screening factor has been neglected. The summation is executed over wavevectors \mathbf{k} corresponding to the states l , and also over two lattice sites, with the atomic magnetic moment set antiparallely in the AF phase (staggered summation). This allows us to account for the antiferromagnetism. The damping factor α gives us the causal part of the Green's function and corresponds to the breaking of time-reversibility of the Hamiltonian. Matrix elements $\langle \mathbf{k}, l | i, j, \text{ or } k | \mathbf{k}, l \rangle$ describe transitions between the electronic d and s states of nickel, consequently they are forbidden in the spherically symmetric environment. Breakdown of the inversion symmetry at the surface changes the selection rules, so that transitions with $\Delta l = \pm 2, \pm 1$ and 0 are allowed. We restrict ourselves to intra-atomic transitions, since they suffice to explain the spectral structures within the gap of NiO [71, 72].

Spin-orbit coupling, being mainly effective in the magnetically-ordered phases, slightly lifts the orthogonality of the wavefunctions (in addition to a similar effect produced by the surface symmetry breaking). As the result, the dipoles x , y , and z are no longer orthogonal. This allows for the non-vanishing triple product of these dipoles in eq. (3.1).

The transition matrix elements are quite cumbersome to calculate, thus in our calculations we will only use some estimates of their value according to [73]. Additionally, some of the products of the transition matrix elements can cancel depending on the symmetry of the investigated surface. In the following subsections, we will qualitatively discuss the nonvanishing tensor elements as resulting from these products for each of the magnetic phases of the surface.

3.1.1 The Paramagnetic Phase

In this magnetic phase, mainly the surface symmetry breaking plays a role in determining the transition matrix elements. The directions x and y (in-plane) are equivalent, so we do not expect any tensor elements which result from a combination of dipoles x and y . From this and because the z direction is distinguished (surface normal),

- tensor elements χ_{zxx} and χ_{zyy} should be equal, but different from χ_{zzz} , and
- in order to suppress any information about magnetization, indices x and y should be present an even number of times each.

These conditions allow for the following tensor elements: $\chi_{zxx} = \chi_{zyy}$, χ_{zzz} , and $\chi_{yyz} = \chi_{xxz}$. This is in agreement with the results of our symmetry analysis.

In the paramagnetic phase, the magnetic moments localized on nickel atoms are disordered and thus do not influence the result. Therefore, for the tensor elements which do not vanish in the paramagnetic phase, their value calculated according to eq. (3.1) is equal to a value resulting from only one nickel atom multiplied by two.

As it can be seen from the above argumentation, the paramagnetic tensor elements do not exhibit any dependence on spin-orbit coupling (to first order).

3.1.2 The Ferromagnetic Phase

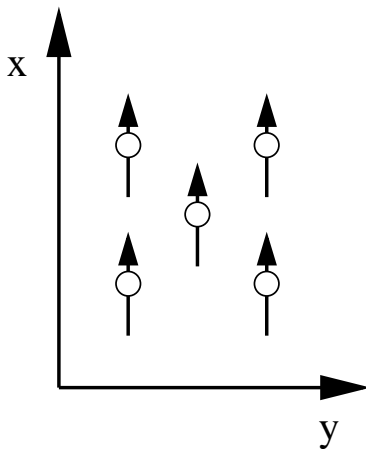


Figure 23: The ferromagnetic surface spin configuration used to perform the analysis in the current subsection.

The specific spin configuration we have in mind performing the analysis described here is shown in Fig. 23. Because the magnetic moments are parallel to the x axis, we do not expect any tensor elements containing x an odd number of times. This leaves us with the set of tensor elements described previously as paramagnetic, additionally some other tensor elements are present, we will refer to them as ferromagnetic. These ferromagnetic tensor elements contain y an odd number of times, from which we can deduce their *linear* dependence on spin-orbit coupling. Pairs of tensor elements which were equal in the paramagnetic phase, like $\chi_{zxx} = \chi_{zyy}$, are not equal now because of the ferromagnetic contribution to them. The preferential axis is namely parallel to x , which is thus inequivalent to y . Our numerical calculation is unable to determine this contribution, since it is of higher than first order in spin-orbit coupling.

The set of tensor elements deduced from the above considerations is the same as the set obtained by our symmetry analysis in the Chapter 2, for the configuration “ferro1” of the (001) surface.

3.1.3 The Antiferromagnetic Phase

Unlike in the previous subsection, there is no net magnetization in the antiferromagnetic phase. Thus, the “distinguished direction” is not defined by magnetic moments but rather by the ligands, and these are in the directions (110) and $(\bar{1}10)$. Still, the axes x and y exist, defined by the magnetic moments. These axes are inequivalent, since the localized

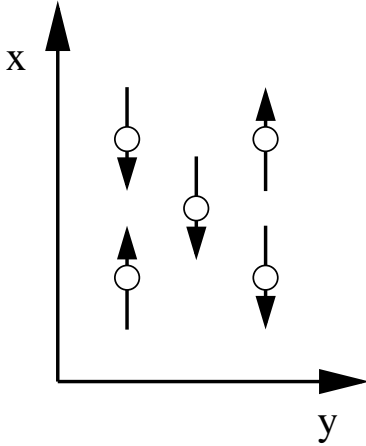


Figure 24: The antiferromagnetic surface spin configuration used to perform the analysis in the current subsection.

magnetic moments are parallel only to x . In addition, localized magnetic moments alternate along the (110) line and are kept invariant along the $(\bar{1}10)$ direction. As the spin-orbit coupling lifts the orthogonality of x and y dipoles slightly, tensor elements with the combination of indices x and y become allowed. On the other hand, the ferromagnetic tensor elements must disappear, since the contributions from opposing spins cancel each other in the antiferromagnetic phase. This leaves us with the set of tensor elements identical to the one determined by our symmetry analysis in the Chapter 2, for the AF configuration c) of the (001) surface.

As the spin-orbit coupling is intervening only once, the antiferromagnetic tensor elements are linear in the order parameter.

The above remarks about the microscopic origin of tensor elements in the AF phase suggest that the SHG is of the same order of magnitude as from a ferromagnetic surface. This means that the effect is measurable. Also, because no intersite spin-flip transitions are involved, the dynamical SHG is expected to be at least as fast as for ferromagnets.

In order to obtain quantitative conclusions about the non-vanishing tensor elements, an electronic calculation is needed. In the next sections, we present such a calculation.

3.2 The Hamiltonian

The proper description of effects encountered in transition metals and their oxides require an extensive use of correlation effects. This is evident even in some effects of the ground state [74], and becomes especially important in nonlinear optics where highly excited states are frequently involved. Therefore, we employ an exact-diagonalization method which allows for a non-perturbative treatment of electronic correlation. Under these conditions, the most general Hamiltonian has the following form:

$$H = H_{band} + H_C + H_{SO} \quad (3.2)$$

where H_{band} describes the band structure of the investigated system, H_C describes the on-site interaction, and H_{SO} is the relativistic part, which describes the spin-orbit coupling needed for magneto-optics. In this work, we focus on the on-site interaction part of the Hamiltonian, which has the following form:

$$H_C = \sum_{i,j,k,l,\sigma,\sigma',\sigma'',\sigma'''} U_{i\sigma,j\sigma',l\sigma'',k\sigma'''} c_{i\sigma}^\dagger c_{j\sigma'}^\dagger c_{k\sigma''} c_{l\sigma'''} \quad (3.3)$$

Here, $U_{i\sigma,j\sigma',l\sigma'',k\sigma'''}$ is the on-site Coulomb interaction which can be described in full generality by the three parameters: Coulomb repulsion U , exchange interaction J , and the

exchange anisotropy ΔJ . In this section, we will concentrate on this on-site Hamiltonian, which possesses the full spherical symmetry of a free nickel ion. The assumption is that exactly two electrons are transferred to the oxygen atom, so that the electronic configuration of the nickel ion is $3d^8 4s^0$, $3d^7 4s^1$, or $3d^6 4s^2$. The energy difference between the configurations $3d^8 4s^0$ and $3d^7 4s^1$ constitute the gap of around 4.0 eV which makes NiO a charge transfer insulator. The states most interesting for us are the 8, 7, or 6 d-states²⁴, or equivalently, 2, 3 or 4 holes in the d-shell of the nickel ion²⁵.

In this work, we will describe the holes according to the convention presented in the following table:

name	band	l_z	spin
1	3d	-2	up
2	3d	-2	down
3	3d	-1	up
4	3d	-1	down
5	3d	0	up
6	3d	0	down
7	3d	1	up
8	3d	1	down
9	3d	2	up
10	3d	2	down
11	4s	0	up
12	4s	0	down

The antisymmetrized products of the single-particle states, which constitute a basis for our many-body states, are described with the use of square brackets, e.g. $[1,6]$ describes a two-particle state constructed of two 3_d hole states, one with $l_z = -2$, and the other with $l_z = 0$.

The states $[i,j,k,l]$, where $i\dots l$ are the single-particle states (either 3_d or 4_s), are referred to as simple product states in Fock space. The Hamiltonian H_C expressed in this basis is called by us simple-product Hamiltonian. On the other hand, Clebsch-Gordan algebra provides us with the way to obtain linear combinations of the simple-product states, these linear combinations are adapted to the spherical symmetry of the free ion and thus describe the coupled, many-body states. These many-body states form a symmetry-adapted basis for the H_C , which is then called symmetry-adapted Hamiltonian.

In the following subsections, we will describe how these holes couple to each other, forming the desired many-body states.

²⁴ $3d^8$, $3d^7$, or $3d^6$

²⁵We do not implement point-charge model (Madelung energy) since we are not interested in the determination of the total energy in the ground state.

3.2.1 Two Holes

In the limit of weak spin-orbit coupling, two holes form a two-particle state by an LS coupling. The resulting quantum numbers are expressed as

$$\begin{aligned} L_z &= l_{z,1} + l_{z,2} \\ S_z &= s_{z,1} + s_{z,2} \end{aligned} \tag{3.4}$$

Here, the $l_{z,i}$ and $s_{z,i}$ denote the z-components of orbital and spin momenta of the i-th hole, respectively. From Eq. (3.4) it becomes clear that the orbital momentum of the coupled state constructed from two d-holes can be 0, 1, 2, 3, or 4, which is conveniently described as S, P, D, F, and G states. The resulting spin can be equal to 0 or 1, in other words each of these S - G states can have a singlet or triplet degeneracy, which is denoted as 1S , 3S , 1P , etc.

It is necessary to take into account the fact the two holes we couple are indistinguishable. Thus, according to the Pauli principle, they have to differ by at least one quantum number. As a single d-hole can be in one of 10 states, two d-holes can produce 45 different two-particle states. Taking into account the multiplicity of the above mentioned two-particle states, both from the point of view of their total orbital momentum and their total spin, we see that the only way to fill these 45 states with our symmetry-adapted two-particle states is (1S , 3P , 1D , 3F , 1G), where 1X means spin-singlet and 3X triplet with the corresponding orbital momentum. These symmetry-adapted states are produced from simple products with use of Clebsch-Gordan algebra, as presented in [75]. As the result, the symmetry-adapted two-particle states take the form depicted in the table A.1 in the Appendix A. The states there are named by capital letters after their angular momentum (L), their superscripts describe the spin-degeneracy (S), and subscripts refer to the magnetic quantum number (L_z). Similar nomenclature is maintained henceforth²⁶.

The symmetry-adapted Hamiltonian has already a diagonal form since it describes a static spherically-symmetric system. There are only five different values at the diagonal of this Hamiltonian, degenerate according to the degeneracy of two-hole symmetry-adapted wave functions which form the basis. We call these values E_S , E_P , E_D , E_F , and E_G , they can be expressed by the constants U, J, and ΔJ . We use the form of diagonal elements of the symmetry-adapted Hamiltonian as derived by Oleś and Stollhoff [76]²⁷. Knowing that all off-diagonal elements of the symmetry-adapted Hamiltonian (3.3) must vanish, we can express the simple-product Hamiltonian by U, J, and ΔJ . This will be used in the next subsection.

There remains an important task of determining the numerical values of the parameters U, J, and ΔJ , through which all the energies are expressed. This can be done by fitting them to measured spectroscopical lines of doubly ionized nickel in the gaseous phase. However, since only two two-hole levels are measured spectroscopically for gaseous Ni^{++} [77] (3F and

²⁶For three- and four-hole states, some of the states with *identical* angular momentum appear twice. We distinguish them by displaying an additional index in parenthesis.

²⁷Their Hamiltonian is less general than the one described here. In particular, it does not possess the claimed spherical symmetry.

3P)²⁸, it is not possible to determine our three parameters. On the other hand, there is another, equivalent system of parameters to describe the energy levels: Racah parameters A, B, and C [78]. Since several authors give their estimates for the values of the parameters B and C, we can express our energy levels as well as the simple-product Hamiltonian elements by Racah parameters. The values of B and C have been taken from [79], and the parameter A (equivalent to U) was adjusted to the experiment. Consequently, we obtain the following two-holes energy levels:

$$\begin{aligned}
 E(^3F) &= A - 8B = 0.0 \text{ eV} \\
 E(^3P) &= A + 7B = 2.070 \text{ eV} \\
 E(^1G) &= A + 4B + 2C = 3.008 \text{ eV} \\
 E(^1D) &= A - 3B + 2C = 2.042 \text{ eV} \\
 E(^1S) &= A + 14B + 7C = 7.768 \text{ eV}
 \end{aligned}
 \tag{3.5}$$

3.2.2 Three and Four Holes

In this subsection we describe the treatment of three- and four-hole states within the framework of our theory. This allows not only for the proper description of excited states in NiO, but also other materials such as CoO and FeO. The three- and four-hole states (all holes are on-site) form the basis for the Hamiltonian. Both the three-hole and four-hole parts of the Hamiltonian preserve the spherical symmetry of a free nickel ion.

The states for the ionic nickel electronic configuration $3d^74s$ are called three-hole states. Symmetry-adapted three-hole states are produced by coupling of symmetry-adapted two-hole states to a third d hole and performing the Clebsch-Gordan algebra followed by Gram-Schmidt orthogonalization²⁹. The result is presented in Tables A.2 and A.3.

There are 120 states conveniently grouped as 2P , 2D , 2D , 2F , 2G , 2H , 4P , and 4F states according to their degeneracy in the spherical environment. The other set of 120 states results from the opposite orientation of the fourth hole, namely that in the 4s band. Although coupling of three d-holes can produce a state with angular momentum equal to 6, the Pauli principle forbids using more than two holes with the maximal l_z quantum number. Therefore the highest angular momentum is 5 (state 2H), which results from using two holes with $l_z=2$ and one with $l_z=1$.

In that way we determine the basis for the three-hole symmetry-adapted Hamiltonian. Matrix elements of the three-hole simple-product Hamiltonian representation are calculated by the embedding of the matrix elements of the simple-product *two-hole* Hamiltonian. This allows us to construct the symmetry-adapted three-hole Hamiltonian using the Clebsch-Gordan algebra. As the result, the matrix elements of the symmetry-adapted Hamiltonian are expressed by Racah parameters A, B, and C and their numerical value can be calculated. This Hamiltonian is diagonal and its values are degenerate according to the multiplicity of the symmetry-adapted states.

²⁸Unlike for neutral Ni (starting point for calculations on metallic nickel) where energies of two-hole states were measured.

²⁹We have two *different* states of D character, they have to be orthogonal. Therefore we use *different* two-hole states to obtain these D states, and perform the orthogonalization on this (partial) result.

The symmetry-adapted four-hole states (i.e. states $3d^64s^2$) are obtained by a Clebsch-Gordan coupling of the two-hole states, followed by Gram-Schmidt orthogonalization. The result of this numerically performed procedure is a set of 210 states 1S , 1S , 1D , 1D , 1F , 1G , 1G , 1I , 3P , 3P , 3D , 3F , 3F , 3G , 3H , and 5D presented in Table A.4. The highest angular momentum possible to obtain by coupling four undistinguishable d-holes is 6, since one has to use two holes with $l_z=2$ and two with $l_z=1$. As previously, the matrix elements of the four-hole simple-product Hamiltonian are determined by use of an embedding procedure, they are then used to construct the four-hole symmetry-adapted Hamiltonian. Again, it is diagonal and its values are degenerate according to the multiplicity of the symmetry-adapted states. The resulting Hamiltonian fully describes the three- and four-hole interactions.

The procedure presented here was performed for a specific system, nickel ion. Nevertheless, it can be applied to any system where up to four d-holes or d-electrons are present (the parameter values must be altered), like cobalt, iron, scandium, titanium or vanadium. Furthermore, an extension towards the systems with 5 d-electrons is possible - one has to couple an additional hole to our four-hole states and orthogonalize the result. For the elements of such five-hole Hamiltonian, an embedding procedure similar to the one described by us can then be performed.

3.2.3 Bulk vs. Surface of NiO

So far, we have discussed the on-site interaction part of the Hamiltonian in the spherically symmetric environment. Because of this symmetry, the Hamiltonian is degenerate to a large extent. Nearly all these degeneracies are lifted when the symmetry is lowered. Since the non-linear magneto-optic effects are known to be sensitive to the splitting of electronic levels [80], we examine the crystal field induced level splitting in detail. Here, we will show how the lowering of the symmetry influences the two-hole part of our Hamiltonian. The extension of the analysis to three- and four-hole parts of the Hamiltonian is straightforward.

Spherical	O_h	C_{4v}
1S	1A_1	1A_1
3P	3T_1	$^3A_1+^3E$
1D	1E	$^1A_1+^1B_1$
	1T_2	$^1B_2+^1E$
3F	3A_2	3B_2
	3T_1	$^3A_1+^3E$
	3T_2	$^3B_1+^3E$
1G	1A_1	1A_1
	1E	$^1A_1+^1B_1$
	1T_1	$^1A_2+^1E$
	1T_2	$^1B_2+^1E$

Table 3.1: Splitting of the spherical symmetry-adapted states in the cubic (O_h) and square (C_{4v}) environments.

linear combinations of spherical functions, adapted to the cubic environment, are called *cubic harmonics*. Using them, we describe the states in the cubic and square (surface) environment. The presence of the surface with its square symmetry splits the states further, one obtains the following set of two-hole surface states: 3E , 3A_2 , 3B_2 , 3E , and 3B_1 . Splitting of all the two-hole states in consequent symmetry breaking is presented in the

environment into states with symmetry 3A_2 , 3T_1 , and 3T_2 . These states are constructed by linear combinations of the previously defined symmetry-adapted orbitals. Such

First, we will describe the level splitting in the cubic environment. The levels obtained in this way will be split in the next step which involves lowering the symmetry from cubic to square one due to the surface.

For example, the 3F state gets split in the cubic environment into states with symmetry 3A_2 , 3T_1 , and 3T_2 . These states are constructed by linear combinations of the previously defined symmetry-adapted orbitals. Such

Table 3.1.

Level splitting due to lowering of the symmetry is governed by the rules of group theory. In particular, it tells us that, for a cubic symmetry O_h , only representations of the order up to three are possible. The highest order of representations which describe the surface states (where the surface square lattice has symmetry C_{4v}) is two. These conditions mark the maximal orbital degeneracies. The particular assignment of the cubic harmonics to the states in the cubic and square environments can be performed by careful analysis of the symmetry properties of the harmonics and the representations.

The square symmetry-adapted wavefunctions for each of the surface two-hole states are presented in Table 3.2.

Table 3.2: Two-hole wavefunctions adapted to surface symmetry. The two 4s holes have been skipped in the notation. For the triplets, only the $\uparrow\uparrow$ state is shown, but the remaining ones can be obtained easily.

Spherical state	Surface state	Wavefunction
1S	1A_1	$\sqrt{\frac{1}{5}} \times ([1, 10] - [3, 8] + [5, 6] + [4, 7] - [2, 9])$
3P	A_1	$\sqrt{\frac{4}{5}}[1, 9] - \sqrt{\frac{1}{5}}[3, 7]$
	E_α	$\sqrt{\frac{2}{5}}[1, 7] - \sqrt{\frac{3}{5}}[3, 5]$
	E_β	$-\sqrt{\frac{2}{5}}[3, 9] + \sqrt{\frac{3}{5}}[5, 7]$
1D	A_1	$\sqrt{\frac{2}{7}}[1, 10] + \sqrt{\frac{1}{14}}[3, 8] - \sqrt{\frac{2}{7}}[5, 6] +$ $-\sqrt{\frac{1}{14}}[4, 7] - \sqrt{\frac{2}{7}}[2, 9]$
	B_1	$-\sqrt{\frac{1}{7}}[6, 9] - \sqrt{\frac{3}{14}}[7, 8] + \sqrt{\frac{1}{7}}[5, 10] + \sqrt{\frac{1}{7}}[1, 6] +$ $-\sqrt{\frac{3}{14}}[3, 4] - \sqrt{\frac{1}{7}}[2, 5]$
	B_2	$-\sqrt{\frac{1}{7}}[6, 9] - \sqrt{\frac{3}{14}}[7, 8] + \sqrt{\frac{1}{7}}[5, 10] - \sqrt{\frac{1}{7}}[1, 6] +$ $+\sqrt{\frac{3}{14}}[3, 4] + \sqrt{\frac{1}{7}}[2, 5]$
	E_α	$\sqrt{\frac{3}{7}}[1, 8] - \sqrt{\frac{1}{14}}[3, 6] + \sqrt{\frac{1}{14}}[4, 5] - \sqrt{\frac{3}{7}}[2, 7]$
	E_β	$\sqrt{\frac{3}{7}}[4, 9] - \sqrt{\frac{1}{14}}[6, 7] + \sqrt{\frac{1}{14}}[5, 8] - \sqrt{\frac{3}{7}}[3, 10]$

continued on the next page

<i>continued from the previous page</i>		
3F	B_1	$\sqrt{\frac{1}{2}}([1, 5] - [5, 9])$
	E_α	$\sqrt{\frac{1}{8}}(\sqrt{3}[7, 9] + \sqrt{3}[1, 7] + \sqrt{2}[3, 5])$
	E_β	$-\sqrt{\frac{1}{8}}(\sqrt{3}[1, 3] + \sqrt{3}[3, 9] + \sqrt{2}[5, 7])$
	B_2	$-\sqrt{\frac{1}{2}}([1, 5] + [5, 9])$
	A_2	$\sqrt{\frac{1}{5}}[1, 9] + \sqrt{\frac{4}{5}}[3, 7]$
	E_γ	$-\sqrt{\frac{1}{8}}(\sqrt{5}[1, 3] - \sqrt{\frac{9}{5}}[3, 9] - \sqrt{\frac{6}{5}}[5, 7])$
	E_δ	$-\sqrt{\frac{1}{8}}(-\sqrt{5}[7, 9] + \sqrt{\frac{9}{5}}[1, 7] + \sqrt{\frac{6}{5}}[3, 5])$
1G	$A_{1\alpha}$	$\sqrt{\frac{7}{12}}(\sqrt{\frac{1}{70}}[1, 10] + \sqrt{\frac{8}{35}}[3, 8] + \sqrt{\frac{18}{35}}[5, 6] - \sqrt{\frac{8}{35}}[4, 7] +$ $-\sqrt{\frac{1}{70}}[2, 9]) + \sqrt{\frac{5}{24}}[9, 10] + \sqrt{\frac{5}{24}}[1, 2]$
	$A_{1\beta}$	$-\sqrt{\frac{5}{12}}(\sqrt{\frac{1}{70}}[1, 10] + \sqrt{\frac{8}{35}}[3, 8] + \sqrt{\frac{18}{35}}[5, 6] - \sqrt{\frac{8}{35}}[4, 7] +$ $-\sqrt{\frac{1}{70}}[2, 9]) + \sqrt{\frac{7}{24}}[9, 10] + \sqrt{\frac{7}{24}}[1, 2]$
	B_1	$-\sqrt{\frac{3}{28}}[6, 9] + \sqrt{\frac{2}{7}}[7, 8] + \sqrt{\frac{3}{28}}[5, 10] + \sqrt{\frac{3}{28}}[1, 6] +$ $+\sqrt{\frac{2}{7}}[3, 4] - \sqrt{\frac{3}{28}}[2, 5]$
	A_2	$\sqrt{\frac{1}{2}}[9, 10] - \sqrt{\frac{1}{2}}[1, 2]$
	E_α	$\sqrt{\frac{1}{8}}(\sqrt{\frac{1}{2}}[7, 10] - \sqrt{\frac{1}{2}}[8, 9] + \sqrt{\frac{1}{2}}[1, 8] + \sqrt{3}[3, 6] +$ $-\sqrt{3}[4, 5] - \sqrt{\frac{1}{2}}[2, 7])$
	E_β	$\sqrt{\frac{1}{8}}(\sqrt{\frac{1}{2}}[2, 3] - \sqrt{\frac{1}{2}}[1, 4] + \sqrt{\frac{1}{2}}[4, 9] + \sqrt{3}[6, 7] +$ $-\sqrt{3}[5, 8] - \sqrt{\frac{1}{2}}[3, 10])$
	B_2	$\sqrt{\frac{1}{2}}(-\sqrt{\frac{3}{14}}[6, 9] + \sqrt{\frac{4}{7}}[7, 8] - \sqrt{\frac{3}{14}}[5, 10] - \sqrt{\frac{3}{14}}[1, 6] +$ $-\sqrt{\frac{4}{7}}[3, 4] + \sqrt{\frac{3}{14}}[2, 5])$
	E_γ	$\sqrt{\frac{1}{8}}(-\sqrt{\frac{1}{14}}[4, 9] - \sqrt{\frac{3}{7}}[8, 9] + \sqrt{\frac{3}{7}}[5, 8] + \sqrt{\frac{1}{14}}[3, 10] +$ $+\sqrt{\frac{7}{2}}[2, 3] - \sqrt{\frac{7}{2}}[1, 4])$
E_δ	$\sqrt{\frac{1}{8}}(\sqrt{\frac{7}{2}}[7, 10] - \sqrt{\frac{7}{2}}[8, 9] - \sqrt{\frac{1}{14}}[1, 8] - \sqrt{\frac{3}{7}}[3, 6] +$ $+\sqrt{\frac{3}{7}}[4, 5] + \sqrt{\frac{1}{14}}[2, 7])$	

Having determined the surface states, we need to obtain the corresponding energy levels. For the levels resulting from the split 3F state, these energies are known from the experiment [81] and presented in Table 3.3. In order to obtain the energies for the other levels we use a ligand field approach.

First, we have to express all the surface states in terms of the square surface ligand

parameters ε_0 , D_q , D_S , and D_U ³⁰. This is done in a manner similar to the one described in [78] for the cubic symmetry, but we have to account for the different (lower) symmetry of the ligand field. The result is presented in Table A.5. An interesting remark is that setting the surface-characteristic parameters D_U and D_S as equal to zero increases the degeneracy of the states. The degeneracy is then characteristic to the cubic environment, as presented in the second column of the Table 3.1. Setting also the cubic ligand parameters ε_0 and D_q to zero leads the levels back to the spherical symmetry.

In principle, knowing the position of the ligands for our particular material, and approximating the ligands by either point charges or dipoles, we can calculate these parameters. Instead, we use the experimental knowledge and fit these parameters so that the energies of the states resulting from splitting of the 3F state are expressed correctly. We obtain the following values for the parameters:

$$\begin{aligned}\varepsilon_0 &= 0.6699 \text{ eV} \\ D_q &= -0.1633 \text{ eV} \\ D_S &= 1.6542 \text{ eV} \\ D_U &= 0.2633 \text{ eV}\end{aligned}\tag{3.6}$$

The parameters obtained in this way allow for determination of the energy shifts caused by the symmetry breaking. The level energies obtained in this way are presented in Table A.5. They find a confirmation in experiments [82]. Along with the energies determined in the previous subsection for the spherically symmetric states, this gives us the full knowledge about the eigenfunctions and eigenvalues of energy at the surface of NiO.

Clearly, the ligand field parameters are smaller than the electron correlation parameter U (about 13.0 eV). Since the energy levels for two- and three-hole states are separated by U (in the spherically symmetrical environment), we do not expect any overlap of these states also in the lower symmetries.

In the next two sections we will use these functions and energies to calculate the nonlinear optical spectra of NiO and to draw some conclusions about spin- and charge dynamics in this material.

3B_1	0.0 eV
3E	0.65 eV
3B_2	1.0 eV
3A_2	1.3 eV
3E	1.44 eV

Table 3.3: Experimental values of energy levels for the surface-symmetry split 3F state [81].

3.3 The Nonlinear Spectrum of NiO (001)

According to eq. (3.1), there are three components needed for our calculations of the nonlinear susceptibility tensor elements: wavefunctions of our many-body eigenstates, transition matrix elements between these states, and the energy levels of these states. The wavefunctions and the corresponding energies were derived in the previous sections. However,

³⁰Among these parameters, ε_0 describes the energy shift in the crystal field, D_q is the level splitting in the cubic environment, D_S and D_U correspond to the level splitting in the octahedral and C_{4v} symmetries, respectively.

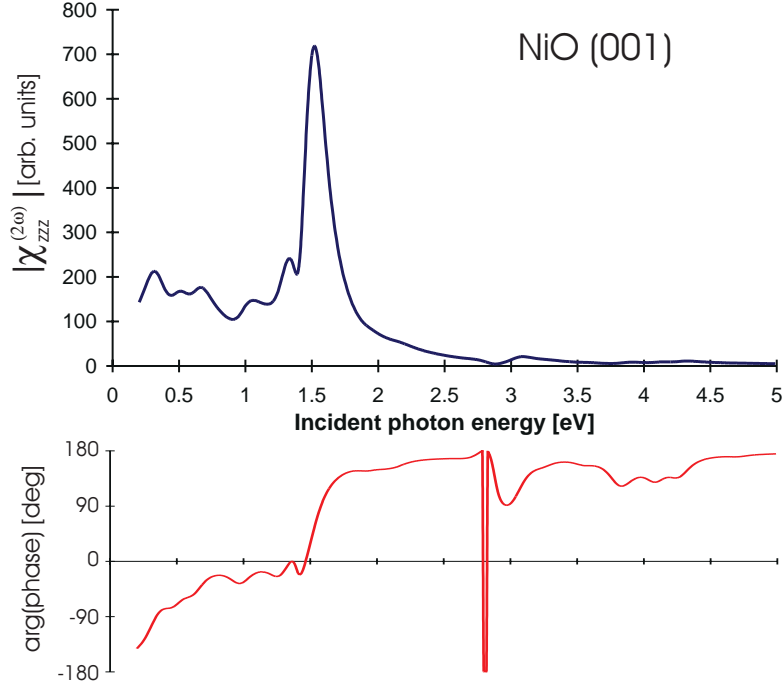


Figure 25: Spectrum of the paramagnetic tensor element χ_{zzz} . Both magnitude and the argument of the complex phase of the tensor element are presented separately.

the exact calculation of the transition matrix elements is very unreliable (transition metal oxides constitute the most difficult case due to their strong electronic correlations) and will not be performed within the framework of the current theory. Instead, we will use the approximations for the transition matrix elements obtained by Hübner *et al.* [73], which constitute the selection rules. Here, we present the spectra of two tensor elements: the prototypic paramagnetic tensor element χ_{zzz} in Fig. 25 and the prototypic antiferromagnetic tensor element χ_{zxy} in Fig. 26.

In the spectrum of χ_{zzz} , all the features fall within the gap, which we assume at 4.0 eV. The dominant structure in the spectrum corresponds to the transitions from the ground state to the states resulting from the split 3P state, which are all located near 3.0 eV. The position of the peak, around 1.5 eV corresponds to the fact that the tensor describes a two-photon process. Other, smaller peaks related to transitions between various states are also present. Another important feature of the calculated spectrum is that the tensor element is complex and its phase varies. This has important consequences for the absence of time-reversal symmetry in the process of SHG, as already extensively discussed in Sec. 2.4.

The spectrum of the antiferromagnetic tensor element χ_{zxy} reveals similar main traits as the previously discussed spectrum. However, we can observe an additional peak at 0.6 eV, with intensity much higher than the corresponding feature in the spectrum of the paramagnetic tensor element χ_{zzz} . Consequently, this is the “antiferromagnetic” spectral line which we suppose is especially suitable for nonlinear magneto-optics. Another inter-

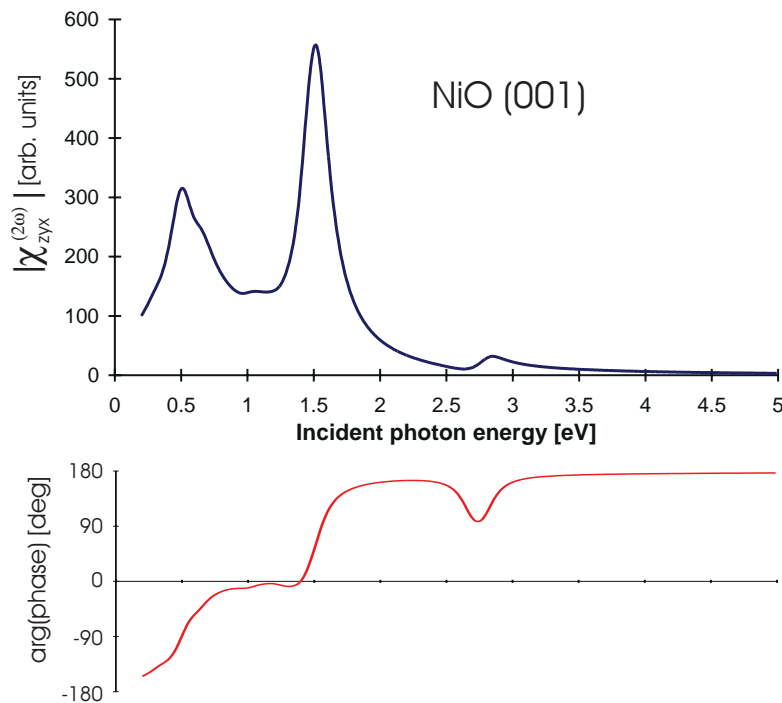


Figure 26: Spectrum of the antiferromagnetic tensor element χ_{zyx} . Both magnitude and the argument of the complex phase of the tensor element are presented separately.

esting result is that both tensor elements are of similar magnitude. This is a favorable condition for the antiferromagnetic domain imaging. Taking into account the magnitudes of both tensor elements presented in this section, domain contrast should be as large as in ferromagnets (where it is of the order of *unity* in SHG).

The results described here concern the process of static SHG, i.e. a measurement taken on a sample close to thermodynamic equilibrium. In the next section, we will describe our anticipations as to the dynamical (time-resolved) measurements of highly excited states in nickel oxide.

3.4 Spin and Charge Dynamics

The area of dynamics of magnetic materials on femto-second timescales escaped scientific investigations till very recently, both from theoretical and experimental point of view. However, the importance of understanding the dynamics in view of new challenges for the materials needed for storage and computer memory media becomes obvious. Only very recently seminal experimental works have been performed in the sub-picosecond regime for *ferromagnetic* materials [83, 84, 85, 86]. The very fact of the observed spin dynamics at these short timescales fostered the development of appropriate theoretical models, since the the spin-lattice relaxation processes, appearing at the timescales of several tens to hundreds of picoseconds [87] cannot be responsible for the observed effect. The con-

cept of different temperatures (charge, spin, and lattice temperature) used to explain the results [83, 84] is not strictly valid, since at so short timescales it is impossible to define a temperature, which is rather an equilibrium property. A proper models, dynamics of complex populations, have been developed for both linear [88] and nonlinear [89] magneto-optics from ferromagnets. However, the investigations of femtosecond spin-dynamics of antiferromagnets is nonexisting so far.

Here, we describe the simulation of an SHG pump-and-probe experiment in NiO. During such an experiment, the sample is excited by a strong laser pulse, and then (with a variable delay of several tens to hundreds of femtoseconds) the second - probe - pulse is issued. The SHG response of the sample to this second beam is measured and can reveal the dynamic properties of the sample. In this section, we

- describe the theoretical model for the dynamics and
- present and discuss the results of the calculations.

3.4.1 Treatment of Pump-Probe Experiments

In our work we extend the theory for probing the femtosecond spin-dynamics by means of nonlinear optics towards antiferromagnets. In fact, we choose the same approach as in [89] and add the initial excited state preparation and the dynamics of complex populations to our previously described theory of the static SHG response. The initial excitation is infinitesimally short in time (the excitation pulse is already completed when our dynamics starts) but its energy distribution follows a Gaussian profile, centered at 2 eV and with the width of 20 eV (truncated at 0 eV, so that no negative energies appear). This width of excitation allows us to probe the fast limit of the dynamics, since all the energy levels (including the highest) are populated and consequently all the de-excitation channels are open. The restriction of the Hamiltonian to electronic on-site interactions complies with this limit. Consequently, the excitation populates all the many-body states of our system, and then these states are left to evolve freely. Under these circumstances the time-dependent tensor element χ_{ijk} can be expressed as

$$\chi_{ijk}^{(2)}(2\mathbf{q}, 2\omega) = \frac{e^3}{2q^3V} \sum_{\mathbf{k}, l, l', l''} \left[\langle \mathbf{k} + 2\mathbf{q}, l'' | i | \mathbf{k} l \rangle \langle \mathbf{k} l | j | \mathbf{k} + \mathbf{q}, l' \rangle \langle \mathbf{k} + \mathbf{q}, l' | k | \mathbf{k} + 2\mathbf{q}, l'' \rangle \times \right. \\ \left. \times \frac{\frac{p(E_{\mathbf{k}+2\mathbf{q}, l''}, t) - p(E_{\mathbf{k}+\mathbf{q}, l'}, t)}{E_{\mathbf{k}+2\mathbf{q}, l''} - E_{\mathbf{k}+\mathbf{q}, l'} - \hbar\omega + i\hbar\alpha} - \frac{p(E_{\mathbf{k}+\mathbf{q}, l'}, t) - p(E_{\mathbf{k}l}, t)}{E_{\mathbf{k}+\mathbf{q}, l'} - E_{\mathbf{k}l} - \hbar\omega + i\hbar\alpha}}{E_{\mathbf{k}+2\mathbf{q}, l''} - E_{\mathbf{k}l} - 2\hbar\omega + 2i\hbar\alpha}} \right], \quad (3.7)$$

Here, $p(E_{\mathbf{k}l}, t) = \langle \Psi(t) | \mathbf{k} l \rangle = f(E) \times e^{-\frac{i}{\hbar} E_{\mathbf{k}l} t}$, and the rest of symbols are the same as in Eq. (3.1). The time evolution of the system exclusively results from the presence of the quantum phase factor. Broadening of many-body levels does not occur since the many-body Hamiltonian is diagonal due to the choice of the appropriate symmetry-adapted basis (as described in Sec. 3.2). Consequently, the effect described by us has a purely quantum nature and cannot be explain within a classical theory. As previously, the band structure is

neglected due to very small dispersion of the gap states which are involved in the described process. In the next subsection we present the results of the numerical simulations of the spin dynamics.

3.4.2 Relaxation of Excited States

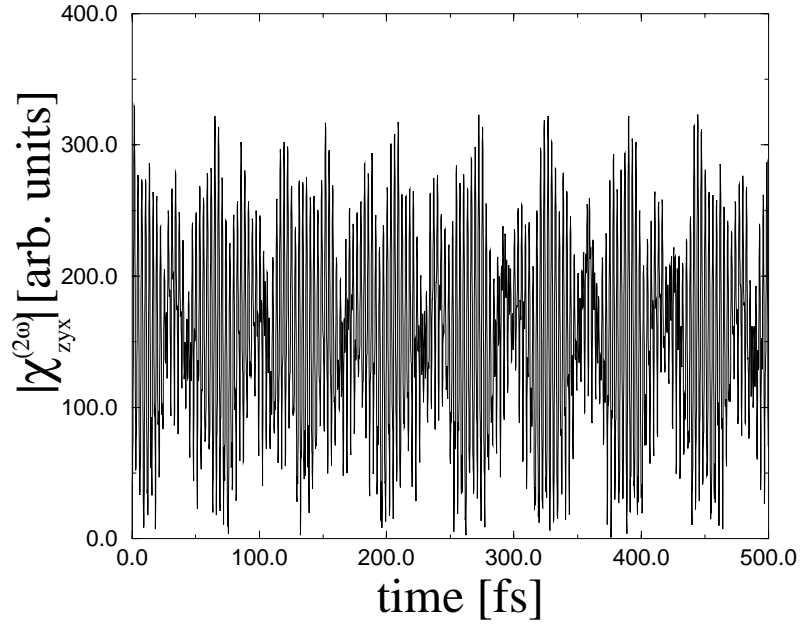
In this subsection, we present for the first time the femtosecond dynamics of the antiferromagnetic order parameter, represented by the antiferromagnetic tensor element χ_{zyx} . As it is clear from the Fig. 27a, there is no decay of the tensor element, like for the metallic systems. The coherence is preserved for a long time (until phenomena neglected within this framework take place, like phonon-magnon coupling), which manifests itself by beating repeated regularly every 50 fs. Fig. 27b presents a zoom into such a period of 50 fs, it demonstrates that the spin dynamics takes place within femtoseconds, and thus is not slower than in metals.

For comparison, we have also performed similar calculations for the paramagnetic tensor element χ_{zzz} . The results are shown in Fig. 28. The basic features are very similar to the dynamics of the antiferromagnetic tensor element described previously. The ultimate limit of the charge dynamics lies also within several femtoseconds, as it can be seen in Fig. 28b, and the coherence is preserved for a long time.

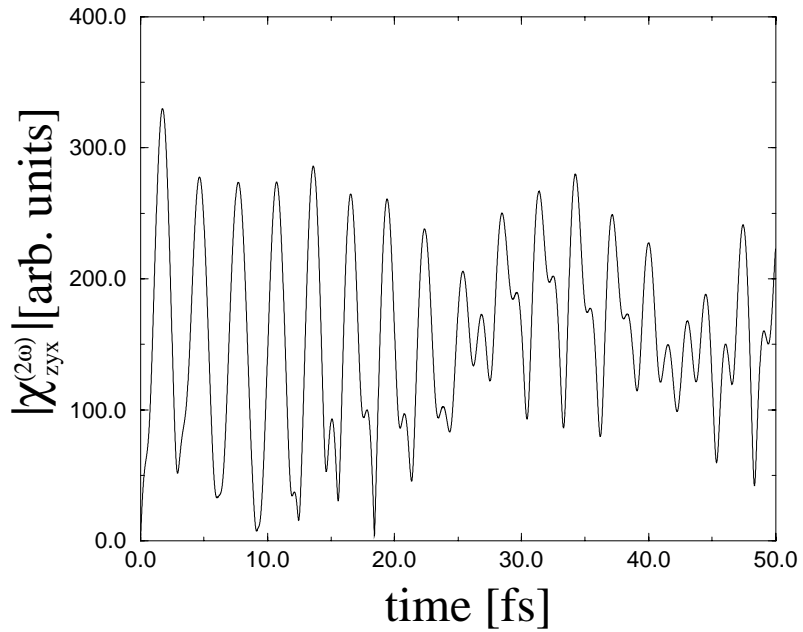
The coherence of the tensor elements determining the SHG response of the AF surface may be destroyed by the phonons, which were neglected in the current framework. As mentioned above, the phonon-magnon coupling intervenes within several tens of picoseconds. Consequently, the coherence times are four orders of magnitude longer than the ultimate speed of the spin and charge dynamics. Additional interactions, like electron-electron interactions of the nearest neighbors, band structure (hopping), or phonons, can bring decoherence. The question if this decay really occurs when these effects are taken into account remains open. However, by choice of a particular spectral line instead of the spectrally wide initial excitation described here one can make the coherence last longer (typical widths of spectral lines in oxides are in the range of tens of μeV [5], which corresponds to several picoseconds coherence times).

The situation where the elementary dynamics happens within femtoseconds and coherence is preserved beyond hundreds of femtoseconds is very favorable for the magneto-optic storage and quantum computing applications [90], since the spin dynamics determines the write and readout speed. Till now, only semiconductors have been known to fulfill this criterion, however the applications of those materials suffer from problems related to spin injection [91]. In the antiferromagnetic oxides no spin injection is necessary since the magnetic moments are already there.

This conclusion ends the description of the results of our femtosecond spin- and charge-dynamics. In the last chapter of this dissertation, we will present other conclusions, preceded by a brief summary of our results.

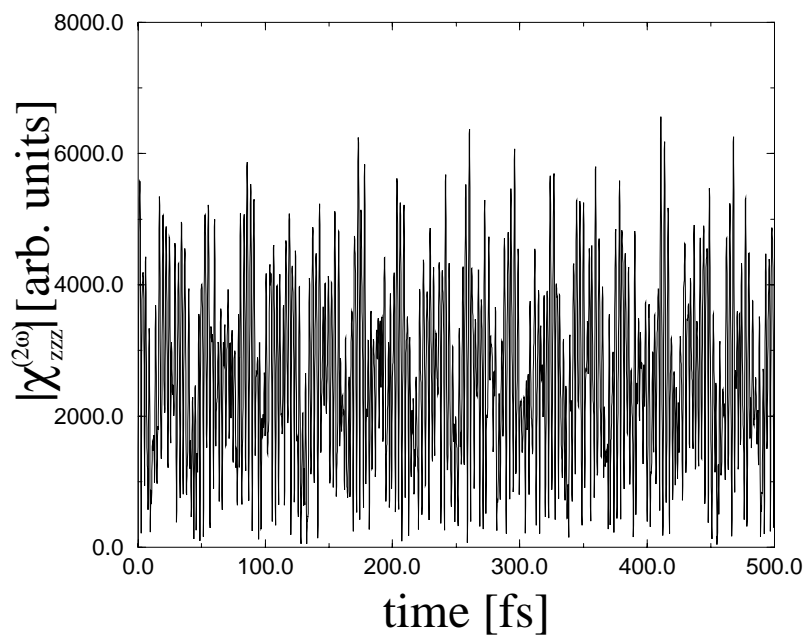


a

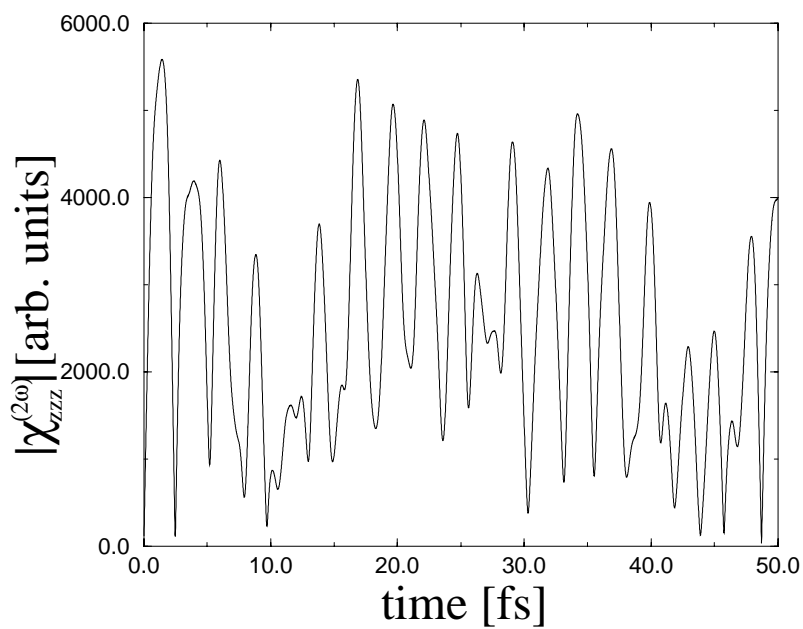


b

Figure 27: Dynamics of the antiferromagnetic tensor element χ_{zyx} on NiO (001) within 500 fs (a) and 50 fs (b). The incident photon energy of the probe pulse $\hbar\omega=1.44$ eV. The graphs present the magnitude of the complex tensor element.



a



b

Figure 28: Dynamics of the paramagnetic tensor element χ_{zzz} on NiO (001) within 500 fs (a) and 50 fs (b). The incident photon energy of the probe pulse $\hbar\omega=1.44$ eV. The graphs present the magnitude of the complex tensor element.

Chapter 4

Conclusions and Outlook

In this work, we have settled the theory for Second Harmonic Generation from antiferromagnetic interfaces. The importance of the antiferromagnetic oxide interfaces for the modern technology and material science has been outlined in the Introduction. The main conclusion of this work is that SHG possesses unique capabilities to address antiferromagnetic interfaces. In particular, the symmetry analysis of the nonlinear magneto-optical response, described in the Chapter 2 of this work, demonstrates the potential of SHG to:

- distinguish magnetic phases of the surface, in particular detect surface antiferromagnetism,
- distinguish detailed spin configurations of the AF surface,
- indicate for the distortions of the lattice
- image the AF surface domains

As proposed by us in the Subsec. 2.3.8, these results can be experimentally obtained by the appropriate choice of geometry. The analysis was applied both to stand-alone monolayers and to double layers (which represent fully the semi-infinite material) and is thus complete.

In addition to the symmetry analysis of the nonlinear magneto-optics we have, for the first time, discussed the validity of applying time-reversal symmetry to classify the SHG response. Our results show that the presence of dissipation in the frequency space makes the process of SHG dynamical and thus irreversible. Only the combination of SHG and antiferromagnetism fully reveals the complications that time-reversal operation imposes in nonlinear magneto-optics.

In the Chapter 3 of this work we have presented an electronic calculation which supports the above mentioned conclusions. The quantitative result of this calculation is that we expect the effect from the antiferromagnetic surfaces to be of the same order of magnitude as SHG from ferromagnetic surfaces, which had been proven measurable. In an experiment, one can exploit a spectral line specific for antiferromagnetism, visible even on top of a ferromagnetic background.

An important outcome of our electronic calculation is the first ever presentation of nonlinear magneto-optical spectra of NiO (Sec. 3.3). Using them, spectral lines favorable

for the experimental nonlinear optics and magneto-optics can be determined. Although the used approximations do not allow for quantitative predictions of the peak heights in the spectrum, peak positions are *reliable*.

The results of the dynamics calculations (Sec. 3.4), simulating a time-resolved pump-and-probe SHG experiment, allow to make some interesting assertions about the investigated systems. In antiferromagnetic oxides, the negligible dispersion of the gap states (which are the most important ones contributing to the surface SHG) prohibits the decay of the tensor elements, unlike for metallic systems. On the other hand, the fast limit of the dynamics in our system is demonstrated to lie within a few femtoseconds. These characteristics make the antiferromagnetic oxides ideal materials for modern applications like quantum computing and magneto-optical storage, even more since no spin injection is needed.

In conclusion, our work has demonstrated that antiferromagnetic oxides, in particular NiO, have many interesting properties which will certainly draw even more attention to this class of materials, and that SHG is a quite unique tool to address these properties.

Our theory, though it yields important and reliable results, is not yet complete. The improvement of our analytic tools will go in the direction of obtaining more quantitative results. For that purpose, a more realistic estimate of transition matrix elements will be indispensable. Actually, a proper *calculation* of these transition matrix elements will make our theory fully *ab initio*, but this will not be possible in the near future. An extension to the current state of our theory which will be easier to implement but which is also quite interesting will be taking into account the three- and four hole states. Their application has already been prepared, since we have determined these states and their energies for the spherically-symmetric environment. Another point which we intend to implement is taking into account the band structure. The dispersion of the gap states, although very small, can help us in determining the long-time limit of the coherence times.

These improvements will provide an even more complete description of nonlinear magneto-optics from antiferromagnetic surfaces of nickel oxide.

Appendix A

Tables

Table A.1: Symmetry-adapted linear combinations of two-hole products

symmetry-adapted state	linear combination of simple products
1S	$\sqrt{\frac{1}{5}}[1, 10, 11, 12] - \sqrt{\frac{1}{5}}[3, 8, 11, 12] + \sqrt{\frac{1}{5}}[5, 6, 11, 12] + \sqrt{\frac{1}{5}}[4, 7, 11, 12] - \sqrt{\frac{1}{5}}[2, 9, 11, 12]$
$^1D_{-2}$	$\sqrt{\frac{2}{7}}[1, 6, 11, 12] - \sqrt{\frac{3}{7}}[3, 4, 11, 12] - \sqrt{\frac{2}{7}}[2, 5, 11, 12]$
$^1D_{-1}$	$\sqrt{\frac{3}{7}}[1, 8, 11, 12] - \sqrt{\frac{1}{14}}[3, 6, 11, 12] + \sqrt{\frac{1}{14}}[4, 5, 11, 12] - \sqrt{\frac{3}{7}}[2, 7, 11, 12]$
1D_0	$\sqrt{\frac{2}{7}}[1, 10, 11, 12] + \sqrt{\frac{1}{14}}[3, 8, 11, 12] - \sqrt{\frac{2}{7}}[5, 6, 11, 12] - \sqrt{\frac{1}{14}}[4, 7, 11, 12] - \sqrt{\frac{2}{7}}[2, 9, 11, 12]$
1D_1	$-\sqrt{\frac{3}{7}}[4, 9, 11, 12] + \sqrt{\frac{1}{14}}[6, 7, 11, 12] - \sqrt{\frac{1}{14}}[5, 8, 11, 12] + \sqrt{\frac{3}{7}}[3, 10, 11, 12]$
1D_2	$-\sqrt{\frac{2}{7}}[6, 9, 11, 12] - \sqrt{\frac{3}{7}}[7, 8, 11, 12] + \sqrt{\frac{2}{7}}[5, 10, 11, 12]$
$^1G_{-4}$	$[1, 2, 11, 12]$
$^1G_{-3}$	$-\sqrt{\frac{1}{2}}[2, 3, 11, 12] + \sqrt{\frac{1}{2}}[1, 4, 11, 12]$
$^1G_{-2}$	$\sqrt{\frac{3}{14}}[1, 6, 11, 12] + \sqrt{\frac{4}{7}}[3, 4, 11, 12] - \sqrt{\frac{3}{14}}[2, 5, 11, 12]$
$^1G_{-1}$	$\sqrt{\frac{1}{14}}[1, 8, 11, 12] + \sqrt{\frac{3}{7}}[3, 6, 11, 12] - \sqrt{\frac{3}{7}}[4, 5, 11, 12] - \sqrt{\frac{1}{14}}[2, 7, 11, 12]$
1G_0	$\sqrt{\frac{1}{70}}[1, 10, 11, 12] + \sqrt{\frac{8}{35}}[3, 8, 11, 12] + \sqrt{\frac{18}{35}}[5, 6, 11, 12] - \sqrt{\frac{8}{35}}[4, 7, 11, 12] - \sqrt{\frac{1}{70}}[2, 9, 11, 12]$
1G_1	$-\sqrt{\frac{1}{14}}[4, 9, 11, 12] - \sqrt{\frac{3}{7}}[6, 7, 11, 12] + \sqrt{\frac{3}{7}}[5, 8, 11, 12] + \sqrt{\frac{1}{14}}[3, 10, 11, 12]$
1G_2	$-\sqrt{\frac{3}{14}}[6, 9, 11, 12] + \sqrt{\frac{4}{7}}[7, 8, 11, 12] + \sqrt{\frac{3}{14}}[5, 10, 11, 12]$
1G_3	$\sqrt{\frac{1}{2}}[7, 10, 11, 12] - \sqrt{\frac{1}{2}}[8, 9, 11, 12]$
$^1G_{-4}$	$[9, 10, 11, 12]$

Table A.1: Symmetry-adapted linear combinations of two-hole products

symmetry-adapted state	linear combination of simple products
${}^3P_{-1}^{\uparrow\uparrow}$	$\sqrt{\frac{2}{5}}[1, 7, 11, 12] - \sqrt{\frac{3}{5}}[3, 5, 11, 12]$
${}^3P_0^{\uparrow\uparrow}$	$\sqrt{\frac{4}{5}}[1, 9, 11, 12] - \sqrt{\frac{1}{5}}[3, 7, 11, 12]$
${}^3P_1^{\uparrow\uparrow}$	$-\sqrt{\frac{2}{5}}[3, 9, 11, 12] + \sqrt{\frac{3}{5}}[5, 7, 11, 12]$
${}^3P_{-1}^{\uparrow\downarrow}$	$-\sqrt{\frac{1}{5}}[1, 8, 11, 12] + \sqrt{\frac{3}{10}}[3, 6, 11, 12] + \sqrt{\frac{3}{10}}[4, 5, 11, 12] - \sqrt{\frac{1}{5}}[2, 7, 11, 12]$
${}^3P_0^{\uparrow\downarrow}$	$-\sqrt{\frac{2}{5}}[1, 10, 11, 12] + \sqrt{\frac{1}{10}}[3, 8, 11, 12] + \sqrt{\frac{1}{10}}[4, 7, 11, 12] - \sqrt{\frac{2}{5}}[2, 9, 11, 12]$
${}^3P_1^{\uparrow\downarrow}$	$\sqrt{\frac{1}{5}}[4, 9, 11, 12] - \sqrt{\frac{3}{10}}[6, 7, 11, 12] - \sqrt{\frac{3}{10}}[5, 8, 11, 12] + \sqrt{\frac{1}{5}}[3, 10, 11, 12]$
${}^3P_{-1}^{\downarrow\downarrow}$	$\sqrt{\frac{2}{5}}[2, 8, 11, 12] - \sqrt{\frac{3}{5}}[4, 6, 11, 12]$
${}^3P_0^{\downarrow\downarrow}$	$\sqrt{\frac{4}{5}}[2, 10, 11, 12] - \sqrt{\frac{1}{5}}[4, 8, 11, 12]$
${}^3P_1^{\downarrow\downarrow}$	$-\sqrt{\frac{2}{5}}[4, 10, 11, 12] + \sqrt{\frac{3}{5}}[6, 8, 11, 12]$
${}^3F_{-3}^{\uparrow\uparrow}$	$[1, 3, 11, 12]$
${}^3F_{-2}^{\uparrow\uparrow}$	$[1, 5, 11, 12]$
${}^3F_{-1}^{\uparrow\uparrow}$	$\sqrt{\frac{3}{5}}[1, 7, 11, 12] + \sqrt{\frac{2}{5}}[3, 5, 11, 12]$
${}^3F_0^{\uparrow\uparrow}$	$\sqrt{\frac{4}{5}}[1, 9, 11, 12] + \sqrt{\frac{4}{5}}[3, 7, 11, 12]$
${}^3F_1^{\uparrow\uparrow}$	$-\sqrt{\frac{3}{5}}[3, 9, 11, 12] - \sqrt{\frac{2}{5}}[5, 7, 11, 12]$
${}^3F_2^{\uparrow\uparrow}$	$[5, 9, 11, 12]$
${}^3F_3^{\uparrow\uparrow}$	$[7, 9, 11, 12]$
${}^3F_{-3}^{\uparrow\downarrow}$	$\sqrt{\frac{1}{2}}[2, 3, 11, 12] + \sqrt{\frac{1}{2}}[1, 4, 11, 12]$
${}^3F_{-2}^{\uparrow\downarrow}$	$\sqrt{\frac{1}{2}}[2, 5, 11, 12] + \sqrt{\frac{1}{2}}[1, 6, 11, 12]$
${}^3F_{-1}^{\uparrow\downarrow}$	$\sqrt{\frac{3}{10}}[2, 7, 11, 12] + \sqrt{\frac{1}{5}}[4, 5, 11, 12] + \sqrt{\frac{1}{5}}[3, 6, 11, 12] + \sqrt{\frac{3}{10}}[1, 8, 11, 12]$
${}^3F_0^{\uparrow\downarrow}$	$-\sqrt{\frac{1}{10}}[1, 10, 11, 12] - \sqrt{\frac{2}{5}}[3, 8, 11, 12] - \sqrt{\frac{2}{5}}[4, 7, 11, 12] - \sqrt{\frac{1}{10}}[2, 9, 11, 12]$
${}^3F_1^{\uparrow\downarrow}$	$-\sqrt{\frac{3}{10}}[3, 10, 11, 12] - \sqrt{\frac{1}{5}}[5, 8, 11, 12] - \sqrt{\frac{1}{5}}[6, 7, 11, 12] - \sqrt{\frac{3}{10}}[4, 9, 11, 12]$
${}^3F_2^{\uparrow\downarrow}$	$-\sqrt{\frac{1}{2}}[5, 10, 11, 12] - \sqrt{\frac{1}{2}}[6, 9, 11, 12]$
${}^3F_3^{\uparrow\downarrow}$	$-\sqrt{\frac{1}{2}}[7, 10, 11, 12] - \sqrt{\frac{1}{2}}[8, 9, 11, 12]$
${}^3F_{-3}^{\downarrow\downarrow}$	$[2, 4, 11, 12]$
${}^3F_{-2}^{\downarrow\downarrow}$	$[2, 6, 11, 12]$
${}^3F_{-1}^{\downarrow\downarrow}$	$\sqrt{\frac{3}{5}}[2, 8, 11, 12] + \sqrt{\frac{2}{5}}[4, 6, 11, 12]$
${}^3F_0^{\downarrow\downarrow}$	$\sqrt{\frac{1}{5}}[2, 10, 11, 12] + \sqrt{\frac{4}{5}}[4, 8, 11, 12]$
${}^3F_1^{\downarrow\downarrow}$	$-\sqrt{\frac{3}{5}}[4, 10, 11, 12] - \sqrt{\frac{2}{5}}[6, 8, 11, 12]$
${}^3F_2^{\downarrow\downarrow}$	$-[6, 10, 11, 12]$
${}^3F_3^{\downarrow\downarrow}$	$-[8, 10, 11, 12]$

Table A.2: Symmetry-adapted linear combinations of three-hole products

symmetry-adapted state	linear combination of simple products
${}^2P_{-1}^\uparrow$	$\sqrt{\frac{2}{35}}[1, 4, 9, 11] + \sqrt{\frac{16}{105}}[1, 5, 8, 11] - \sqrt{\frac{8}{35}}[1, 3, 10, 11] + \sqrt{\frac{1}{105}}[1, 6, 7, 11] +$ $+\sqrt{\frac{2}{35}}[2, 3, 9, 11] - \sqrt{\frac{9}{70}}[3, 4, 7, 11] - \sqrt{\frac{9}{70}}[3, 5, 6, 11] - \sqrt{\frac{5}{21}}[2, 5, 7, 11]$
${}^2P_0^\uparrow$	$-\sqrt{\frac{8}{105}}[1, 5, 10, 11] + \sqrt{\frac{35}{105}}[1, 6, 9, 11] + \sqrt{\frac{9}{35}}[1, 7, 8, 11] - \sqrt{\frac{8}{105}}[2, 5, 9, 11] +$ $-\sqrt{\frac{9}{35}}[3, 4, 9, 11] - \sqrt{\frac{1}{210}}[3, 5, 8, 11] + \sqrt{\frac{2}{105}}[3, 6, 7, 11] - \sqrt{\frac{1}{210}}[4, 5, 7, 11]$
${}^2P_1^\uparrow$	$-\sqrt{\frac{2}{35}}[1, 8, 9, 11] - \sqrt{\frac{16}{105}}[4, 5, 9, 11] + \sqrt{\frac{8}{35}}[2, 7, 9, 11] - \sqrt{\frac{1}{105}}[3, 6, 9, 11] +$ $-\sqrt{\frac{2}{35}}[1, 7, 10, 11] - \sqrt{\frac{9}{70}}[3, 7, 8, 11] - \sqrt{\frac{9}{70}}[5, 6, 7, 11] + \sqrt{\frac{5}{21}}[3, 5, 10, 11]$
${}^2P_{-1}^\downarrow$	$\sqrt{\frac{2}{35}}[2, 3, 10, 11] + \sqrt{\frac{16}{105}}[2, 6, 7, 11] - \sqrt{\frac{8}{35}}[2, 4, 9, 11] + \sqrt{\frac{1}{105}}[2, 5, 8, 11] +$ $+\sqrt{\frac{2}{35}}[1, 4, 10, 11] + \sqrt{\frac{9}{70}}[3, 4, 8, 11] + \sqrt{\frac{9}{70}}[4, 5, 6, 11] - \sqrt{\frac{5}{21}}[1, 6, 8, 11]$
${}^2P_0^\downarrow$	$-\sqrt{\frac{8}{105}}[2, 6, 9, 11] + \sqrt{\frac{32}{105}}[2, 5, 10, 11] - \sqrt{\frac{9}{35}}[2, 7, 8, 11] - \sqrt{\frac{8}{105}}[1, 6, 10, 11] +$ $+\sqrt{\frac{9}{39}}[3, 4, 10, 11] - \sqrt{\frac{1}{210}}[4, 6, 7, 11] + \sqrt{\frac{2}{105}}[4, 5, 8, 11] - \sqrt{\frac{1}{210}}[3, 6, 8, 11]$
${}^2P_1^\downarrow$	$-\sqrt{\frac{2}{35}}[2, 7, 10, 11] - \sqrt{\frac{16}{105}}[3, 6, 10, 11] + \sqrt{\frac{8}{35}}[1, 8, 10, 11] - \sqrt{\frac{1}{105}}[4, 5, 10, 11] +$ $-\sqrt{\frac{2}{35}}[2, 8, 9, 11] + \sqrt{\frac{9}{70}}[4, 7, 8, 11] + \sqrt{\frac{9}{70}}[5, 6, 8, 11] + \sqrt{\frac{5}{21}}[4, 6, 9, 11]$
${}^2D_{-2}^\uparrow(1)$	$-\frac{1}{2}[1, 2, 9, 11] - \frac{1}{2}[1, 3, 8, 11] + \frac{1}{2}[1, 4, 7, 11] + \frac{1}{2}[1, 5, 6, 11]$
${}^2D_{-1}^\uparrow(1)$	$-\frac{1}{2}[1, 3, 10, 11] + \frac{1}{2}[2, 3, 9, 11] + \frac{1}{2}[3, 4, 7, 11] + \frac{1}{2}[3, 5, 6, 11]$
${}^2D_0^\uparrow(1)$	$-\frac{1}{2}[1, 5, 10, 11] + \frac{1}{2}[2, 5, 9, 11] + \frac{1}{2}[3, 5, 8, 11] - \frac{1}{2}[4, 5, 7, 11]$
${}^2D_1^\uparrow(1)$	$\frac{1}{2}[2, 7, 9, 11] - \frac{1}{2}[1, 7, 10, 11] + \frac{1}{2}[3, 7, 8, 11] + \frac{1}{2}[5, 6, 7, 11]$
${}^2D_2^\uparrow(1)$	$-\frac{1}{2}[1, 9, 10, 11] + \frac{1}{2}[4, 7, 9, 11] - \frac{1}{2}[3, 8, 9, 11] + \frac{1}{2}[5, 6, 9, 11]$
${}^2D_{-2}^\downarrow(1)$	$\frac{1}{2}[1, 2, 10, 11] - \frac{1}{2}[2, 4, 7, 11] + \frac{1}{2}[2, 3, 8, 11] - \frac{1}{2}[2, 5, 6, 11]$
${}^2D_{-1}^\downarrow(1)$	$-\frac{1}{2}[2, 4, 9, 11] + \frac{1}{2}[1, 4, 10, 11] - \frac{1}{2}[3, 4, 8, 11] - \frac{1}{2}[4, 5, 6, 11]$
${}^2D_0^\downarrow(1)$	$-\frac{1}{2}[2, 6, 9, 11] + \frac{1}{2}[1, 6, 10, 11] + \frac{1}{2}[4, 6, 7, 11] - \frac{1}{2}[3, 6, 8, 11]$
${}^2D_1^\downarrow(1)$	$\frac{1}{2}[1, 8, 10, 11] - \frac{1}{2}[2, 8, 9, 11] - \frac{1}{2}[4, 7, 8, 11] - \frac{1}{2}[5, 6, 8, 11]$
${}^2D_2^\downarrow(1)$	$\frac{1}{2}[2, 9, 10, 11] + \frac{1}{2}[3, 8, 10, 11] - \frac{1}{2}[4, 7, 10, 11] - \frac{1}{2}[5, 6, 10, 11]$
${}^2D_{-2}^\uparrow(2)$	$\sqrt{\frac{25}{84}}[1, 2, 9, 11] - \sqrt{\frac{3}{28}}[1, 3, 8, 11] - \sqrt{\frac{1}{84}}[1, 4, 7, 11] + \sqrt{\frac{3}{28}}[1, 5, 6, 11] +$ $+\sqrt{\frac{4}{21}}[2, 3, 7, 11] + \sqrt{\frac{2}{7}}[3, 4, 5, 11]$
${}^2D_{-1}^\uparrow(2)$	$-\sqrt{\frac{3}{28}}[1, 3, 10, 11] + \sqrt{\frac{4}{21}}[1, 4, 9, 11] - \sqrt{\frac{2}{7}}[1, 6, 7, 11] - \sqrt{\frac{1}{84}}[2, 3, 9, 11] +$ $+\sqrt{\frac{2}{7}}[2, 5, 7, 11] + \sqrt{\frac{1}{84}}[3, 4, 7, 11] - \sqrt{\frac{3}{28}}[3, 5, 6, 11]$
${}^2D_0^\uparrow(2)$	$-\sqrt{\frac{3}{28}}[1, 5, 10, 11] + \sqrt{\frac{2}{7}}[1, 7, 8, 11] + \sqrt{\frac{3}{28}}[2, 5, 9, 11] + \sqrt{\frac{2}{7}}[3, 4, 9, 11] +$ $-\sqrt{\frac{3}{28}}[3, 5, 8, 11] + \sqrt{\frac{3}{28}}[4, 5, 7, 11]$
${}^2D_1^\uparrow(2)$	$\sqrt{\frac{3}{28}}[2, 7, 9, 11] - \sqrt{\frac{4}{21}}[1, 8, 9, 11] + \sqrt{\frac{2}{7}}[3, 6, 9, 11] + \sqrt{\frac{1}{84}}[1, 7, 10, 11] +$ $-\sqrt{\frac{2}{7}}[3, 5, 10, 11] + \sqrt{\frac{1}{84}}[3, 7, 8, 11] - \sqrt{\frac{3}{28}}[5, 6, 7, 11]$
${}^2D_2^\uparrow(2)$	$\sqrt{\frac{25}{84}}[1, 9, 10, 11] + \sqrt{\frac{3}{28}}[4, 7, 9, 11] + \sqrt{\frac{1}{84}}[3, 8, 9, 11] + \sqrt{\frac{3}{28}}[5, 6, 9, 11] +$ $-\sqrt{\frac{4}{21}}[3, 7, 10, 11] + \sqrt{\frac{2}{7}}[5, 7, 8, 11]$

Table A.2: Symmetry-adapted linear combinations of three-hole products

symmetry-adapted state	linear combination of simple products
${}^2D_{-2}^\downarrow(2)$	$-\sqrt{\frac{25}{84}}[1, 2, 10, 11] - \sqrt{\frac{3}{28}}[2, 4, 7, 11] - \sqrt{\frac{1}{84}}[2, 3, 8, 11] - \sqrt{\frac{3}{28}}[2, 5, 6, 11] +$ $+\sqrt{\frac{4}{21}}[1, 4, 8, 11] - \sqrt{\frac{2}{7}}[3, 4, 6, 11]$
${}^2D_{-1}^\downarrow(2)$	$-\sqrt{\frac{3}{28}}[2, 4, 9, 11] + \sqrt{\frac{4}{21}}[2, 3, 10, 11] - \sqrt{\frac{2}{7}}[2, 5, 8, 11] - \sqrt{\frac{1}{84}}[1, 4, 10, 11] +$ $+\sqrt{\frac{2}{7}}[1, 6, 8, 11] - \sqrt{\frac{1}{84}}[3, 4, 8, 11] + \sqrt{\frac{3}{28}}[4, 5, 6, 11]$
${}^2D_0^\downarrow(2)$	$-\sqrt{\frac{3}{28}}[2, 6, 9, 11] - \sqrt{\frac{2}{7}}[2, 7, 8, 11] + \sqrt{\frac{3}{28}}[1, 6, 10, 11] - \sqrt{\frac{2}{7}}[3, 4, 10, 11] +$ $-\sqrt{\frac{3}{28}}[4, 6, 7, 11] + \sqrt{\frac{3}{28}}[3, 6, 8, 11]$
${}^2D_1^\downarrow(2)$	$\sqrt{\frac{3}{28}}[1, 8, 10, 11] - \sqrt{\frac{4}{21}}[2, 7, 10, 11] + \sqrt{\frac{2}{7}}[4, 5, 10, 11] + \sqrt{\frac{1}{84}}[2, 8, 9, 11] +$ $-\sqrt{\frac{2}{7}}[4, 6, 9, 11] - \sqrt{\frac{1}{84}}[4, 7, 8, 11] + \sqrt{\frac{3}{28}}[5, 6, 8, 11]$
${}^2D_2^\downarrow(2)$	$-\sqrt{\frac{25}{84}}[2, 9, 10, 11] + \sqrt{\frac{3}{28}}[3, 8, 10, 11] + \sqrt{\frac{1}{84}}[4, 7, 10, 11] - \sqrt{\frac{3}{28}}[5, 6, 10, 11] +$ $-\sqrt{\frac{4}{21}}[4, 8, 9, 11] - \sqrt{\frac{2}{7}}[6, 7, 8, 11]$
${}^2F_{-3}^\uparrow$	$\sqrt{\frac{1}{2}}[1, 2, 7, 11] - \sqrt{\frac{1}{12}}[1, 4, 5, 11] - \sqrt{\frac{1}{12}}[1, 3, 6, 11] + \sqrt{\frac{1}{3}}[2, 3, 5, 11]$
${}^2F_{-2}^\uparrow$	$\sqrt{\frac{1}{3}}[1, 2, 9, 11] - \sqrt{\frac{1}{12}}[1, 3, 8, 11] + \sqrt{\frac{1}{12}}[1, 4, 7, 11] - \sqrt{\frac{1}{2}}[3, 4, 5, 11]$
${}^2F_{-1}^\uparrow$	$-\sqrt{\frac{1}{30}}[1, 3, 10, 11] + \sqrt{\frac{3}{10}}[1, 4, 9, 11] - \sqrt{\frac{1}{20}}[1, 5, 8, 11] + \sqrt{\frac{1}{20}}[1, 6, 7, 11] +$ $-\sqrt{\frac{2}{15}}[2, 3, 9, 11] - \sqrt{\frac{2}{15}}[3, 4, 7, 11] + \sqrt{\frac{3}{10}}[3, 5, 6, 11]$
${}^2F_0^\uparrow$	$-\sqrt{\frac{1}{15}}[1, 5, 10, 11] + \sqrt{\frac{4}{15}}[1, 6, 9, 11] - \sqrt{\frac{1}{10}}[1, 7, 8, 11] - \sqrt{\frac{1}{15}}[2, 5, 9, 11] +$ $+\sqrt{\frac{1}{10}}[3, 4, 9, 11] + \sqrt{\frac{1}{15}}[3, 5, 8, 11] - \sqrt{\frac{4}{15}}[3, 6, 7, 11] + \sqrt{\frac{1}{15}}[4, 5, 7, 11]$
${}^2F_1^\uparrow$	$\sqrt{\frac{1}{30}}[2, 7, 9, 11] - \sqrt{\frac{3}{10}}[1, 8, 9, 11] + \sqrt{\frac{1}{20}}[4, 5, 9, 11] - \sqrt{\frac{1}{20}}[3, 6, 9, 11] +$ $+\sqrt{\frac{2}{15}}[1, 7, 10, 11] - \sqrt{\frac{2}{15}}[3, 7, 8, 11] + \sqrt{\frac{3}{10}}[5, 6, 7, 11]$
${}^2F_2^\uparrow$	$\sqrt{\frac{1}{3}}[1, 9, 10, 11] + \sqrt{\frac{1}{12}}[4, 7, 9, 11] - \sqrt{\frac{1}{12}}[3, 8, 9, 11] - \sqrt{\frac{1}{2}}[5, 7, 8, 11]$
${}^2F_3^\uparrow$	$\sqrt{\frac{1}{2}}[3, 9, 10, 11] + \sqrt{\frac{1}{12}}[5, 8, 9, 11] + \sqrt{\frac{1}{12}}[6, 7, 9, 11] - \sqrt{\frac{1}{3}}[5, 7, 10, 11]$
${}^2F_{-3}^\downarrow$	$-\sqrt{\frac{1}{2}}[1, 2, 8, 11] - \sqrt{\frac{1}{12}}[2, 3, 6, 11] - \sqrt{\frac{1}{12}}[2, 4, 5, 11] + \sqrt{\frac{1}{3}}[1, 4, 6, 11]$
${}^2F_{-2}^\downarrow$	$-\sqrt{\frac{1}{3}}[1, 2, 10, 11] - \sqrt{\frac{1}{12}}[2, 4, 7, 11] + \sqrt{\frac{1}{12}}[2, 3, 8, 11] + \sqrt{\frac{1}{2}}[3, 4, 6, 11]$
${}^2F_{-1}^\downarrow$	$-\sqrt{\frac{1}{30}}[2, 4, 9, 11] + \sqrt{\frac{3}{10}}[2, 3, 10, 11] - \sqrt{\frac{1}{20}}[2, 6, 7, 11] + \sqrt{\frac{1}{20}}[2, 5, 8, 11] +$ $-\sqrt{\frac{2}{15}}[1, 4, 10, 11] + \sqrt{\frac{2}{15}}[3, 4, 8, 11] - \sqrt{\frac{3}{10}}[4, 5, 6, 11]$
${}^2F_0^\downarrow$	$-\sqrt{\frac{1}{15}}[2, 6, 9, 11] + \sqrt{\frac{4}{15}}[2, 5, 10, 11] + \sqrt{\frac{1}{10}}[2, 7, 8, 11] - \sqrt{\frac{1}{15}}[1, 6, 10, 11] +$ $-\sqrt{\frac{1}{10}}[3, 4, 10, 11] + \sqrt{\frac{1}{15}}[4, 6, 7, 11] - \sqrt{\frac{4}{15}}[4, 5, 8, 11] + \sqrt{\frac{1}{15}}[3, 6, 8, 11]$
${}^2F_1^\downarrow$	$\sqrt{\frac{1}{30}}[1, 8, 10, 11] - \sqrt{\frac{3}{10}}[2, 7, 10, 11] + \sqrt{\frac{1}{20}}[3, 6, 10, 11] - \sqrt{\frac{1}{20}}[4, 5, 10, 11] +$ $+\sqrt{\frac{2}{15}}[2, 8, 9, 11] + \sqrt{\frac{2}{15}}[4, 7, 8, 11] - \sqrt{\frac{3}{10}}[5, 6, 8, 11]$
${}^2F_2^\downarrow$	$-\sqrt{\frac{1}{3}}[2, 9, 10, 11] + \sqrt{\frac{1}{12}}[3, 8, 10, 11] - \sqrt{\frac{1}{12}}[4, 7, 10, 11] + \sqrt{\frac{1}{2}}[6, 7, 8, 11]$
${}^2F_3^\downarrow$	$-\sqrt{\frac{1}{2}}[4, 9, 10, 11] + \sqrt{\frac{1}{12}}[6, 7, 10, 11] + \sqrt{\frac{1}{12}}[5, 8, 10, 11] - \sqrt{\frac{1}{3}}[6, 8, 9, 11]$
${}^2G_{-4}^\uparrow$	$-\sqrt{\frac{2}{5}}[1, 2, 5, 11] - \sqrt{\frac{3}{5}}[1, 3, 4, 11]$

Table A.2: Symmetry-adapted linear combinations of three-hole products

symmetry-adapted state	linear combination of simple products
${}^2G_{-3}^\uparrow$	$-\sqrt{\frac{3}{10}}[1, 2, 7, 11] + \sqrt{\frac{1}{20}}[1, 4, 5, 11] - \sqrt{\frac{9}{20}}[1, 3, 6, 11] + \sqrt{\frac{1}{5}}[2, 3, 5, 11]$
${}^2G_{-2}^\uparrow$	$-\sqrt{\frac{3}{35}}[1, 2, 9, 11] - \sqrt{\frac{27}{140}}[1, 3, 8, 11] - \sqrt{\frac{3}{140}}[1, 4, 7, 11] - \sqrt{\frac{12}{35}}[1, 5, 6, 11] +$ $+\sqrt{\frac{12}{35}}[2, 3, 7, 11] - \sqrt{\frac{1}{70}}[3, 4, 5, 11]$
${}^2G_{-1}^\uparrow$	$-\sqrt{\frac{3}{70}}[1, 3, 10, 11] - \sqrt{\frac{3}{70}}[1, 4, 9, 11] - \sqrt{\frac{7}{20}}[1, 5, 8, 11] + \sqrt{\frac{9}{140}}[1, 6, 7, 11] +$ $+\sqrt{\frac{6}{35}}[2, 3, 9, 11] + \sqrt{\frac{4}{35}}[2, 5, 7, 11] - \sqrt{\frac{6}{35}}[3, 4, 7, 11] - \sqrt{\frac{3}{70}}[3, 5, 6, 11]$
${}^2G_0^\uparrow$	$-\sqrt{\frac{1}{7}}[1, 5, 10, 11] - \sqrt{\frac{3}{14}}[1, 7, 8, 11] + \sqrt{\frac{1}{7}}[2, 5, 9, 11] - \sqrt{\frac{3}{14}}[3, 4, 9, 11] +$ $-\sqrt{\frac{1}{7}}[3, 5, 8, 11] + \sqrt{\frac{1}{7}}[4, 5, 7, 11]$
${}^2G_1^\uparrow$	$\sqrt{\frac{3}{70}}[2, 7, 9, 11] + \sqrt{\frac{3}{70}}[1, 8, 9, 11] + \sqrt{\frac{7}{20}}[4, 5, 9, 11] - \sqrt{\frac{9}{140}}[3, 6, 9, 11] +$ $-\sqrt{\frac{6}{35}}[1, 7, 10, 11] - \sqrt{\frac{4}{35}}[3, 5, 10, 11] - \sqrt{\frac{6}{35}}[3, 7, 8, 11] - \sqrt{\frac{3}{70}}[5, 6, 7, 11]$
${}^2G_2^\uparrow$	$-\sqrt{\frac{3}{35}}[1, 9, 10, 11] + \sqrt{\frac{27}{140}}[4, 7, 9, 11] + \sqrt{\frac{3}{140}}[3, 8, 9, 11] - \sqrt{\frac{12}{35}}[5, 6, 9, 11] +$ $-\sqrt{\frac{12}{35}}[3, 7, 10, 11] - \sqrt{\frac{1}{70}}[5, 7, 8, 11]$
${}^2G_3^\uparrow$	$-\sqrt{\frac{3}{10}}[3, 9, 10, 11] - \sqrt{\frac{1}{20}}[5, 8, 9, 11] + \sqrt{\frac{9}{20}}[6, 7, 9, 11] - \sqrt{\frac{1}{5}}[5, 7, 10, 11]$
${}^2G_4^\uparrow$	$-\sqrt{\frac{2}{5}}[5, 9, 10, 11] - \sqrt{\frac{3}{5}}[7, 8, 9, 11]$
${}^2G_{-4}^\downarrow$	$\sqrt{\frac{2}{5}}[1, 2, 6, 11] + \sqrt{\frac{3}{5}}[2, 3, 4, 11]$
${}^2G_{-3}^\downarrow$	$\sqrt{\frac{3}{10}}[1, 2, 8, 11] + \sqrt{\frac{1}{20}}[2, 3, 6, 11] - \sqrt{\frac{9}{20}}[2, 4, 5, 11] + \sqrt{\frac{1}{5}}[1, 4, 6, 11]$
${}^2G_{-2}^\downarrow$	$\sqrt{\frac{3}{35}}[1, 2, 10, 11] - \sqrt{\frac{27}{140}}[2, 4, 7, 11] - \sqrt{\frac{3}{140}}[2, 3, 8, 11] + \sqrt{\frac{12}{35}}[2, 5, 6, 11] +$ $+\sqrt{\frac{12}{35}}[1, 4, 8, 11] + \sqrt{\frac{1}{70}}[3, 4, 6, 11]$
${}^2G_{-1}^\downarrow$	$-\sqrt{\frac{3}{70}}[2, 4, 9, 11] - \sqrt{\frac{3}{70}}[2, 3, 10, 11] - \sqrt{\frac{7}{20}}[2, 6, 7, 11] + \sqrt{\frac{9}{140}}[2, 5, 8, 11] +$ $+\sqrt{\frac{6}{35}}[1, 4, 10, 11] + \sqrt{\frac{4}{35}}[1, 6, 8, 11] + \sqrt{\frac{6}{35}}[3, 4, 8, 11] + \sqrt{\frac{3}{70}}[4, 5, 6, 11]$
${}^2G_0^\downarrow$	$-\sqrt{\frac{1}{7}}[2, 6, 9, 11] + \sqrt{\frac{3}{14}}[2, 7, 8, 11] + \sqrt{\frac{1}{7}}[1, 6, 10, 11] + \sqrt{\frac{3}{14}}[3, 4, 10, 11] +$ $-\sqrt{\frac{1}{7}}[4, 6, 7, 11] + \sqrt{\frac{1}{7}}[3, 6, 8, 11]$
${}^2G_1^\downarrow$	$\sqrt{\frac{3}{70}}[1, 8, 10, 11] + \sqrt{\frac{3}{70}}[2, 7, 10, 11] + \sqrt{\frac{7}{20}}[3, 6, 10, 11] - \sqrt{\frac{9}{140}}[4, 5, 10, 11] +$ $-\sqrt{\frac{6}{35}}[2, 8, 9, 11] - \sqrt{\frac{4}{35}}[4, 6, 9, 11] + \sqrt{\frac{6}{35}}[4, 7, 8, 11] + \sqrt{\frac{3}{70}}[5, 6, 8, 11]$
${}^2G_2^\downarrow$	$\sqrt{\frac{3}{35}}[2, 9, 10, 11] + \sqrt{\frac{27}{140}}[3, 8, 10, 11] + \sqrt{\frac{3}{140}}[4, 7, 10, 11] + \sqrt{\frac{12}{35}}[5, 6, 10, 11] +$ $-\sqrt{\frac{12}{35}}[4, 8, 9, 11] + \sqrt{\frac{1}{70}}[6, 7, 8, 11]$
${}^2G_3^\downarrow$	$\sqrt{\frac{3}{10}}[4, 9, 10, 11] - \sqrt{\frac{1}{20}}[6, 7, 10, 11] + \sqrt{\frac{9}{20}}[5, 8, 10, 11] - \sqrt{\frac{1}{5}}[6, 8, 9, 11]$
${}^2G_4^\downarrow$	$\sqrt{\frac{2}{5}}[6, 9, 10, 11] + \sqrt{\frac{3}{5}}[7, 8, 10, 11]$
${}^2H_{-5}^\uparrow$	$[1, 2, 3, 11]$
${}^2H_{-4}^\uparrow$	$\sqrt{\frac{3}{5}}[1, 2, 5, 11] - \sqrt{\frac{2}{5}}[1, 3, 4, 11]$
${}^2H_{-3}^\uparrow$	$\sqrt{\frac{1}{5}}[1, 2, 7, 11] + \sqrt{\frac{8}{15}}[1, 4, 5, 11] - \sqrt{\frac{2}{15}}[1, 3, 6, 11] - \sqrt{\frac{2}{15}}[2, 3, 5, 11]$
${}^2H_{-2}^\uparrow$	$\sqrt{\frac{1}{30}}[1, 2, 9, 11] - \sqrt{\frac{1}{30}}[1, 3, 8, 11] + \sqrt{\frac{3}{10}}[1, 4, 7, 11] - \sqrt{\frac{3}{10}}[1, 5, 6, 11] +$

Table A.2: Symmetry-adapted linear combinations of three-hole products

symmetry-adapted state	linear combination of simple products
${}^2\text{H}_{-1}^\uparrow$	$-\sqrt{\frac{2}{15}}[2, 3, 7, 11] + \sqrt{\frac{1}{5}}[3, 4, 5, 11]$
${}^2\text{H}_0^\uparrow$	$-\sqrt{\frac{1}{210}}[1, 3, 10, 11] + \sqrt{\frac{8}{105}}[1, 4, 9, 11] - \sqrt{\frac{4}{35}}[1, 5, 8, 11] + \sqrt{\frac{9}{35}}[1, 6, 7, 11] +$ $-\sqrt{\frac{3}{70}}[2, 3, 9, 11] - \sqrt{\frac{1}{35}}[2, 5, 7, 11] + \sqrt{\frac{32}{105}}[3, 4, 7, 11] - \sqrt{\frac{6}{35}}[3, 5, 6, 11]$
${}^2\text{H}_1^\uparrow$	$-\sqrt{\frac{1}{42}}[1, 5, 10, 11] + \sqrt{\frac{2}{21}}[1, 6, 9, 11] - \sqrt{\frac{1}{7}}[1, 7, 8, 11] - \sqrt{\frac{1}{42}}[2, 5, 9, 11] +$ $+\sqrt{\frac{1}{7}}[3, 4, 9, 11] - \sqrt{\frac{2}{21}}[3, 5, 8, 11] + \sqrt{\frac{8}{21}}[3, 6, 7, 11] - \sqrt{\frac{2}{21}}[4, 5, 7, 11]$
${}^2\text{H}_2^\uparrow$	$\sqrt{\frac{1}{210}}[2, 7, 9, 11] - \sqrt{\frac{8}{105}}[1, 8, 9, 11] + \sqrt{\frac{4}{35}}[4, 5, 9, 11] - \sqrt{\frac{9}{35}}[3, 6, 9, 11] +$ $+\sqrt{\frac{3}{70}}[1, 7, 10, 11] + \sqrt{\frac{1}{35}}[3, 5, 10, 11] + \sqrt{\frac{32}{105}}[3, 7, 8, 11] - \sqrt{\frac{6}{35}}[5, 6, 7, 11]$
${}^2\text{H}_3^\uparrow$	$\sqrt{\frac{1}{30}}[1, 9, 10, 11] + \sqrt{\frac{1}{30}}[4, 7, 9, 11] - \sqrt{\frac{3}{10}}[3, 8, 9, 11] - \sqrt{\frac{3}{10}}[5, 6, 9, 11] +$ $+\sqrt{\frac{2}{15}}[3, 7, 10, 11] + \sqrt{\frac{1}{5}}[5, 7, 8, 11]$
${}^2\text{H}_4^\uparrow$	$\sqrt{\frac{1}{5}}[3, 9, 10, 11] - \sqrt{\frac{8}{15}}[5, 8, 9, 11] + \sqrt{\frac{2}{15}}[6, 7, 9, 11] + \sqrt{\frac{2}{15}}[5, 7, 10, 11]$
${}^2\text{H}_5^\uparrow$	$\sqrt{\frac{3}{5}}[5, 9, 10, 11] - \sqrt{\frac{2}{5}}[7, 8, 9, 11]$
${}^2\text{H}_{-5}^\downarrow$	$[7, 9, 10, 11]$
${}^2\text{H}_{-4}^\downarrow$	$[1, 2, 4, 11]$
${}^2\text{H}_{-3}^\downarrow$	$-\sqrt{\frac{3}{5}}[1, 2, 6, 11] + \sqrt{\frac{2}{5}}[2, 3, 4, 11]$
${}^2\text{H}_{-2}^\downarrow$	$-\sqrt{\frac{1}{5}}[1, 2, 8, 11] + \sqrt{\frac{8}{15}}[2, 3, 6, 11] - \sqrt{\frac{2}{15}}[2, 4, 5, 11] - \sqrt{\frac{2}{15}}[1, 4, 6, 11]$
${}^2\text{H}_{-1}^\downarrow$	$-\sqrt{\frac{1}{30}}[1, 2, 10, 11] - \sqrt{\frac{1}{30}}[2, 4, 7, 11] + \sqrt{\frac{3}{10}}[2, 3, 8, 11] + \sqrt{\frac{3}{10}}[2, 5, 6, 11] +$ $-\sqrt{\frac{2}{15}}[1, 4, 8, 11] - \sqrt{\frac{1}{5}}[3, 4, 6, 11]$
${}^2\text{H}_0^\downarrow$	$-\sqrt{\frac{1}{210}}[2, 4, 9, 11] + \sqrt{\frac{8}{105}}[2, 3, 10, 11] - \sqrt{\frac{4}{35}}[2, 6, 7, 11] + \sqrt{\frac{9}{35}}[2, 5, 8, 11] +$ $-\sqrt{\frac{3}{70}}[1, 4, 10, 11] - \sqrt{\frac{1}{35}}[1, 6, 8, 11] - \sqrt{\frac{32}{105}}[3, 4, 8, 11] + \sqrt{\frac{6}{35}}[4, 5, 6, 11]$
${}^2\text{H}_1^\downarrow$	$-\sqrt{\frac{1}{42}}[2, 6, 9, 11] + \sqrt{\frac{2}{21}}[2, 5, 10, 11] + \sqrt{\frac{1}{7}}[2, 7, 8, 11] - \sqrt{\frac{1}{42}}[1, 6, 10, 11] +$ $-\sqrt{\frac{1}{7}}[3, 4, 10, 11] - \sqrt{\frac{2}{21}}[4, 6, 7, 11] + \sqrt{\frac{8}{21}}[4, 5, 8, 11] - \sqrt{\frac{2}{21}}[3, 6, 8, 11]$
${}^2\text{H}_2^\downarrow$	$\sqrt{\frac{1}{210}}[1, 8, 10, 11] - \sqrt{\frac{8}{105}}[2, 7, 10, 11] + \sqrt{\frac{4}{35}}[3, 6, 10, 11] - \sqrt{\frac{9}{35}}[4, 5, 10, 11] +$ $+\sqrt{\frac{3}{70}}[2, 8, 9, 11] + \sqrt{\frac{1}{35}}[4, 6, 9, 11] - \sqrt{\frac{32}{105}}[4, 7, 8, 11] + \sqrt{\frac{6}{35}}[5, 6, 8, 11]$
${}^2\text{H}_3^\downarrow$	$-\sqrt{\frac{1}{30}}[2, 9, 10, 11] + \sqrt{\frac{1}{30}}[3, 8, 10, 11] - \sqrt{\frac{3}{10}}[4, 7, 10, 11] + \sqrt{\frac{3}{10}}[5, 6, 10, 11] +$ $+\sqrt{\frac{2}{15}}[4, 8, 9, 11] - \sqrt{\frac{1}{5}}[6, 7, 8, 11]$
${}^2\text{H}_4^\downarrow$	$-\sqrt{\frac{1}{5}}[4, 9, 10, 11] - \sqrt{\frac{8}{15}}[6, 7, 10, 11] + \sqrt{\frac{2}{15}}[5, 8, 10, 11] + \sqrt{\frac{2}{15}}[6, 8, 9, 11]$
${}^2\text{H}_5^\downarrow$	$-\sqrt{\frac{3}{5}}[6, 9, 10, 11] + \sqrt{\frac{2}{5}}[7, 8, 10, 11]$
	$[8, 9, 10, 11]$

Table A.3: Symmetry-adapted linear combinations of three-hole products, produced by our orthogonalization procedure.

symmetry-adapted state	linear combination of simple products
${}^4P_{-1}^{\uparrow\uparrow\uparrow}$	$-\sqrt{\frac{3}{5}}[1, 3, 9, 11] + \sqrt{\frac{2}{5}}[1, 5, 7, 11]$
${}^4P_0^{\uparrow\uparrow\uparrow}$	$-\sqrt{\frac{1}{5}}[1, 5, 9, 11] + \sqrt{\frac{4}{5}}[3, 5, 7, 11]$
${}^4P_1^{\uparrow\uparrow\uparrow}$	$-\sqrt{\frac{3}{5}}[1, 7, 9, 11] + \sqrt{\frac{2}{5}}[3, 5, 9, 11]$
${}^4P_{-1}^{\uparrow\uparrow\downarrow}$	$0.365148 [1,6,7,11] -0.447213 [1,4,9,11] -0.447213 [2,3,9,11] +0.365148 [2,5,7,11] +$ $+0.365149 [1,5,8,11] -0.447214 [1,3,10,11]$
${}^4P_0^{\uparrow\uparrow\downarrow}$	$0.516397 [3,5,8,11] -0.258199 [1,6,9,11] +0.516398 [3,6,7,11] +0.516397 [4,5,7,11] +$ $-0.258199 [1,5,10,11] -0.258199 [2,5,9,11]$
${}^4P_1^{\uparrow\uparrow\downarrow}$	$-0.447213 [1,7,10,11] +0.365148 [3,5,10,11] -0.447213 [1,8,9,11] +0.365148 [3,6,9,11] +$ $+0.365149 [4,5,9,11] -0.447214 [2,7,9,11]$
${}^4P_{-1}^{\uparrow\downarrow\downarrow}$	$0.365148 [2,5,8,11] -0.447213 [2,3,10,11] -0.447213 [1,4,10,11] +0.365148 [1,6,8,11] +$ $+0.365148 [2,6,7,11] -0.447213 [2,4,9,11]$
${}^4P_0^{\uparrow\downarrow\downarrow}$	$0.516397 [4,6,7,11] -0.258199 [2,5,10,11] +0.516397 [4,5,8,11] +0.516397 [3,6,8,11] +$ $-0.258199 [2,6,9,11] -0.258199 [1,6,10,11]$
${}^4P_1^{\uparrow\downarrow\downarrow}$	$-0.447213 [2,8,9,11] +0.365148 [4,6,9,11] -0.447213 [2,7,10,11] +0.365148 [4,5,10,11] +$ $+0.365148 [3,6,10,11] -0.447213 [1,8,10,11]$
${}^4P_{-1}^{\downarrow\downarrow\downarrow}$	$-\sqrt{\frac{3}{5}}[2, 4, 10, 11] + \sqrt{\frac{2}{5}}[2, 6, 8, 11]$
${}^4P_0^{\downarrow\downarrow\downarrow}$	$-\sqrt{\frac{1}{5}}[2, 6, 10, 11] + \sqrt{\frac{4}{5}}[4, 6, 8, 11]$
${}^4P_1^{\downarrow\downarrow\downarrow}$	$-\sqrt{\frac{3}{5}}[2, 8, 10, 11] + \sqrt{\frac{2}{5}}[4, 6, 10, 11]$
${}^4F_{-3}^{\uparrow\uparrow\uparrow}$	$[1,3,5,11]$
${}^4F_{-2}^{\uparrow\uparrow\uparrow}$	$[1,3,7,11]$
${}^4F_{-1}^{\uparrow\uparrow\uparrow}$	$\sqrt{\frac{2}{5}}[1, 3, 9, 11] + \sqrt{\frac{3}{5}}[1, 5, 7, 11]$
${}^4F_0^{\uparrow\uparrow\uparrow}$	$-\sqrt{\frac{4}{5}}[1, 5, 9, 11] - \sqrt{\frac{1}{5}}[3, 5, 7, 11]$
${}^4F_1^{\uparrow\uparrow\uparrow}$	$-\sqrt{\frac{2}{5}}[1, 7, 9, 11] - \sqrt{\frac{3}{5}}[3, 5, 9, 11]$
${}^4F_2^{\uparrow\uparrow\uparrow}$	$-[3,7,9,11]$
${}^4F_3^{\uparrow\uparrow\uparrow}$	$[5,7,9,11]$
${}^4F_{-3}^{\uparrow\uparrow\downarrow}$	$\sqrt{\frac{1}{3}}[1, 4, 5, 11] + \sqrt{\frac{1}{3}}[1, 3, 6, 11] + \sqrt{\frac{1}{3}}[2, 3, 5, 11]$
${}^4F_{-2}^{\uparrow\uparrow\downarrow}$	$\sqrt{\frac{1}{3}}[1, 4, 7, 11] + \sqrt{\frac{1}{3}}[1, 3, 8, 11] + \sqrt{\frac{1}{3}}[2, 3, 7, 11]$
${}^4F_{-1}^{\uparrow\uparrow\downarrow}$	$0.365148 [1,4,9,11] +0.447213 [1,6,7,11] +0.447214 [1,5,8,11] +0.365148 [1,3,10,11] +$ $+0.365148 [2,3,9,11] +0.447214 [2,5,7,11]$
${}^4F_0^{\uparrow\uparrow\downarrow}$	$0.516398 [1,6,9,11] +0.516398 [2,5,9,11] +0.258199 [4,5,7,11] +0.516398 [1,5,10,11] +$ $+0.258199 [3,5,8,11] +0.258199 [3,6,7,11]$
${}^4F_1^{\uparrow\uparrow\downarrow}$	$-0.365148 [1,8,9,11] -0.447213 [3,6,9,11] -0.447214 [4,5,9,11] -0.365148 [2,7,9,11]$ $-0.365148 [1,7,10,11] -0.447214 [3,5,10,11]$
${}^4F_2^{\uparrow\uparrow\downarrow}$	$-\sqrt{\frac{1}{3}}[3, 8, 9, 11] - \sqrt{\frac{1}{3}}[4, 7, 9, 11] - \sqrt{\frac{1}{3}}[3, 7, 10, 11]$
${}^4F_3^{\uparrow\uparrow\downarrow}$	$-\sqrt{\frac{1}{3}}[5, 8, 9, 11] - \sqrt{\frac{1}{3}}[6, 7, 9, 11] - \sqrt{\frac{1}{3}}[5, 7, 10, 11]$

Table A.3: Symmetry-adapted linear combinations of three-hole products, produced by our orthogonalization procedure.

symmetry-adapted state	linear combination of simple products
${}^4F_{-3}^{\uparrow\downarrow\downarrow}$	$\sqrt{\frac{1}{3}}[2, 3, 6, 11] + \sqrt{\frac{1}{3}}[2, 4, 5, 11] + \sqrt{\frac{1}{3}}[1, 4, 6, 11]$
${}^4F_{-2}^{\uparrow\downarrow\downarrow}$	$\sqrt{\frac{1}{3}}[2, 3, 8, 11] + \sqrt{\frac{1}{3}}[2, 4, 7, 11] + \sqrt{\frac{1}{3}}[1, 4, 8, 11]$
${}^4F_{-1}^{\uparrow\downarrow\downarrow}$	$0.365148 [2,3,10,11] + 0.447213 [2,5,8,11] + 0.447213 [2,6,7,11] + 0.365148 [2,4,9,11] +$ $+ 0.365148 [1,4,10,11] + 0.447213 [1,6,8,11]$
${}^4F_0^{\uparrow\downarrow\downarrow}$	$0.516398 [2,5,10,11] + 0.516398 [1,6,10,11] + 0.258199 [3,6,8,11] + 0.516398 [2,6,9,11] +$ $+ 0.258199 [4,6,7,11] + 0.258199 [4,5,8,11]$
${}^4F_1^{\uparrow\downarrow\downarrow}$	$-0.365148 [2,7,10,11] - 0.447213 [4,5,10,11] - 0.447213 [3,6,10,11] - 0.365148 [1,8,10,11] +$ $- 0.365148 [2,8,9,11] - 0.447213 [4,6,9,11]$
${}^4F_2^{\uparrow\downarrow\downarrow}$	$-\sqrt{\frac{1}{3}}[4, 7, 10, 11] - \sqrt{\frac{1}{3}}[3, 8, 10, 11] - \sqrt{\frac{1}{3}}[4, 8, 9, 11]$
${}^4F_3^{\uparrow\downarrow\downarrow}$	$-\sqrt{\frac{1}{3}}[6, 7, 10, 11] - \sqrt{\frac{1}{3}}[5, 8, 10, 11] - \sqrt{\frac{1}{3}}[6, 8, 9, 11]$
${}^4F_{-3}^{\downarrow\downarrow\downarrow}$	$[2,4,6,11]$
${}^4F_{-2}^{\downarrow\downarrow\downarrow}$	$[2,4,8,11]$
${}^4F_{-1}^{\downarrow\downarrow\downarrow}$	$\sqrt{\frac{2}{5}}[2, 4, 10, 11] + \sqrt{\frac{3}{5}}[2, 6, 8, 11]$
${}^4F_0^{\downarrow\downarrow\downarrow}$	$-\sqrt{\frac{4}{5}}[2, 6, 10, 11] - \sqrt{\frac{1}{5}}[4, 6, 8, 11]$
${}^4F_1^{\downarrow\downarrow\downarrow}$	$-\sqrt{\frac{2}{5}}[2, 8, 10, 11] - \sqrt{\frac{3}{5}}[4, 6, 10, 11]$
${}^4F_2^{\downarrow\downarrow\downarrow}$	$-[4,8,10,11]$
${}^4F_3^{\downarrow\downarrow\downarrow}$	$[6,8,10,11]$

The other half of the symmetry-adapted three-hole states is obtained from the states depicted in Tables A.2 and A.3 by substituting the 4s hole [11] by the one of the opposite spin, i.e. [12].

Table A.4: Symmetry-adapted linear combinations of four-hole products, produced by our numerical procedure.

symmetry-adapted state	linear combination of simple products
${}^1S(1)$	$-0.316228 [1,3,8,10] + 0.316228 [1,5,6,10] + 0.316228 [1,4,7,10] - 0.316228 [1,2,9,10] +$ $-0.316228 [3,5,6,8] - 0.316228 [3,4,7,8] + 0.316228 [2,3,8,9] + 0.316228 [4,5,6,7] +$ $-0.316228 [2,5,6,9] - 0.316228 [2,4,7,9]$
${}^1S(2)$	$-0.207019 [1,5,6,10] - 0.338062 [1,6,7,8] - 0.338062 [3,4,5,10] + 0.069006 [3,4,7,8] +$ $+ 0.338062 [3,4,6,9] + 0.338062 [2,5,7,8] + 0.207019 [2,5,6,9] + 0.207019 [1,3,8,10] +$ $- 0.276026 [1,4,8,9] - 0.207020 [3,5,6,8] + 0.207020 [4,5,6,7] - 0.276026 [2,3,7,10] +$ $+ 0.207019 [2,4,7,9] + 0.069007 [1,4,7,10] - 0.345033 [1,2,9,10] + 0.069007 [2,3,8,9]$
${}^1D_{-2}(1)$	$-0.377964 [1,3,4,10] - 0.308607 [1,2,5,10] + 0.308607 [1,3,6,8] - 0.308607 [2,3,5,8] +$ $- 0.377964 [3,4,5,6] - 0.308607 [1,4,6,7] + 0.308607 [2,4,5,7] + 0.308607 [1,2,6,9] +$ $+ 0.377964 [2,3,4,9]$
${}^1D_{-1}(1)$	$-0.154303 [1,3,6,10] + 0.154303 [1,4,5,10] - 0.377964 [1,2,7,10] - 0.154303 [3,4,5,8] +$ $- 0.377964 [2,3,7,8] + 0.377964 [1,5,6,8] - 0.377964 [2,5,6,7] + 0.377964 [1,4,7,8] +$ $+ 0.154303 [3,4,6,7] + 0.377964 [1,2,8,9] + 0.154303 [2,3,6,9] - 0.154303 [2,4,5,9]$
${}^1D_0(1)$	$-0.154303 [1,3,8,10] + 0.154303 [1,4,7,10] - 0.617213 [1,2,9,10] + 0.462910 [3,5,6,8] +$ $+ 0.308607 [3,4,7,8] + 0.154303 [2,3,8,9] - 0.462910 [4,5,6,7] - 0.154303 [2,4,7,9]$
${}^1D_1(1)$	$-0.154303 [1,5,8,10] + 0.154303 [1,6,7,10] - 0.377964 [1,4,9,10] - 0.154303 [3,6,7,8] +$ $- 0.377964 [3,4,8,9] + 0.377964 [3,5,6,10] - 0.377964 [4,5,6,9] + 0.377964 [3,4,7,10] +$ $+ 0.154303 [4,5,7,8] + 0.377964 [2,3,9,10] + 0.154303 [2,5,8,9] - 0.154303 [2,6,7,9]$
${}^1D_2(1)$	$-0.377964 [1,7,8,10] - 0.308607 [1,6,9,10] + 0.308607 [3,5,8,10] - 0.308607 [3,6,8,9] +$ $- 0.377964 [5,6,7,8] - 0.308607 [4,5,7,10] + 0.308607 [4,6,7,9] + 0.308607 [2,5,9,10] +$ $+ 0.377964 [2,7,8,9]$
${}^1D_{-2}(2)$	$0.218218 [1,4,6,7] + 0.218218 [1,2,6,9] - 0.267261 [1,3,4,10] + 0.534522 [3,4,5,6] +$ $+ 0.267261 [2,3,4,9] - 0.218218 [1,2,5,10] + 0.218218 [2,3,5,8] - 0.218218 [1,4,5,8] +$ $+ 0.534523 [1,2,7,8] - 0.218218 [2,3,6,7]$
${}^1D_{-1}(2)$	$-0.327327 [1,3,6,10] + 0.267262 [1,5,6,8] + 0.436436 [1,4,6,9] + 0.218218 [3,4,5,8] +$ $- 0.218218 [3,4,6,7] + 0.436436 [2,3,5,10] - 0.267262 [2,5,6,7] - 0.327327 [2,4,5,9] +$ $- 0.267261 [1,2,8,9] - 0.109109 [2,3,6,9] - 0.109109 [1,4,5,10] + 0.267261 [1,2,7,10]$
${}^1D_0(2)$	$-0.267261 [1,6,7,8] - 0.267261 [3,4,5,10] + 0.436436 [3,4,7,8] + 0.267261 [3,4,6,9] +$ $+ 0.267261 [2,5,7,8] - 0.327327 [1,3,8,10] + 0.218218 [1,4,8,9] + 0.218218 [2,3,7,10] +$ $- 0.327327 [2,4,7,9] + 0.109109 [1,4,7,10] + 0.436436 [1,2,9,10] + 0.109109 [2,3,8,9]$
${}^1D_1(2)$	$-0.327327 [1,5,8,10] + 0.436436 [1,6,8,9] + 0.267262 [3,5,6,10] + 0.218218 [3,6,7,8] +$ $- 0.218218 [4,5,7,8] - 0.267262 [4,5,6,9] + 0.436436 [2,5,7,10] - 0.327327 [2,6,7,9] +$ $- 0.109109 [1,6,7,10] + 0.267261 [1,4,9,10] - 0.267261 [2,3,9,10] - 0.109109 [2,5,8,9]$
${}^1D_2(2)$	$-0.267261 [1,7,8,10] - 0.218218 [1,6,9,10] + 0.218218 [3,6,8,9] + 0.534522 [5,6,7,8] +$ $+ 0.218218 [4,5,7,10] + 0.218218 [2,5,9,10] + 0.267261 [2,7,8,9] - 0.218218 [3,6,7,10] +$ $+ 0.534523 [3,4,9,10] - 0.218218 [4,5,8,9]$

Table A.4: Symmetry-adapted linear combinations of four-hole products, produced by our numerical procedure.

symmetry-adapted state	linear combination of simple products
${}^1F_{-3}$	$0.273861 [1,4,5,6] + 0.223607 [1,2,6,7] + 0.273861 [1,3,4,8] - 0.273861 [2,3,4,7] +$ $-0.223607 [1,2,5,8] - 0.273861 [2,3,5,6] + 0.547723 [1,2,3,10] - 0.547723 [1,2,4,9]$
${}^1F_{-2}$	$0.273861 [1,3,6,8] - 0.091287 [1,4,6,7] - 0.365148 [1,2,6,9] - 0.223607 [1,3,4,10] +$ $+ 0.447214 [3,4,5,6] + 0.223607 [2,3,4,9] + 0.365148 [1,2,5,10] - 0.091287 [2,3,5,8] +$ $+ 0.273861 [2,4,5,7] - 0.182574 [1,4,5,8] - 0.447214 [1,2,7,8] - 0.182574 [2,3,6,7]$
${}^1F_{-1}$	$0.353553 [1,5,6,8] - 0.288675 [1,4,6,9] + 0.288675 [3,4,5,8] - 0.288675 [3,4,6,7] +$ $- 0.288675 [2,3,5,10] - 0.353553 [2,5,6,7] - 0.353553 [1,4,7,8] + 0.288675 [2,3,6,9] +$ $+ 0.288675 [1,4,5,10] + 0.353553 [2,3,7,8]$
1F_0	$-\frac{1}{2}[1,6,7,8] + \frac{1}{2}[3,4,5,10] - \frac{1}{2}[3,4,6,9] + \frac{1}{2}[2,5,7,8]$
1F_1	$-0.288675 [1,6,7,10] + 0.288675 [1,6,8,9] + 0.353553 [3,4,7,10] - 0.353553 [3,4,8,9] +$ $+ 0.288675 [2,5,7,10] - 0.288675 [2,5,8,9] - 0.353553 [3,5,6,10] - 0.288675 [3,6,7,8] +$ $+ 0.288675 [4,5,7,8] + 0.353553 [4,5,6,9]$
1F_2	$-0.365148 [1,6,9,10] + 0.447214 [3,4,9,10] + 0.365148 [2,5,9,10] + 0.223607 [1,7,8,10] +$ $+ 0.182574 [3,6,7,10] + 0.091287 [3,6,8,9] + 0.091287 [4,5,7,10] + 0.182574 [4,5,8,9] +$ $- 0.223607 [2,7,8,9] - 0.273861 [3,5,8,10] - 0.447214 [5,6,7,8] - 0.273861 [4,6,7,9]$
1F_3	$-0.547723 [1,8,9,10] + 0.223607 [3,6,9,10] - 0.223607 [4,5,9,10] + 0.547723 [2,7,9,10] +$ $- 0.273861 [3,7,8,10] - 0.273861 [5,6,7,10] + 0.273861 [5,6,8,9] + 0.273861 [4,7,8,9]$
${}^1G_{-4}(1)$	$-\sqrt{\frac{1}{3}}[1,2,3,8] + \sqrt{\frac{1}{3}}[1,2,5,6] + \sqrt{\frac{1}{3}}[1,2,4,7]$
${}^1G_{-3}(1)$	$-\sqrt{\frac{1}{6}}[1,2,3,10] + \sqrt{\frac{1}{6}}[1,3,4,8] + \sqrt{\frac{1}{6}}[1,4,5,6] - \sqrt{\frac{1}{6}}[2,3,5,6] +$ $-\sqrt{\frac{1}{6}}[2,3,4,7] + \sqrt{\frac{1}{6}}[1,2,4,9]$
${}^1G_{-2}(1)$	$0.436436 [1,3,4,10] - 0.267261 [1,2,5,10] + 0.267261 [1,3,6,8] - 0.267261 [2,3,5,8] +$ $+ 0.436436 [3,4,5,6] - 0.267261 [1,4,6,7] + 0.267261 [2,4,5,7] + 0.267261 [1,2,6,9] +$ $- 0.436436 [2,3,4,9]$
${}^1G_{-1}(1)$	$0.377964 [1,3,6,10] - 0.377964 [1,4,5,10] - 0.154303 [1,2,7,10] + 0.377964 [3,4,5,8] +$ $- 0.154303 [2,3,7,8] + 0.154303 [1,5,6,8] - 0.154303 [2,5,6,7] + 0.154303 [1,4,7,8] +$ $- 0.377964 [3,4,6,7] + 0.154303 [1,2,8,9] - 0.377964 [2,3,6,9] + 0.377964 [2,4,5,9]$
${}^1G_0(1)$	$0.207020 [1,3,8,10] + 0.483046 [1,5,6,10] - 0.207020 [1,4,7,10] - 0.138013 [1,2,9,10] +$ $- 0.138013 [3,5,6,8] + 0.552052 [3,4,7,8] - 0.207020 [2,3,8,9] + 0.138013 [4,5,6,7] +$ $- 0.483046 [2,5,6,9] + 0.207020 [2,4,7,9]$
${}^1G_1(1)$	$0.377964 [1,5,8,10] - 0.377964 [1,6,7,10] - 0.154303 [1,4,9,10] + 0.377964 [3,6,7,8] +$ $- 0.154303 [3,4,8,9] + 0.154303 [3,5,6,10] - 0.154303 [4,5,6,9] + 0.154303 [3,4,7,10] +$ $- 0.377964 [4,5,7,8] + 0.154303 [2,3,9,10] - 0.377964 [2,5,8,9] + 0.377964 [2,6,7,9]$
${}^1G_2(1)$	$0.436436 [1,7,8,10] - 0.267261 [1,6,9,10] + 0.267261 [3,5,8,10] - 0.267261 [3,6,8,9] +$ $+ 0.436436 [5,6,7,8] - 0.267261 [4,5,7,10] + 0.267261 [4,6,7,9] + 0.267261 [2,5,9,10] +$ $- 0.436436 [2,7,8,9]$
${}^1G_3(1)$	$-\sqrt{\frac{1}{6}}[1,8,9,10] + \sqrt{\frac{1}{6}}[3,7,8,10] + \sqrt{\frac{1}{6}}[5,6,7,10] - \sqrt{\frac{1}{6}}[5,6,8,9] +$ $-\sqrt{\frac{1}{6}}[4,7,8,9] + \sqrt{\frac{1}{6}}[2,7,9,10]$
${}^1G_4(1)$	$-\sqrt{\frac{1}{3}}[3,8,9,10] + \sqrt{\frac{1}{3}}[5,6,9,10] + \sqrt{\frac{1}{3}}[4,7,9,10]$

Table A.4: Symmetry-adapted linear combinations of four-hole products, produced by our numerical procedure.

symmetry-adapted state	linear combination of simple products
${}^1G_{-4}(2)$	$-0.639602 [1,3,4,6] -0.348156 [1,2,5,6] +0.639602 [2,3,4,5] -0.174078 [1,2,3,8] +$ $+0.174078 [1,2,4,7]$
${}^1G_{-3}(2)$	$0.307729 [1,4,5,6] +0.452267 [1,2,6,7] -0.430820 [1,3,4,8] +0.430820 [2,3,4,7] +$ $-0.452267 [1,2,5,8] -0.307729 [2,3,5,6] -0.123091 [1,2,3,10] +0.123091 [1,2,4,9]$
${}^1G_{-2}(2)$	$-0.282038 [1,3,6,8] +0.040292 [1,4,6,7] +0.322329 [1,2,6,9] -0.164487 [1,3,4,10] +$ $+0.328976 [3,4,5,6] +0.164487 [2,3,4,9] -0.322329 [1,2,5,10] +0.040292 [2,3,5,8] +$ $-0.282038 [2,4,5,7] +0.241747 [1,4,5,8] -0.592157 [1,2,7,8] +0.241747 [2,3,6,7]$
${}^1G_{-1}(2)$	$-0.227922 [1,3,6,10] -0.302408 [1,5,6,8] +0.170940 [1,4,6,9] +0.284901 [3,4,5,8] +$ $-0.284901 [3,4,6,7] +0.170940 [2,3,5,10] +0.302408 [2,5,6,7] -0.227922 [2,4,5,9] +$ $-0.162835 [1,4,7,8] +0.465242 [1,2,8,9] +0.056980 [2,3,6,9] +0.056980 [1,4,5,10] +$ $-0.465242 [1,2,7,10] +0.162835 [2,3,7,8]$
${}^1G_0(2)$	$-0.291287 [1,5,6,10] +0.076448 [1,6,7,8] +0.076448 [3,4,5,10] -0.076448 [3,4,6,9] +$ $-0.076448 [2,5,7,8] +0.291287 [2,5,6,9] -0.124837 [1,3,8,10] +0.374513 [1,4,8,9] +$ $-0.291288 [3,5,6,8] +0.291288 [4,5,6,7] +0.374513 [2,3,7,10] -0.124837 [2,4,7,9] +$ $-0.249675 [1,4,7,10] -0.416125 [1,2,9,10] -0.249675 [2,3,8,9] +0.166450 [3,4,7,8]$
${}^1G_1(2)$	$-0.227922 [1,5,8,10] +0.170940 [1,6,8,9] -0.302408 [3,5,6,10] +0.284901 [3,6,7,8] +$ $-0.284901 [4,5,7,8] +0.302408 [4,5,6,9] +0.170940 [2,5,7,10] -0.227922 [2,6,7,9] +$ $+0.056980 [1,6,7,10] -0.465242 [1,4,9,10] +0.162835 [3,4,8,9] -0.162835 [3,4,7,10] +$ $+0.465242 [2,3,9,10] +0.056980 [2,5,8,9]$
${}^1G_2(2)$	$-0.164487 [1,7,8,10] -0.322329 [1,6,9,10] -0.282038 [3,5,8,10] +0.040292 [3,6,8,9] +$ $+0.328976 [5,6,7,8] +0.040292 [4,5,7,10] -0.282038 [4,6,7,9] +0.322329 [2,5,9,10] +$ $+0.164487 [2,7,8,9] +0.241747 [3,6,7,10] -0.592157 [3,4,9,10] +0.241747 [4,5,8,9]$
${}^1G_3(2)$	$-0.430820 [3,7,8,10] -0.452267 [3,6,9,10] -0.307729 [5,6,8,9] +0.307729 [5,6,7,10] +$ $+0.452267 [4,5,9,10] +0.430820 [4,7,8,9] -0.123091 [1,8,9,10] +0.123091 [2,7,9,10]$
${}^1G_4(2)$	$-0.639602 [5,7,8,10] -0.348156 [5,6,9,10] +0.639602 [6,7,8,9] -0.174078 [3,8,9,10] +$ $+0.174078 [4,7,9,10]$
${}^1I_{-6}$	$[1,2,3,4]$
${}^1I_{-5}$	$\sqrt{\frac{1}{2}}[1,2,3,6] - \sqrt{\frac{1}{2}}[1,2,4,5]$
${}^1I_{-4}$	$0.369274 [1,2,3,8] +0.738549 [1,2,5,6] -0.369274 [1,2,4,7] -0.301511 [1,3,4,6] +$ $+0.301511 [2,3,4,5]$
${}^1I_{-3}$	$0.134840 [1,2,3,10] +0.495434 [1,2,5,8] -0.495434 [1,2,6,7] -0.134840 [1,2,4,9] +$ $-0.269680 [1,3,4,8] +0.404520 [1,4,5,6] -0.404520 [2,3,5,6] +0.269680 [2,3,4,7]$
${}^1I_{-2}$	$0.220193 [1,2,5,10] +0.404520 [1,2,7,8] -0.220193 [1,2,6,9] -0.134840 [1,3,4,10] +$ $+0.440386 [1,4,5,8] -0.330289 [1,4,6,7] -0.330289 [2,3,5,8] +0.440386 [2,3,6,7] +$ $+0.134840 [2,3,4,9] -0.110096 [1,3,6,8] +0.269680 [3,4,5,6] -0.110096 [2,4,5,7]$
${}^1I_{-1}$	$0.213201 [1,2,7,10] -0.213201 [1,2,8,9] +0.261116 [1,4,5,10] +0.426401 [1,4,7,8] +$ $-0.174078 [1,4,6,9] -0.174078 [2,3,5,10] -0.426401 [2,3,7,8] +0.261116 [2,3,6,9] +$ $-0.087039 [1,3,6,10] -0.213201 [1,5,6,8] +0.348155 [3,4,5,8] -0.348155 [3,4,6,7] +$ $+0.213201 [2,5,6,7] -0.087039 [2,4,5,9]$
1I_0	$0.131590 [1,2,9,10] +0.296078 [1,4,7,10] -0.263181 [1,4,8,9] -0.263181 [2,3,7,10] +$ $+0.296078 [2,3,8,9] -0.197386 [1,5,6,10] +0.241747 [1,6,7,8] +0.241747 [3,4,5,10] +$ $+0.526361 [3,4,7,8] -0.241747 [3,4,6,9] -0.241747 [2,5,7,8] +0.197386 [2,5,6,9] +$ $-0.032898 [1,3,8,10] -0.197386 [3,5,6,8] +0.197386 [4,5,6,7] -0.032898 [2,4,7,9]$

Table A.4: Symmetry-adapted linear combinations of four-hole products, produced by our numerical procedure.

symmetry-adapted state	linear combination of simple products
1I_1	0.213201 [1,4,9,10] -0.213201 [2,3,9,10] +0.261116 [1,6,7,10] -0.174078 [1,6,8,9] + +0.426401 [3,4,7,10] -0.426401 [3,4,8,9] -0.174078 [2,5,7,10] +0.261116 [2,5,8,9] + -0.087039 [1,5,8,10] -0.213201 [3,5,6,10] +0.348155 [3,6,7,8] -0.348155 [4,5,7,8] + +0.213201 [4,5,6,9] -0.087039 [2,6,7,9]
1I_2	0.220193 [1,6,9,10] +0.404520 [3,4,9,10] -0.220193 [2,5,9,10] -0.134840 [1,7,8,10] + +0.440386 [3,6,7,10] -0.330289 [3,6,8,9] -0.330289 [4,5,7,10] +0.440386 [4,5,8,9] + +0.134840 [2,7,8,9] -0.110096 [3,5,8,10] +0.269680 [5,6,7,8] -0.110096 [4,6,7,9]
1I_3	0.134840 [1,8,9,10] +0.495434 [3,6,9,10] -0.495434 [4,5,9,10] -0.134840 [2,7,9,10] + -0.269680 [3,7,8,10] +0.404520 [5,6,7,10] -0.404520 [5,6,8,9] +0.269680 [4,7,8,9]
1I_4	0.369274 [3,8,9,10] +0.738549 [5,6,9,10] -0.369274 [4,7,9,10] -0.301511 [5,7,8,10] + +0.301511 [6,7,8,9]
1I_5	$\sqrt{\frac{1}{2}}[5, 8, 9, 10] - \sqrt{\frac{1}{2}}[6, 7, 9, 10]$
1I_6	[7,8,9,10]
${}^3P_{-1}^{\uparrow\uparrow}(1)$	-0.365148 [1,2,8,10] +0.447214 [1,4,6,10] -0.447214 [3,4,6,8] -0.365148 [2,5,6,8] + -0.365148 [2,4,7,8] -0.447214 [2,4,6,9]
${}^3P_0^{\uparrow\uparrow}(1)$	0.258199 [1,4,8,10] +0.516398 [2,3,8,10] -0.516398 [2,5,6,10] +0.258199 [4,5,6,8] + -0.516398 [2,4,7,10] -0.258199 [2,4,8,9]
${}^3P_1^{\uparrow\uparrow}(1)$	0.447214 [1,6,8,10] -0.365148 [3,4,8,10] -0.365148 [4,5,6,10] -0.447214 [4,6,7,8] + -0.365148 [2,4,9,10] -0.447214 [2,6,8,9]
${}^3P_{-1}^{\uparrow\downarrow}(1)$	0.316228 [1,3,6,10] +0.316228 [1,4,5,10] -0.258199 [1,2,7,10] -0.316228 [3,4,5,8] + -0.258199 [2,3,7,8] -0.258199 [1,5,6,8] -0.258199 [2,5,6,7] -0.258199 [1,4,7,8] + -0.316228 [3,4,6,7] -0.258199 [1,2,8,9] -0.316228 [2,3,6,9] -0.316228 [2,4,5,9]
${}^3P_0^{\uparrow\downarrow}(1)$	0.547723 [1,3,8,10] -0.365148 [1,5,6,10] -0.182574 [1,4,7,10] +0.182574 [3,5,6,8] + +0.182574 [2,3,8,9] +0.182574 [4,5,6,7] -0.365148 [2,5,6,9] -0.547723 [2,4,7,9]
${}^3P_1^{\uparrow\downarrow}(1)$	0.316228 [1,5,8,10] +0.316228 [1,6,7,10] -0.258199 [1,4,9,10] -0.316228 [3,6,7,8] + -0.258199 [3,4,8,9] -0.258199 [3,5,6,10] -0.258199 [4,5,6,9] -0.258199 [3,4,7,10] + -0.316228 [4,5,7,8] -0.258199 [2,3,9,10] -0.316228 [2,5,8,9] -0.316228 [2,6,7,9]
${}^3P_{-1}^{\downarrow\downarrow}(1)$	0.447214 [1,3,5,10] -0.365148 [1,3,7,8] -0.365148 [1,5,6,7] -0.447214 [3,4,5,7] + -0.365148 [1,2,7,9] -0.447214 [2,3,5,9]
${}^3P_0^{\downarrow\downarrow}(1)$	0.258199 [1,3,7,10] +0.516398 [1,3,8,9] -0.516398 [1,5,6,9] +0.258199 [3,5,6,7] + -0.516398 [1,4,7,9] -0.258199 [2,3,7,9]
${}^3P_1^{\downarrow\downarrow}(1)$	-0.365148 [1,3,9,10] +0.447214 [1,5,7,10] -0.447214 [3,5,7,8] -0.365148 [3,5,6,9] + -0.365148 [3,4,7,9] -0.447214 [2,5,7,9]
${}^3P_{-1}^{\uparrow\uparrow}(2)$	0.239046 [1,4,6,10] -0.239046 [3,4,6,8] -0.358569 [2,4,5,10] +0.097590 [2,5,6,8] + -0.487949 [1,2,8,10] -0.358569 [2,3,6,10] +0.390360 [2,4,7,8] +0.478092 [2,4,6,9]
${}^3P_0^{\uparrow\uparrow}(2)$	-0.276026 [1,4,8,10] +0.507093 [3,4,6,10] +0.552052 [4,5,6,8] -0.069006 [2,4,7,10] + +0.507093 [2,6,7,8] +0.069006 [2,3,8,10] +0.138014 [2,5,6,10] +0.276026 [2,4,8,9]
${}^3P_1^{\uparrow\uparrow}(2)$	-0.478092 [1,6,8,10] +0.390360 [3,4,8,10] +0.097590 [4,5,6,10] -0.239046 [4,6,7,8] + -0.487949 [2,4,9,10] -0.239046 [2,6,8,9] +0.358569 [2,5,8,10] +0.358569 [2,6,7,10]

Table A.4: Symmetry-adapted linear combinations of four-hole products, produced by our numerical procedure.

symmetry-adapted state	linear combination of simple products
${}^3P_{-1}^{\uparrow\downarrow}(2)$	-0.084516 [1,3,6,10] +0.069007 [1,5,6,8] +0.507093 [1,4,6,9] -0.169030 [3,4,5,8] + -0.169030 [3,4,6,7] -0.507093 [2,3,5,10] +0.069007 [2,5,6,7] +0.084516 [2,4,5,9] + +0.276027 [1,4,7,8] -0.345032 [1,2,8,9] +0.084516 [2,3,6,9] -0.084516 [1,4,5,10] + -0.345032 [1,2,7,10] +0.276027 [2,3,7,8]
${}^3P_0^{\uparrow\downarrow}(2)$	-0.146386 [1,3,8,10] +0.358568 [1,6,7,8] +0.390361 [3,5,6,8] +0.358568 [3,4,6,9] + +0.358568 [3,4,5,10] +0.390361 [4,5,6,7] +0.358568 [2,5,7,8] +0.146386 [2,4,7,9] + +0.097589 [1,5,6,10] -0.243975 [1,4,7,10] +0.243975 [2,3,8,9] +0.097589 [2,5,6,9]
${}^3P_1^{\uparrow\downarrow}(2)$	-0.084516 [1,5,8,10] -0.084516 [1,6,7,10] -0.345032 [1,4,9,10] -0.169030 [3,6,7,8] + +0.276027 [3,4,8,9] +0.069007 [3,5,6,10] +0.069007 [4,5,6,9] +0.276027 [3,4,7,10] + -0.169030 [4,5,7,8] -0.345032 [2,3,9,10] +0.084516 [2,5,8,9] +0.084516 [2,6,7,9] + +0.507093 [2,5,7,10] -0.507093 [1,6,8,9]
${}^3P_{-1}^{\downarrow\downarrow}(2)$	0.358569 [1,3,6,9] +0.097590 [1,5,6,7] -0.239046 [3,4,5,7] -0.239046 [2,3,5,9] + +0.390360 [1,3,7,8] +0.358569 [1,4,5,9] -0.487949 [1,2,7,9] -0.478092 [1,3,5,10]
${}^3P_0^{\downarrow\downarrow}(2)$	0.069006 [1,3,8,9] +0.507093 [1,5,7,8] +0.552052 [3,5,6,7] +0.507093 [3,4,5,9] + +0.276026 [2,3,7,9] -0.276026 [1,3,7,10] +0.138014 [1,5,6,9] -0.069006 [1,4,7,9]
${}^3P_1^{\downarrow\downarrow}(2)$	-0.487949 [1,3,9,10] +0.239046 [1,5,7,10] -0.239046 [3,5,7,8] +0.097590 [3,5,6,9] + +0.390360 [3,4,7,9] +0.478092 [2,5,7,9] -0.358569 [1,5,8,9] -0.358569 [1,6,7,9]
${}^3D_{-2}^{\uparrow\uparrow}$	0.436436 [1,2,6,10] -0.545545 [1,4,6,8] +0.534522 [2,3,4,10] +0.327327 [2,4,5,8] + -0.109109 [2,3,6,8] +0.327327 [2,4,6,7]
${}^3D_{-1}^{\uparrow\uparrow}$	-0.109109 [1,4,6,10] -0.436436 [3,4,6,8] -0.327327 [2,4,5,10] -0.534522 [2,5,6,8] + +0.534522 [1,2,8,10] +0.109109 [2,3,6,10] +0.327327 [2,4,6,9]
${}^3D_0^{\uparrow\uparrow}$	-0.534522 [3,4,6,10] +0.327327 [1,4,8,10] -0.327327 [2,4,7,10] +0.534522 [2,6,7,8] + -0.327327 [2,3,8,10] +0.327327 [2,4,8,9]
${}^3D_1^{\uparrow\uparrow}$	0.327327 [1,6,8,10] -0.327327 [2,5,8,10] +0.534522 [4,5,6,10] +0.109109 [2,6,7,10] + +0.436436 [4,6,7,8] -0.534522 [2,4,9,10] -0.109109 [2,6,8,9]
${}^3D_2^{\uparrow\uparrow}$	0.327327 [3,6,8,10] +0.327327 [4,5,8,10] -0.534522 [2,7,8,10] -0.109109 [4,6,7,10] + -0.436436 [2,6,9,10] -0.545545 [4,6,8,9]
${}^3D_{-2}^{\uparrow\downarrow}$	-0.462910 [1,3,6,8] -0.154303 [1,4,6,7] +0.308607 [1,2,6,9] +0.377964 [1,3,4,10] + +0.377964 [2,3,4,9] +0.308607 [1,2,5,10] +0.154303 [2,3,5,8] +0.462910 [2,4,5,7] + -0.154303 [1,4,5,8] +0.154303 [2,3,6,7]
${}^3D_{-1}^{\uparrow\downarrow}$	-0.377964 [1,5,6,8] +0.154303 [1,4,6,9] -0.308607 [3,4,5,8] -0.308607 [3,4,6,7] + -0.154303 [2,3,5,10] -0.377964 [2,5,6,7] +0.377964 [1,2,8,9] +0.308607 [2,3,6,9] + -0.308607 [1,4,5,10] +0.377964 [1,2,7,10]
${}^3D_0^{\uparrow\downarrow}$	0.377964 [1,6,7,8] -0.377964 [3,4,5,10] -0.377964 [3,4,6,9] +0.377964 [2,5,7,8] + +0.462910 [1,4,8,9] -0.462910 [2,3,7,10]
${}^3D_1^{\uparrow\downarrow}$	0.308607 [1,6,7,10] +0.154303 [1,6,8,9] -0.154303 [2,5,7,10] -0.308607 [2,5,8,9] + +0.377964 [3,5,6,10] +0.308607 [3,6,7,8] +0.308607 [4,5,7,8] +0.377964 [4,5,6,9] + -0.377964 [1,4,9,10] -0.377964 [2,3,9,10]
${}^3D_2^{\uparrow\downarrow}$	-0.377964 [1,7,8,10] +0.154303 [3,6,7,10] -0.154303 [3,6,8,9] +0.154303 [4,5,7,10] + -0.154303 [4,5,8,9] -0.377964 [2,7,8,9] -0.308607 [1,6,9,10] +0.462910 [3,5,8,10] + -0.462910 [4,6,7,9] -0.308607 [2,5,9,10]
${}^3D_{-2}^{\downarrow\downarrow}$	-0.327327 [1,3,6,7] +0.534522 [1,3,4,9] +0.436436 [1,2,5,9] +0.545545 [2,3,5,7] + -0.327327 [1,3,5,8] +0.109109 [1,4,5,7]
${}^3D_{-1}^{\downarrow\downarrow}$	0.327327 [1,3,6,9] -0.534522 [1,5,6,7] -0.436436 [3,4,5,7] +0.109109 [2,3,5,9] + -0.109109 [1,4,5,9] +0.534522 [1,2,7,9] -0.327327 [1,3,5,10]

Table A.4: Symmetry-adapted linear combinations of four-hole products, produced by our numerical procedure.

symmetry-adapted state	linear combination of simple products
${}^3D_0^{\downarrow\downarrow}$	$-0.534522 [3,4,5,9] + 0.327327 [1,3,8,9] + 0.534522 [1,5,7,8] - 0.327327 [2,3,7,9] +$ $-0.327327 [1,3,7,10] + 0.327327 [1,4,7,9]$
${}^3D_1^{\downarrow\downarrow}$	$0.327327 [1,6,7,9] - 0.327327 [2,5,7,9] - 0.109109 [1,5,8,9] + 0.534522 [3,5,6,9] +$ $-0.534522 [1,3,9,10] + 0.109109 [1,5,7,10] + 0.436436 [3,5,7,8]$
${}^3D_2^{\downarrow\downarrow}$	$-0.534522 [1,7,8,9] - 0.327327 [3,6,7,9] - 0.327327 [4,5,7,9] - 0.436436 [1,5,9,10] +$ $+0.109109 [3,5,8,9] + 0.545545 [3,5,7,10]$
${}^3F_{-3}^{\uparrow\uparrow}(1)$	$-\sqrt{\frac{1}{3}}[1, 2, 4, 10] - \sqrt{\frac{1}{3}}[2, 3, 4, 8] - \sqrt{\frac{1}{3}}[2, 4, 5, 6]$
${}^3F_{-2}^{\uparrow\uparrow}(1)$	$-\sqrt{\frac{1}{3}}[1, 2, 6, 10] - \sqrt{\frac{1}{3}}[2, 3, 6, 8] + \sqrt{\frac{1}{3}}[2, 4, 6, 7]$
${}^3F_{-1}^{\uparrow\uparrow}(1)$	$-0.447214 [1,2,8,10] - 0.365148 [1,4,6,10] + 0.365148 [3,4,6,8] - 0.447214 [2,5,6,8] +$ $-0.447214 [2,4,7,8] + 0.365148 [2,4,6,9]$
${}^3F_0^{\uparrow\uparrow}(1)$	$-0.516398 [1,4,8,10] + 0.258199 [2,3,8,10] - 0.258199 [2,5,6,10] - 0.516398 [4,5,6,8] +$ $-0.258199 [2,4,7,10] + 0.516398 [2,4,8,9]$
${}^3F_1^{\uparrow\uparrow}(1)$	$-0.365148 [1,6,8,10] - 0.447214 [3,4,8,10] - 0.447214 [4,5,6,10] + 0.365148 [4,6,7,8] +$ $-0.447214 [2,4,9,10] + 0.365148 [2,6,8,9]$
${}^3F_2^{\uparrow\uparrow}(1)$	$-\sqrt{\frac{1}{3}}[3, 6, 8, 10] + \sqrt{\frac{1}{3}}[4, 6, 7, 10] - \sqrt{\frac{1}{3}}[2, 6, 9, 10]$
${}^3F_3^{\uparrow\uparrow}(1)$	$-\sqrt{\frac{1}{3}}[5, 6, 8, 10] - \sqrt{\frac{1}{3}}[4, 7, 8, 10] - \sqrt{\frac{1}{3}}[2, 8, 9, 10]$
${}^3F_{-3}^{\uparrow\downarrow}(1)$	$-\sqrt{\frac{1}{6}}[1, 2, 3, 10] - \sqrt{\frac{1}{6}}[1, 3, 4, 8] - \sqrt{\frac{1}{6}}[1, 4, 5, 6] - \sqrt{\frac{1}{6}}[2, 3, 5, 6] +$ $-\sqrt{\frac{1}{6}}[2, 3, 4, 7] - \sqrt{\frac{1}{6}}[1, 2, 4, 9]$
${}^3F_{-2}^{\uparrow\downarrow}(1)$	$-\sqrt{\frac{1}{6}}[1, 2, 5, 10] - \sqrt{\frac{1}{6}}[1, 3, 6, 8] - \sqrt{\frac{1}{6}}[2, 3, 5, 8] + \sqrt{\frac{1}{6}}[1, 4, 6, 7] +$ $+\sqrt{\frac{1}{6}}[2, 4, 5, 7] - \sqrt{\frac{1}{6}}[1, 2, 6, 9]$
${}^3F_{-1}^{\uparrow\downarrow}(1)$	$-0.258199 [1,3,6,10] - 0.258199 [1,4,5,10] - 0.316228 [1,2,7,10] + 0.258199 [3,4,5,8] +$ $-0.316228 [2,3,7,8] - 0.316228 [1,5,6,8] - 0.316228 [2,5,6,7] - 0.316228 [1,4,7,8] +$ $+0.258199 [3,4,6,7] - 0.316228 [1,2,8,9] + 0.258199 [2,3,6,9] + 0.258199 [2,4,5,9]$
${}^3F_0^{\uparrow\downarrow}(1)$	$-0.182574 [1,3,8,10] - 0.182574 [1,5,6,10] - 0.547723 [1,4,7,10] - 0.365148 [3,5,6,8] +$ $+0.547723 [2,3,8,9] - 0.365148 [4,5,6,7] - 0.182574 [2,5,6,9] + 0.182574 [2,4,7,9]$
${}^3F_1^{\uparrow\downarrow}(1)$	$-0.258199 [1,5,8,10] - 0.258199 [1,6,7,10] - 0.316228 [1,4,9,10] + 0.258199 [3,6,7,8] +$ $-0.316228 [3,4,8,9] - 0.316228 [3,5,6,10] - 0.316228 [4,5,6,9] - 0.316228 [3,4,7,10] +$ $+0.258199 [4,5,7,8] - 0.316228 [2,3,9,10] + 0.258199 [2,5,8,9] + 0.258199 [2,6,7,9]$
${}^3F_2^{\uparrow\downarrow}(1)$	$-\sqrt{\frac{1}{6}}[1, 6, 9, 10] - \sqrt{\frac{1}{6}}[3, 5, 8, 10] - \sqrt{\frac{1}{6}}[3, 6, 8, 9] + \sqrt{\frac{1}{6}}[4, 5, 7, 10] +$ $+\sqrt{\frac{1}{6}}[4, 6, 7, 9] - \sqrt{\frac{1}{6}}[2, 5, 9, 10]$
${}^3F_3^{\uparrow\downarrow}(1)$	$-\sqrt{\frac{1}{6}}[1, 8, 9, 10] - \sqrt{\frac{1}{6}}[3, 7, 8, 10] - \sqrt{\frac{1}{6}}[5, 6, 7, 10] - \sqrt{\frac{1}{6}}[5, 6, 8, 9] +$ $-\sqrt{\frac{1}{6}}[4, 7, 8, 9] - \sqrt{\frac{1}{6}}[2, 7, 9, 10]$
${}^3F_{-3}^{\downarrow\downarrow}(1)$	$-\sqrt{\frac{1}{3}}[1, 3, 5, 6] - \sqrt{\frac{1}{3}}[1, 3, 4, 7] - \sqrt{\frac{1}{3}}[1, 2, 3, 9]$
${}^3F_{-2}^{\downarrow\downarrow}(1)$	$-\sqrt{\frac{1}{3}}[1, 3, 5, 8] + \sqrt{\frac{1}{3}}[1, 4, 5, 7] - \sqrt{\frac{1}{3}}[1, 2, 5, 9]$
${}^3F_{-1}^{\downarrow\downarrow}(1)$	$-0.365148 [1,3,5,10] - 0.447214 [1,3,7,8] - 0.447214 [1,5,6,7] + 0.365148 [3,4,5,7] +$ $-0.447214 [1,2,7,9] + 0.365148 [2,3,5,9]$
${}^3F_0^{\downarrow\downarrow}(1)$	$-0.516398 [1,3,7,10] + 0.258199 [1,3,8,9] - 0.258199 [1,5,6,9] - 0.516398 [3,5,6,7] +$ $-0.258199 [1,4,7,9] + 0.516398 [2,3,7,9]$

Table A.4: Symmetry-adapted linear combinations of four-hole products, produced by our numerical procedure.

symmetry-adapted state	linear combination of simple products
${}^3F_1^{\downarrow\downarrow}(1)$	$-0.447214 [1,3,9,10] -0.365148 [1,5,7,10] +0.365148 [3,5,7,8] -0.447214 [3,5,6,9] +$ $-0.447214 [3,4,7,9] +0.365148 [2,5,7,9]$
${}^3F_2^{\downarrow\downarrow}(1)$	$-\sqrt{\frac{1}{3}}[1, 5, 9, 10] - \sqrt{\frac{1}{3}}[3, 5, 8, 9] + \sqrt{\frac{1}{3}}[4, 5, 7, 9]$
${}^3F_3^{\downarrow\downarrow}(1)$	$-\sqrt{\frac{1}{3}}[1, 7, 9, 10] - \sqrt{\frac{1}{3}}[3, 7, 8, 9] - \sqrt{\frac{1}{3}}[5, 6, 7, 9]$
${}^3F_{-3}^{\uparrow\uparrow}(2)$	$0.707107 [1,2,6,8] +0.288676 [2,3,4,8] +0.288676 [2,4,5,6] -0.577350 [1,2,4,10]$
${}^3F_{-2}^{\uparrow\uparrow}(2)$	$0.577350 [1,4,6,8] +0.707107 [2,3,4,10] -0.288674 [2,3,6,8] -0.288676 [2,4,6,7]$
${}^3F_{-1}^{\uparrow\uparrow}(2)$	$0.365149 [1,4,6,10] +0.547722 [3,4,6,8] -0.547722 [2,4,5,10] -0.223607 [2,5,6,8] +$ $+0.365149 [2,3,6,10] +0.223607 [2,4,7,8] -0.182574 [2,4,6,9]$
${}^3F_0^{\uparrow\uparrow}(2)$	$0.258198 [1,4,8,10] +0.316228 [3,4,6,10] +0.316228 [2,6,7,8] +0.516398 [2,5,6,10] +$ $-0.258198 [2,4,8,9] +0.258199 [2,3,8,10] -0.516398 [4,5,6,8] -0.258199 [2,4,7,10]$
${}^3F_1^{\uparrow\uparrow}(2)$	$0.182574 [1,6,8,10] +0.223607 [3,4,8,10] -0.223607 [4,5,6,10] +0.547722 [4,6,7,8] +$ $-0.365149 [2,6,8,9] +0.547722 [2,5,8,10] -0.365149 [2,6,7,10]$
${}^3F_2^{\uparrow\uparrow}(2)$	$0.288676 [3,6,8,10] +0.288674 [4,6,7,10] -0.577350 [4,6,8,9] +0.707107 [2,7,8,10]$
${}^3F_3^{\uparrow\uparrow}(2)$	$0.288676 [5,6,8,10] +0.288676 [4,7,8,10] +0.707107 [4,6,9,10] -0.577350 [2,8,9,10]$
${}^3F_{-3}^{\uparrow\downarrow}(2)$	$0.204125 [1,4,5,6] +0.500000 [1,2,6,7] +0.204125 [1,3,4,8] +0.204125 [2,3,4,7] +$ $+0.500000 [1,2,5,8] +0.204125 [2,3,5,6] -0.408248 [1,2,3,10] -0.408248 [1,2,4,9]$
${}^3F_{-2}^{\uparrow\downarrow}(2)$	$0.204125 [1,3,6,8] +0.204123 [1,4,6,7] +0.500000 [1,3,4,10] +0.500000 [2,3,4,9] +$ $-0.204123 [2,3,5,8] -0.204125 [2,4,5,7] +0.408248 [1,4,5,8] -0.408248 [2,3,6,7]$
${}^3F_{-1}^{\uparrow\downarrow}(2)$	$0.516398 [1,3,6,10] -0.158115 [1,5,6,8] +0.129099 [1,4,6,9] +0.387298 [3,4,5,8] +$ $+0.387298 [3,4,6,7] -0.129099 [2,3,5,10] -0.158115 [2,5,6,7] -0.516398 [2,4,5,9] +$ $+0.158113 [1,4,7,8] +0.129100 [2,3,6,9] -0.129100 [1,4,5,10] +0.158113 [2,3,7,8]$
${}^3F_0^{\uparrow\downarrow}(2)$	$0.365148 [1,3,8,10] +0.223607 [1,6,7,8] +0.223607 [3,4,6,9] +0.223607 [3,4,5,10] +$ $+0.223607 [2,5,7,8] -0.365148 [2,4,7,9] +0.365148 [1,5,6,10] +0.365148 [2,5,6,9] +$ $-0.365148 [3,5,6,8] -0.365148 [4,5,6,7]$
${}^3F_1^{\uparrow\downarrow}(2)$	$0.516398 [1,5,8,10] -0.129100 [1,6,7,10] +0.387298 [3,6,7,8] +0.158113 [3,4,8,9] +$ $-0.158115 [3,5,6,10] -0.158115 [4,5,6,9] +0.158113 [3,4,7,10] +0.387298 [4,5,7,8] +$ $+0.129100 [2,5,8,9] -0.516398 [2,6,7,9] +0.129099 [2,5,7,10] -0.129099 [1,6,8,9]$
${}^3F_2^{\uparrow\downarrow}(2)$	$0.204125 [3,5,8,10] +0.408248 [3,6,7,10] -0.408248 [4,5,8,9] -0.204125 [4,6,7,9] +$ $+0.204123 [4,5,7,10] +0.500000 [1,7,8,10] +0.500000 [2,7,8,9] -0.204123 [3,6,8,9]$
${}^3F_3^{\uparrow\downarrow}(2)$	$0.204125 [5,6,7,10] +0.500000 [4,5,9,10] +0.204125 [3,7,8,10] +0.204125 [4,7,8,9] +$ $+0.500000 [3,6,9,10] +0.204125 [5,6,8,9] -0.408248 [1,8,9,10] -0.408248 [2,7,9,10]$
${}^3F_{-3}^{\downarrow\downarrow}(2)$	$0.288676 [1,3,5,6] +0.288676 [1,3,4,7] +0.707107 [1,2,5,7] -0.577350 [1,2,3,9]$
${}^3F_{-2}^{\downarrow\downarrow}(2)$	$0.707107 [1,3,4,9] -0.577350 [2,3,5,7] +0.288676 [1,3,5,8] +0.288674 [1,4,5,7]$
${}^3F_{-1}^{\downarrow\downarrow}(2)$	$0.547722 [1,3,6,9] -0.223607 [1,5,6,7] +0.547722 [3,4,5,7] -0.365149 [2,3,5,9] +$ $+0.223607 [1,3,7,8] -0.365149 [1,4,5,9] +0.182574 [1,3,5,10]$
${}^3F_0^{\downarrow\downarrow}(2)$	$0.316228 [1,5,7,8] +0.316228 [3,4,5,9] -0.258198 [2,3,7,9] +0.258198 [1,3,7,10] +$ $+0.516398 [1,5,6,9] +0.258199 [1,3,8,9] -0.516398 [3,5,6,7] -0.258199 [1,4,7,9]$
${}^3F_1^{\downarrow\downarrow}(2)$	$0.365149 [1,5,7,10] +0.547722 [3,5,7,8] -0.223607 [3,5,6,9] +0.223607 [3,4,7,9] +$ $-0.182574 [2,5,7,9] +0.365149 [1,5,8,9] -0.547722 [1,6,7,9]$
${}^3F_2^{\downarrow\downarrow}(2)$	$0.577350 [3,5,7,10] -0.288674 [3,5,8,9] -0.288676 [4,5,7,9] +0.707107 [1,7,8,9]$
${}^3F_3^{\downarrow\downarrow}(2)$	$0.707107 [3,5,9,10] +0.288676 [3,7,8,9] +0.288676 [5,6,7,9] -0.577350 [1,7,9,10]$

Table A.4: Symmetry-adapted linear combinations of four-hole products, produced by our numerical procedure.

symmetry-adapted state	linear combination of simple products
${}^3G_{-4}^{\uparrow\uparrow}$	-0.774597 [2,3,4,6] -0.632456 [1,2,4,8]
${}^3G_{-3}^{\uparrow\uparrow}$	-0.547723 [1,2,6,8] -0.223607 [2,3,4,8] +0.670820 [2,4,5,6] -0.447214 [1,2,4,10]
${}^3G_{-2}^{\uparrow\uparrow}$	-0.585540 [1,2,6,10] -0.292770 [1,4,6,8] +0.119523 [2,3,4,10] +0.585540 [2,4,5,8] + +0.146385 [2,3,6,8] -0.439155 [2,4,6,7]
${}^3G_{-1}^{\uparrow\uparrow}$	-0.414039 [1,4,6,10] -0.207020 [3,4,6,8] +0.207020 [2,4,5,10] -0.253546 [2,5,6,8] + -0.338062 [1,2,8,10] +0.414039 [2,3,6,10] +0.591608 [2,4,7,8] -0.207020 [2,4,6,9]
${}^3G_0^{\uparrow\uparrow}$	-0.462910 [3,4,6,10] -0.377964 [1,4,8,10] +0.377964 [2,4,7,10] +0.462910 [2,6,7,8] + +0.377964 [2,3,8,10] -0.377964 [2,4,8,9]
${}^3G_1^{\uparrow\uparrow}$	-0.207020 [1,6,8,10] -0.591608 [3,4,8,10] +0.207020 [2,5,8,10] +0.253546 [4,5,6,10] + +0.414039 [2,6,7,10] +0.207020 [4,6,7,8] +0.338062 [2,4,9,10] -0.414039 [2,6,8,9]
${}^3G_2^{\uparrow\uparrow}$	-0.439155 [3,6,8,10] +0.585540 [4,5,8,10] -0.119523 [2,7,8,10] +0.146385 [4,6,7,10] + +0.585540 [2,6,9,10] -0.292770 [4,6,8,9]
${}^3G_3^{\uparrow\uparrow}$	-0.670820 [5,6,8,10] +0.223607 [4,7,8,10] +0.447214 [2,8,9,10] +0.547723 [4,6,9,10]
${}^3G_4^{\uparrow\uparrow}$	0.774597 [6,7,8,10] +0.632456 [4,8,9,10]
${}^3G_{-4}^{\uparrow\downarrow}$	-0.547723 [1,3,4,6] -0.547723 [2,3,4,5] -0.447214 [1,2,3,8] -0.447214 [1,2,4,7]
${}^3G_{-3}^{\uparrow\downarrow}$	0.474342 [1,4,5,6] -0.387298 [1,2,6,7] -0.158114 [1,3,4,8] -0.158114 [2,3,4,7] + -0.387298 [1,2,5,8] +0.474342 [2,3,5,6] -0.316228 [1,2,3,10] -0.316228 [1,2,4,9]
${}^3G_{-2}^{\uparrow\downarrow}$	-0.103510 [1,3,6,8] -0.517549 [1,4,6,7] -0.414039 [1,2,6,9] +0.084515 [1,3,4,10] + +0.084515 [2,3,4,9] -0.414039 [1,2,5,10] +0.517549 [2,3,5,8] +0.103510 [2,4,5,7] + +0.207020 [1,4,5,8] -0.207020 [2,3,6,7]
${}^3G_{-1}^{\uparrow\downarrow}$	-0.179284 [1,5,6,8] -0.439155 [1,4,6,9] -0.146385 [3,4,5,8] -0.146385 [3,4,6,7] + +0.439155 [2,3,5,10] -0.179284 [2,5,6,7] +0.418330 [1,4,7,8] -0.239046 [1,2,8,9] + +0.146385 [2,3,6,9] -0.146385 [1,4,5,10] -0.239046 [1,2,7,10] +0.418330 [2,3,7,8]
${}^3G_0^{\uparrow\downarrow}$	0.327327 [1,6,7,8] -0.327327 [3,4,5,10] -0.327327 [3,4,6,9] +0.327327 [2,5,7,8] + -0.534522 [1,4,8,9] +0.534522 [2,3,7,10]
${}^3G_1^{\uparrow\downarrow}$	0.146385 [1,6,7,10] -0.439155 [1,6,8,9] -0.418330 [3,4,7,10] -0.418330 [3,4,8,9] + +0.439155 [2,5,7,10] -0.146385 [2,5,8,9] +0.179284 [3,5,6,10] +0.146385 [3,6,7,8] + +0.146385 [4,5,7,8] +0.179284 [4,5,6,9] +0.239046 [1,4,9,10] +0.239046 [2,3,9,10]
${}^3G_2^{\uparrow\downarrow}$	-0.084515 [1,7,8,10] -0.207020 [3,6,7,10] -0.517549 [3,6,8,9] +0.517549 [4,5,7,10] + +0.207020 [4,5,8,9] -0.084515 [2,7,8,9] +0.414039 [1,6,9,10] +0.103510 [3,5,8,10] + -0.103510 [4,6,7,9] +0.414039 [2,5,9,10]
${}^3G_3^{\uparrow\downarrow}$	0.316228 [1,8,9,10] +0.158114 [3,7,8,10] -0.474342 [5,6,7,10] -0.474342 [5,6,8,9] + +0.158114 [4,7,8,9] +0.316228 [2,7,9,10] +0.387298 [3,6,9,10] +0.387298 [4,5,9,10]
${}^3G_4^{\uparrow\downarrow}$	0.447214 [3,8,9,10] +0.547723 [5,7,8,10] +0.547723 [6,7,8,9] +0.447214 [4,7,9,10]
${}^3G_{-4}^{\downarrow\downarrow}$	-0.774597 [1,3,4,5] -0.632456 [1,2,3,7]
${}^3G_{-3}^{\downarrow\downarrow}$	0.670820 [1,3,5,6] -0.223607 [1,3,4,7] -0.547723 [1,2,5,7] -0.447214 [1,2,3,9]
${}^3G_{-2}^{\downarrow\downarrow}$	-0.585540 [1,3,6,7] +0.119523 [1,3,4,9] -0.585540 [1,2,5,9] +0.292770 [2,3,5,7] + +0.439155 [1,3,5,8] -0.146385 [1,4,5,7]
${}^3G_{-1}^{\downarrow\downarrow}$	-0.207020 [1,3,6,9] -0.253546 [1,5,6,7] -0.207020 [3,4,5,7] +0.414039 [2,3,5,9] + +0.591608 [1,3,7,8] -0.414039 [1,4,5,9] -0.338062 [1,2,7,9] +0.207020 [1,3,5,10]
${}^3G_0^{\downarrow\downarrow}$	-0.462910 [3,4,5,9] -0.377964 [1,3,8,9] +0.462910 [1,5,7,8] +0.377964 [2,3,7,9] + +0.377964 [1,3,7,10] -0.377964 [1,4,7,9]
${}^3G_1^{\downarrow\downarrow}$	-0.207020 [1,6,7,9] -0.591608 [3,4,7,9] +0.207020 [2,5,7,9] -0.414039 [1,5,8,9] + +0.253546 [3,5,6,9] +0.338062 [1,3,9,10] +0.414039 [1,5,7,10] +0.207020 [3,5,7,8]

Table A.4: Symmetry-adapted linear combinations of four-hole products, produced by our numerical procedure.

symmetry-adapted state	linear combination of simple products
${}^3G_2^{\downarrow\downarrow}$	$-0.119523 [1,7,8,9] -0.585540 [3,6,7,9] +0.439155 [4,5,7,9] +0.585540 [1,5,9,10] +$ $-0.146385 [3,5,8,9] +0.292770 [3,5,7,10]$
${}^3G_3^{\downarrow\downarrow}$	$0.447214 [1,7,9,10] +0.223607 [3,7,8,9] -0.670820 [5,6,7,9] +0.547723 [3,5,9,10]$
${}^3G_4^{\downarrow\downarrow}$	$0.632456 [3,7,9,10] +0.774597 [5,7,8,9]$
${}^3H_{-5}^{\uparrow\uparrow}$	$[1,2,4,6]$
${}^3H_{-4}^{\uparrow\uparrow}$	$-0.774597 [1,2,4,8] +0.632456 [2,3,4,6]$
${}^3H_{-3}^{\uparrow\uparrow}$	$-0.365148 [1,2,4,10] -0.447214 [1,2,6,8] +0.730297 [2,3,4,8] -0.365148 [2,4,5,6]$
${}^3H_{-2}^{\uparrow\uparrow}$	$-0.365148 [1,2,6,10] -0.182574 [1,4,6,8] +0.447214 [2,3,4,10] +0.547723 [2,3,6,8] +$ $-0.547723 [2,4,5,8] +0.182574 [2,4,6,7]$
${}^3H_{-1}^{\uparrow\uparrow}$	$-0.169031 [1,2,8,10] -0.207020 [1,4,6,10] +0.552052 [2,3,6,10] -0.276026 [3,4,6,8] +$ $-0.414039 [2,4,5,10] +0.507093 [2,5,6,8] -0.338062 [2,4,7,8] +0.069007 [2,4,6,9]$
${}^3H_0^{\uparrow\uparrow}$	$-0.154303 [1,4,8,10] +0.308607 [2,3,8,10] -0.377964 [3,4,6,10] +0.617213 [2,5,6,10] +$ $+0.308607 [4,5,6,8] -0.308607 [2,4,7,10] -0.377964 [2,6,7,8] +0.154303 [2,4,8,9]$
${}^3H_1^{\uparrow\uparrow}$	$-0.069007 [1,6,8,10] -0.338062 [3,4,8,10] +0.414039 [2,5,8,10] +0.507093 [4,5,6,10] +$ $-0.552052 [2,6,7,10] -0.276026 [4,6,7,8] -0.169031 [2,4,9,10] +0.207020 [2,6,8,9]$
${}^3H_2^{\uparrow\uparrow}$	$-0.182574 [3,6,8,10] +0.547723 [4,5,8,10] +0.447214 [2,7,8,10] -0.547723 [4,6,7,10] +$ $-0.365148 [2,6,9,10] +0.182574 [4,6,8,9]$
${}^3H_3^{\uparrow\uparrow}$	$-0.365148 [5,6,8,10] +0.730297 [4,7,8,10] -0.365148 [2,8,9,10] -0.447214 [4,6,9,10]$
${}^3H_4^{\uparrow\uparrow}$	$0.632456 [6,7,8,10] -0.774597 [4,8,9,10]$
${}^3H_5^{\uparrow\uparrow}$	$-[6,8,9,10]$
${}^3H_{-5}^{\uparrow\downarrow}$	$-\sqrt{\frac{1}{2}}[1, 2, 3, 6] - \sqrt{\frac{1}{2}}[1, 2, 4, 5]$
${}^3H_{-4}^{\uparrow\downarrow}$	$-0.547723 [1,2,3,8] -0.547723 [1,2,4,7] +0.447214 [1,3,4,6] +0.447214 [2,3,4,5]$
${}^3H_{-3}^{\uparrow\downarrow}$	$-0.258199 [1,2,3,10] -0.316228 [1,2,5,8] -0.316228 [1,2,6,7] -0.258199 [1,2,4,9] +$ $+0.516398 [1,3,4,8] -0.258199 [1,4,5,6] -0.258199 [2,3,5,6] +0.516398 [2,3,4,7]$
${}^3H_{-2}^{\uparrow\downarrow}$	$-0.258199 [1,2,5,10] -0.258199 [1,2,6,9] +0.316228 [1,3,4,10] -0.516398 [1,4,5,8] +$ $+0.516398 [2,3,6,7] +0.316228 [2,3,4,9] +0.258199 [1,3,6,8] -0.258199 [2,4,5,7]$
${}^3H_{-1}^{\uparrow\downarrow}$	$-0.119523 [1,2,7,10] -0.119523 [1,2,8,9] -0.439155 [1,4,5,10] -0.239046 [1,4,7,8] +$ $-0.097590 [1,4,6,9] +0.097590 [2,3,5,10] -0.239046 [2,3,7,8] +0.439155 [2,3,6,9] +$ $+0.243975 [1,3,6,10] +0.358569 [1,5,6,8] -0.195180 [3,4,5,8] -0.195180 [3,4,6,7] +$ $+0.358569 [2,5,6,7] -0.243975 [2,4,5,9]$
${}^3H_0^{\uparrow\downarrow}$	$-0.327327 [1,4,7,10] +0.327327 [2,3,8,9] +0.436436 [1,5,6,10] -0.267261 [1,6,7,8] +$ $-0.267261 [3,4,5,10] -0.267261 [3,4,6,9] -0.267261 [2,5,7,8] +0.436436 [2,5,6,9] +$ $+0.109109 [1,3,8,10] +0.218218 [3,5,6,8] +0.218218 [4,5,6,7] -0.109109 [2,4,7,9]$
${}^3H_1^{\uparrow\downarrow}$	$-0.439155 [1,6,7,10] +0.097590 [1,6,8,9] -0.239046 [3,4,7,10] -0.239046 [3,4,8,9] +$ $-0.097590 [2,5,7,10] +0.439155 [2,5,8,9] +0.243975 [1,5,8,10] +0.358569 [3,5,6,10] +$ $-0.195180 [3,6,7,8] -0.195180 [4,5,7,8] +0.358569 [4,5,6,9] -0.243975 [2,6,7,9] +$ $-0.119523 [1,4,9,10] -0.119523 [2,3,9,10]$
${}^3H_2^{\uparrow\downarrow}$	$0.316228 [1,7,8,10] -0.516398 [3,6,7,10] +0.516398 [4,5,8,9] +0.316228 [2,7,8,9] +$ $-0.258199 [1,6,9,10] +0.258199 [3,5,8,10] -0.258199 [4,6,7,9] -0.258199 [2,5,9,10]$
${}^3H_3^{\uparrow\downarrow}$	$-0.258199 [1,8,9,10] +0.516398 [3,7,8,10] -0.258199 [5,6,7,10] -0.258199 [5,6,8,9] +$ $+0.516398 [4,7,8,9] -0.258199 [2,7,9,10] -0.316228 [3,6,9,10] -0.316228 [4,5,9,10]$
${}^3H_4^{\uparrow\downarrow}$	$-0.547723 [3,8,9,10] +0.447214 [5,7,8,10] +0.447214 [6,7,8,9] -0.547723 [4,7,9,10]$
${}^3H_5^{\uparrow\downarrow}$	$-\sqrt{\frac{1}{2}}[5, 8, 9, 10] - \sqrt{\frac{1}{2}}[6, 7, 9, 10]$

Table A.4: Symmetry-adapted linear combinations of four-hole products, produced by our numerical procedure.

symmetry-adapted state	linear combination of simple products
${}^3H_{-5}^{\downarrow\downarrow}$	$-[1,2,3,5]$
${}^3H_{-4}^{\downarrow\downarrow}$	$-0.774597 [1,2,3,7] + 0.632456 [1,3,4,5]$
${}^3H_{-3}^{\downarrow\downarrow}$	$-0.365148 [1,2,3,9] - 0.447214 [1,2,5,7] + 0.730297 [1,3,4,7] - 0.365148 [1,3,5,6]$
${}^3H_{-2}^{\downarrow\downarrow}$	$-0.365148 [1,2,5,9] + 0.447214 [1,3,4,9] - 0.547723 [1,4,5,7] + 0.182574 [2,3,5,7] + 0.547723 [1,3,6,7] - 0.182574 [1,3,5,8]$
${}^3H_{-1}^{\downarrow\downarrow}$	$-0.169031 [1,2,7,9] - 0.552052 [1,4,5,9] + 0.207020 [2,3,5,9] + 0.414039 [1,3,6,9] + 0.507093 [1,5,6,7] - 0.276026 [3,4,5,7] - 0.338062 [1,3,7,8] - 0.069007 [1,3,5,10]$
${}^3H_0^{\downarrow\downarrow}$	$-0.308607 [1,4,7,9] + 0.154303 [2,3,7,9] + 0.617213 [1,5,6,9] - 0.377964 [3,4,5,9] + 0.308607 [1,3,8,9] - 0.377964 [1,5,7,8] + 0.308607 [3,5,6,7] - 0.154303 [1,3,7,10]$
${}^3H_1^{\downarrow\downarrow}$	$-0.414039 [1,6,7,9] - 0.338062 [3,4,7,9] + 0.069007 [2,5,7,9] + 0.552052 [1,5,8,9] + 0.507093 [3,5,6,9] - 0.169031 [1,3,9,10] - 0.207020 [1,5,7,10] - 0.276026 [3,5,7,8]$
${}^3H_2^{\downarrow\downarrow}$	$0.447214 [1,7,8,9] - 0.547723 [3,6,7,9] + 0.182574 [4,5,7,9] - 0.365148 [1,5,9,10] + 0.547723 [3,5,8,9] - 0.182574 [3,5,7,10]$
${}^3H_3^{\downarrow\downarrow}$	$-0.365148 [1,7,9,10] + 0.730297 [3,7,8,9] - 0.365148 [5,6,7,9] - 0.447214 [3,5,9,10]$
${}^3H_4^{\downarrow\downarrow}$	$-0.774597 [3,7,9,10] + 0.632456 [5,7,8,9]$
${}^3H_5^{\downarrow\downarrow}$	$-[5,7,9,10]$
${}^5D_{-2}^{\uparrow\uparrow\uparrow}$	$-[1,3,5,7]$
${}^5D_{-1}^{\uparrow\uparrow\uparrow}$	$-[1,3,5,9]$
${}^5D_0^{\uparrow\uparrow\uparrow}$	$-[1,3,7,9]$
${}^5D_1^{\uparrow\uparrow\uparrow}$	$-[1,5,7,9]$
${}^5D_2^{\uparrow\uparrow\uparrow}$	$-[3,5,7,9]$
${}^5D_{-2}^{\uparrow\uparrow\downarrow}$	$-\frac{1}{2}[1,3,5,8] - \frac{1}{2}[1,3,6,7] - \frac{1}{2}[1,4,5,7] - \frac{1}{2}[2,3,5,7]$
${}^5D_{-1}^{\uparrow\uparrow\downarrow}$	$-\frac{1}{2}[1,3,6,9] - \frac{1}{2}[1,4,5,9] - \frac{1}{2}[1,3,5,10] - \frac{1}{2}[2,3,5,9]$
${}^5D_0^{\uparrow\uparrow\downarrow}$	$-\frac{1}{2}[1,3,8,9] - \frac{1}{2}[2,3,7,9] - \frac{1}{2}[1,3,7,10] - \frac{1}{2}[1,4,7,9]$
${}^5D_1^{\uparrow\uparrow\downarrow}$	$-\frac{1}{2}[1,5,7,10] - \frac{1}{2}[2,5,7,9] - \frac{1}{2}[1,5,8,9] - \frac{1}{2}[1,6,7,9]$
${}^5D_2^{\uparrow\uparrow\downarrow}$	$-\frac{1}{2}[3,5,7,10] - \frac{1}{2}[3,5,8,9] - \frac{1}{2}[3,6,7,9] - \frac{1}{2}[4,5,7,9]$
${}^5D_{-2}^{\uparrow\downarrow\downarrow}$	$-\sqrt{\frac{1}{6}}[2,3,5,8] - \sqrt{\frac{1}{6}}[1,4,6,7] - \sqrt{\frac{1}{6}}[1,3,6,8] - \sqrt{\frac{1}{6}}[1,4,5,8] +$ $-\sqrt{\frac{1}{6}}[2,3,6,7] - \sqrt{\frac{1}{6}}[2,4,5,7]$
${}^5D_{-1}^{\uparrow\downarrow\downarrow}$	$-\sqrt{\frac{1}{6}}[1,4,6,9] - \sqrt{\frac{1}{6}}[1,3,6,10] - \sqrt{\frac{1}{6}}[2,3,6,9] - \sqrt{\frac{1}{6}}[1,4,5,10] +$ $-\sqrt{\frac{1}{6}}[2,4,5,9] - \sqrt{\frac{1}{6}}[2,3,5,10]$
${}^5D_0^{\uparrow\downarrow\downarrow}$	$-\sqrt{\frac{1}{6}}[2,3,8,9] - \sqrt{\frac{1}{6}}[1,3,8,10] - \sqrt{\frac{1}{6}}[1,4,8,9] - \sqrt{\frac{1}{6}}[2,3,7,10] +$ $-\sqrt{\frac{1}{6}}[2,4,7,9] - \sqrt{\frac{1}{6}}[1,4,7,10]$
${}^5D_1^{\uparrow\downarrow\downarrow}$	$-\sqrt{\frac{1}{6}}[2,5,7,10] - \sqrt{\frac{1}{6}}[1,5,8,10] - \sqrt{\frac{1}{6}}[1,6,7,10] - \sqrt{\frac{1}{6}}[2,5,8,9] +$ $-\sqrt{\frac{1}{6}}[2,6,7,9] - \sqrt{\frac{1}{6}}[1,6,8,9]$
${}^5D_2^{\uparrow\downarrow\downarrow}$	$-\sqrt{\frac{1}{6}}[4,5,7,10] - \sqrt{\frac{1}{6}}[3,6,8,9] - \sqrt{\frac{1}{6}}[3,5,8,10] - \sqrt{\frac{1}{6}}[3,6,7,10] +$ $-\sqrt{\frac{1}{6}}[4,5,8,9] - \sqrt{\frac{1}{6}}[4,6,7,9]$
${}^5D_{-2}^{\uparrow\downarrow\downarrow}$	$-\frac{1}{2}[2,3,6,8] - \frac{1}{2}[2,4,5,8] - \frac{1}{2}[1,4,6,8] - \frac{1}{2}[2,4,6,7]$
${}^5D_{-1}^{\uparrow\downarrow\downarrow}$	$-\frac{1}{2}[1,4,6,10] - \frac{1}{2}[2,4,6,9] - \frac{1}{2}[2,3,6,10] - \frac{1}{2}[2,4,5,10]$
${}^5D_0^{\uparrow\downarrow\downarrow}$	$-\frac{1}{2}[2,3,8,10] - \frac{1}{2}[2,4,8,9] - \frac{1}{2}[1,4,8,10] - \frac{1}{2}[2,4,7,10]$

Table A.4: Symmetry-adapted linear combinations of four-hole products, produced by our numerical procedure.

symmetry-adapted state	linear combination of simple products
${}^5D_1^{\uparrow\downarrow\downarrow\downarrow}$	$-\frac{1}{2}[2, 5, 8, 10] - \frac{1}{2}[2, 6, 7, 10] - \frac{1}{2}[1, 6, 8, 10] - \frac{1}{2}[2, 6, 8, 9]$
${}^5D_2^{\uparrow\downarrow\downarrow\downarrow}$	$-\frac{1}{2}[4, 5, 8, 10] - \frac{1}{2}[4, 6, 7, 10] - \frac{1}{2}[3, 6, 8, 10] - \frac{1}{2}[4, 6, 8, 9]$
${}^5D_{-2}^{\downarrow\downarrow\downarrow\downarrow}$	$-[2, 4, 6, 8]$
${}^5D_{-1}^{\downarrow\downarrow\downarrow\downarrow}$	$-[2, 4, 6, 10]$
${}^5D_0^{\downarrow\downarrow\downarrow\downarrow}$	$-[2, 4, 8, 10]$
${}^5D_1^{\downarrow\downarrow\downarrow\downarrow}$	$-[2, 6, 8, 10]$
${}^5D_2^{\downarrow\downarrow\downarrow\downarrow}$	$-[4, 6, 8, 10]$

Table A.5: Corrections to the free-ion (spherical symmetry) energy levels resulting from the surface ligand field.

free-ion state	surface state	ligand-field correction	resulting energy [eV]
1S	A_1	$2\varepsilon_0$	9.4113
3P	A_1	$2\varepsilon_0 + \frac{14}{5}D_S$	2.8150
	E	$2\varepsilon_0 - \frac{7}{5}D_S$	3.0565
1D	A_1	$2\varepsilon_0 + \frac{6}{7}D_S + \frac{24}{7}D_q$	2.6999
	B_1	$2\varepsilon_0 - \frac{6}{7}D_S + \frac{24}{7}D_q + \frac{20}{7}D_U$	3.2499
	B_2	$2\varepsilon_0 - \frac{6}{7}D_S - \frac{16}{7}D_q - \frac{20}{7}D_U$	2.6784
	E_{α}, E_{β}	$2\varepsilon_0 - \frac{3}{7}D_S - \frac{16}{7}D_q$	3.1052
3F	B_1	$2\varepsilon_0 + 2D_q - 5D_U$	0.0000
	E_{α}, E_{β}	$2\varepsilon_0 - D_S + 2D_q + \frac{15}{4}D_U$	1.4400
	B_2	$2\varepsilon_0 + 12D_q + 5D_U$	1.0000
	A_2	$2\varepsilon_0 - \frac{4}{5}D_S - 6D_q$	1.3000
	E_{γ}, E_{δ}	$2\varepsilon_0 + \frac{2}{5}D_S - 6D_q - \frac{15}{4}D_U$	0.6385
1G	$A_{1\alpha}$	$2\varepsilon_0 + 4D_q + \frac{5}{3}D_U$	3.9453
	$A_{1\beta}$	$2\varepsilon_0 + \frac{8}{7}D_S + \frac{4}{7}D_q - \frac{5}{3}D_U$	3.5518
	B_1	$2\varepsilon_0 - \frac{8}{7}D_S + \frac{4}{7}D_q + \frac{15}{7}D_U$	4.2851
	A_2	$2\varepsilon_0 + 4D_S + 2D_q$	3.5680
	E_{α}, E_{β}	$2\varepsilon_0 - 2D_S + 2D_q + \frac{5}{4}D_U$	4.1105
	B_2	$2\varepsilon_0 - \frac{8}{7}D_S - \frac{26}{7}D_q - \frac{15}{7}D_U$	3.8566
	E_{γ}, E_{δ}	$2\varepsilon_0 + \frac{4}{7}D_S - \frac{26}{7}D_q - \frac{5}{4}D_U$	3.8991

Bibliography

- [1] J. Hubbard, Proc. Roy. Soc. London Ser. A **276**, 238 (1963), M. C. Gutzwiller, Phys. Rev. Lett. **10**, 159 (1963), J. Kanamori, Progr. Theor. Phys. **30**, 275 (1963).
- [2] P. A. Franken, A. E. Hill, C. W. Peters, and E. Weinreich, Phys. Rev. Lett. **7**, 118 (1961).
- [3] J. de Boeck and G. Borghs, Phys. World, April 1999, 27 (1999).
- [4] M. Fiebig, D. Fröhlich, G. Sluyterman, and R.V. Pisarev, Appl. Phys. Lett. **66**, 2906 (1995).
- [5] M. Fiebig, D. Fröhlich, B. B. Krichevtsov, and R. V. Pisarev, Phys. Rev. Lett. **73**, 2127 (1994).
- [6] W. L. Roth, J. Appl. Phys. **31**, 2000 (1960).
- [7] V. V. Eremenko and N. F. Kharchenko, Sov. Sci. Rev. A **5**, 1 (1984).
- [8] J. F. Dillon, J. Magn. Magn. Mat. **100**, 425 (1991).
- [9] J. Baruchel, M. Schlenker, and W. L. Roth, J. Appl. Phys. **48**, 5 (1976).
- [10] U. Hillebrecht, private communication, compare also J. Stöhr, A. Scholl, T. J. Regan, S. Anders, J. Lüning, M. R. Scheinfein, H. A. Padmore, and R. L. White, Phys. Rev. Lett. **83**, 1862 (1999).
- [11] D. Fröhlich, Physica Scripta **T35**,125 (1995)
- [12] R. P. Pan, H. D. Wei, and Y. R. Shen, Phys. Rev. B **39**, 1229 (1989).
- [13] W. Hübner and K.-H. Bennemann, Phys. Rev. B **40**, 5973 (1989).
- [14] T. A. Luce, W. Hübner, and K. H. Bennemann, Phys. Rev. Lett. **77**, 2810 (1996).
- [15] A. Kirilyuk, T. Rasing, R. Mégy, and P. Beauvillain, Phys. Rev. Lett. **77**, 4608 (1996).
- [16] A. V. Petukhov, I. L. Lyubchanskii, and T. Rasing, Phys. Rev. B, **56**, 2680 (1997).
- [17] U. Pustogowa, T. A. Luce, W. Hübner, and K. H. Bennemann, J. Appl. Phys. **79**, 6177 (1996).

- [18] M. Straub, R. Vollmer, and J. Kirschner, Phys. Rev. Lett. **77**, 743 (1996).
- [19] J. Schmalian and W. Hübner, Phys. Rev. B **53**, 11860 (1996).
- [20] K. B. Lyons, J. Kwo, J. F. Dillon, G. P. Espinosa, M. McGlashan-Powell, A. P. Ramirez, and L. F. Schneemeyer, Phys. Rev. Lett. **64**, 3294 (1990).
- [21] T. Rasing, M. Groot Koerkamp, and B. Koopmans, J. Appl. Phys. **79**, 6181 (1996).
- [22] Y. J. Ding and A. E. Kaplan, Phys. Rev. Lett. **63**, 2725 (1989).
- [23] M. G. Raizen and B. Rosenstein, Phys. Rev. Lett. **65**, 2744 (1990), G. W. Ford and D. G. Steel, Phys. Rev. Lett. **65**, 2745 (1990) and the reply thereafter.
- [24] M. Fiebig, D. Fröhlich, and H-J. Thiele, Phys. Rev. B **54**, R12681 (1996).
- [25] S. Kielich and R. Zawodny, Optics Comm. **4**, 132 (1971).
- [26] J. Rosen, *Symmetry in Science* (Springer-Verlag Inc., New York, 1995).
- [27] P. Argyres, Phys. Rev. **97**, 334 (1955).
- [28] W. F. Brown, S. Shtrikman, and D. Treves, J. Appl. Phys. **34**, 1233 (1963).
- [29] V. V. Eremenko and N. F. Kharchenko, Phys. Rep. **155**, 379 (1987).
- [30] I. Dzyaloshinskii and E. V. Papamichail, Phys. Rev. Lett. **75**, 3004 (1995)
- [31] S. Kielich and R. Zawodny, Acta Phys. Polonica A **43**, 579 (1973).
- [32] I. L. Lyubchanskii, Phys. Solid State **37**, 387 (1995).
- [33] S. B. Borisov, N. N. Dadoenkova, I. L. Lyubchanskii, and V. L. Sobolev, Sov. Phys. Solid State **32**, 2127 (1990).
- [34] S. B. Borisov, N. N. Dadoenkova, I. L. Lyubchanskii, and V. L. Sobolev, Sov. Phys. Solid State **33**, 1061 (1991).
- [35] N. N. Akhmediev, S. B. Borisov, A. K. Zvezdin, I. L. Lyubchanskii, and Yu. V. Melikhov, Sov. Phys. Solid State **27**, 650 (1985).
- [36] V. N. Muthukumar, R. Valenti, and C. Gros, Phys. Rev. Lett. **75**, 2766 (1995).
- [37] Y. Tanabe, M. Muto, and E. Hanamura, Solid State Comm. **102**, 643 (1997).
- [38] F. Bassani and S. Scandolo, Phys. Rev. B **44**, 8446 (1991).
- [39] M. Trzeciecki, W. Hübner, unpublished.
- [40] A. Dähn, W. Hübner, and K. H. Bennemann, Phys. Rev. Lett. **77**, 3929 (1996).

- [41] R. R. Birss, *Symmetry and Magnetism* (North Holland, Amsterdam, 1964).
- [42] J. E. Sipe, D. J. Moss, and H. M. van Driel, *Phys. Rev. B* **35**, 1129 (1987).
- [43] I. E. Dzialoshinskii, *Sov. Phys. JETP* **5**, 1259 (1957).
- [44] M. Trzeciecki and W. Hübner, *Appl. Phys. B* **68**, 473 (1999).
- [45] A. Dähn, “Gruppentheorie der optischen Frequenzverdopplung an antiferromagnetischen Oberflächen”, Master’s Thesis, Freie Universität Berlin, 1996.
- [46] W. Hübner, K. H. Bennemann, *Phys. Rev. B* **52**, 13411 (1995).
- [47] E. Iguchi and H. Nakatsugawa, *Phys. Rev. B* **51**, 10956 (1995).
- [48] G. Renaud, B. Villette, I. Vilfan, and A. Bourret, *Phys. Rev. Lett.* **73**, 1825 (1994).
- [49] M. J. Gillan, unpublished.
- [50] M. Fiebig, D. Fröhlich, and R.V. Pisarev, *J. Appl. Phys.* **81**, 4875 (1997)
- [51] M. Fiebig, D. Fröhlich, S. Leute, and R.V. Pisarev, *Appl. Phys. B.* **66**, 265 (1998).
- [52] D. Gabrielli, G. Jona-Lasinio, C. Landim, *Phys. Rev. Lett.* **77**, 1202 (1996).
- [53] J. L. Lebowitz, H. Spohn, *Phys. Rev. Lett.* **78**, 394 (1997).
- [54] D. Gabrielli, G. Jona-Lasinio, C. Landim, *Phys. Rev. Lett.* **78** 395 (1997).
- [55] E. B. Graham and R. E. Raab, *Phys. Rev. B* **59**, 7058 (1999).
- [56] A. L. Shelankov, *Phys. Rev. Lett.* **71**, 2658 (1993).
- [57] B. L. Petersen, A. Bauer, G. Meyer, T. Crecelius, G. Kaindl, *Appl. Phys. Lett.* **73**, 538 (1998).
- [58] A. Kapitulnik, J. S. Dodge, and M. M. Fejer, *J. Appl. Phys.* **75**, 6872 (1994).
- [59] S. Spielman, K. Fesler, C. B. Eom, T. H. Geballe, M. M. Fejer, A. Kapitulnik, *Phys. Rev. Lett.* **65**, 123 (1990).
- [60] F. Perrin, *J. Chem. Phys.* **51**, 415 (1942).
- [61] A. L. Shelankov and G. E. Pikus, *Phys. Rev. B* **46**, 3326 (1992).
- [62] J. A. Armstrong, N. Bloembergen, J. Ducuing, P. S. Pershan, *Phys. Rev.* **127**, 1918 (1962).
- [63] M. Fiebig, “Nichtlineare Spektroskopie und Topografie an antiferromagnetischen Domänen”, PhD Thesis, Universität Dortmund, 1996.

- [64] W. Brenig, *Statistische Theorie der Wärme* (Springer, Berlin, 1975).
- [65] P. Weinberger in J. L. Moran-Lopez (Ed.), *Current Problems in Condensed Matter*, proceedings of an International Workshop on Current Problems in Condensed Matter: Theory and Experiment, pp. 87-93, Plenum Press New York (1998).
- [66] M. Tinkham, *Group Theory and Quantum Mechanics* (McGraw-Hill, New York, 1964).
- [67] M. Trzeciecki, A. Dähn, and W. Hübner, *Phys. Rev. B* **60**, 1144 (1999).
- [68] N. Bloembergen, *Nonlinear Optics* (W.A. Benjamin Inc., 1965).
- [69] Y. R. Shen *The Principles of Nonlinear Optics* (Wiley and Sons, New York, 1984).
- [70] J. Dewitz, “Nichtlineare Magneto-Optik an Fe Monolagen”, PhD Thesis, Martin-Luther Universität Halle - Wittenberg, 1999.
- [71] K. Terakura, A. R. Williams, T. Oguchi, and J. Kübler, *Phys. Rev. Lett.* **52**, 1830 (1984).
- [72] A. Gorschlüter and H. Merz, *Phys. Rev. B* **49**, 17293 (1994).
- [73] W. Hübner, K. H. Bennemann, and K. Böhmer, *Phys. Rev. B* **50**, 17597 (1994).
- [74] P. Fulde, *Electron Correlation in molecules and Solids, 3rd edit.* (Springer, Heidelberg, 1995); J. Wahle, N. Blümer, J. Schlipf, K. Held, and D. Vollhardt, *Phys. Rev. B* **58**, 12749 (1998).
- [75] W. Hübner and L. M. Falicov, *Phys. Rev. B* **47**, 8783 (1993).
- [76] M. Oleś, G. Stollhoff, *Phys. Rev. B* **29**, 314 (1984).
- [77] C. E. Moore, *Atomic Energy Levels*, Natl. Bur. Stand. (U.S.), U.S. GPO, Washington DC (1971).
- [78] H. C. Schläfer, G. Gliemann, “Einführung in die Ligandenfeldtheorie”, Geest & Portig K.-G., Leipzig 1967.
- [79] A. Fujimori, F. Minami, *Phys. Rev. B* **30**, 957 (1984).
- [80] A. Kirilyuk, V. V. Pavlov, R. V. Pisarev, and Th. Rasing, *Phys. Rev. B* **61**, R3796 (2000).
- [81] B. Fromme, M. Möller, Th. Anshütz, C. Bethke, and E. Kisker, *Phys. Rev. Lett.* **77**, 1548 (1996).
- [82] P. A. Cox and A. A. Williams, *Surf. Sci.* **152/153**, 791 (1985).
- [83] E. Beaurepaire, J.-C. Merle, A. Daunois, and J.-Y. Bigot, *Phys. Rev. Lett.* **76**, 4250 (1996).

- [84] J. Hohlfeld, E. Matthias, R. Knorren, and K. H. Bennemann, Phys. Rev. Lett. **78**, 4861 (1997), *ibid* **79**, 960 (1997) (erratum).
- [85] A. Scholl, L. Baumgarten, R. Jacquemin, and W. Eberhardt, Phys. Rev. Lett. **79**, 5146 (1997).
- [86] M. Aeschlimann, M. Bauer, S.Pawlik, W. Weber, R. Burgermeister, D.Oberli, and H. C. Siegmann, Phys. Rev. Lett. **79**, 5158 (1997).
- [87] A. Vaterlaus, T. Beutler, and F. Meier, Phys. Rev. Lett. **67**, 3314 (1991).
- [88] W. Hübner and G. P. Zhang, Phys. Rev. B **58**, R5920 (1998).
- [89] G. P. Zhang and W. Hübner, Appl. Phys. B **68**, 495 (1999).
- [90] D. P. DiVincenzo and D. Loss, J. Magn. Magn. Mat. **200**, 202 (1999).
- [91] See, e.g. M. Oestreich, J. Hübner, D. Hägele, P. J. Klar, W.Heimbrodtt, W. W. Rühle, D. E. Ashenford, and B. Lunn, Appl. Phys. Lett. **74**, 1251 (1999), and references therein.

Acknowledgements

This work would be impossible to complete without the help I obtained from many people.

Let me thank my family, namely to my grandmother, mother and wife Agnieszka. They were fulfilling a heavy but hardly visible duty of guarding my hearth while I was doing science.

My direct supervisor, Dr. Wolfgang Hübner, introduced me to the amazing field of nonlinear magneto-optics and was guiding me there. This outstanding scientist invested much of his time in making our cooperation so fruitful. He is not only a talented team leader, but also presents exceptional human qualities.

I wish to thank Prof. Jürgen Kirschner for accepting me into his department at the Max-Planck-Institut für Mikrostrukturphysik. Thanks to him I got the chance to learn physics in a very stimulating environment, at the institute where the most modern research is being made.

Dr. Leszek Adamowicz deserves my very special thanks for many fruitful discussions and for the grant of the Warsaw University of Technology.

I want to express my gratitude towards my colleagues, Torsten Andersen, Holger Kirschner, Marek Pajda, and Ricardo Gomez Abal. I received much support from them.

Zusammenfassung

In dieser Arbeit wurde eine Theorie für die optische Frequenzverdopplung (SHG) an den Oberflächen antiferromagnetischer Oxide entwickelt.

Die neuen Gebiete der Technologie, wie magnetische Speicherelemente oder Quantencomputer, benötigen neue Materialien. Beispielsweise beruhen die für Anwendungen als Computerspeicher vorgesehene TMR - tunneling magnetoresistance - Bauelemente auf Dreifachschicht-Sandwiches, denen Mittelschicht ein Oxid beinhaltet. Die magnetischen Eigenschaften dieses häufig antiferromagnetischen Oxids beeinflussen die Leistung des Gerätes, ein Studium der magnetischen Struktur der Mittelschicht ist also von großer Bedeutung. Eine bequeme Methode, solche "verborgenen" oxidischen Schichten zu untersuchen, ist die SHG (second harmonic generation). Darum ist es von großer Bedeutung, die nicht-lineare optische Antwort solcher Strukturen theoretisch zu studieren und Vorhersagen zu gewinnen.

Es wurde schon experimentell bestätigt, dass SHG für Oberflächen sensitiv ist, weil eine Grenzfläche die Inversionssymmetrie bricht. Andererseits gibt es hervorragende experimentelle Ergebnisse über Domänenabbildung im Volumen antiferromagnetischer Materialien die keine Inversionssymmetrie besitzen (Cr_2O_3). Dadurch entsteht die Frage, ob SHG die Fähigkeit besitzt, die magnetische Struktur an Oberflächen inversionssymmetrischer Antiferromagnete (wie z.B. Nickeloxid NiO) zu untersuchen. Die Frage wird in dieser Dissertation beantwortet.

In *ferromagnetischen* Metallen wurden von mehreren experimentellen Arbeitsgruppen mit verschiedenen zeitaufgelösten optischen Methoden ein Zerfall der Magnetisierung in weniger als einer Pikosekunde sowie Abweichungen vom Fermiflüssigkeitsverhalten beobachtet, sodass die üblicherweise für Ummagnetisierungsprozesse erforderliche Beteiligung und Erwärmung des Kristallgitters nur von untergeordneter Bedeutung sein kann. Es ist zu erwarten, dass *antiferromagnetische* oxidische Grenzflächen aufgrund ihrer elektronischen Struktur teils ähnliche, teils neuartige magnetische Effekte im Femtosekunden-Bereich zeigen und besondere Relevanz für Anwendungen ultraschneller Prozesse in der Magneto-Elektronik erlangen werden. Oxidische Grenzflächen eignen sich auch besonders gut für Untersuchungen der Spin-Dynamik auf der Femtosekunden-Skala, da sie (i) über ein reichhaltiges magnetisches Phasendiagramm, (ii) über ein stark korreliertes Elektronensystem mit hoher Zustandsdichte und gleichzeitig großer Bandlücke verfügen und (iii) an der Grenzfläche zu Metallsubstraten (Metall/Metalloxid-Grenzfläche mit jeweils demselben Metall) die Wärmeabfuhr der laserinduzierten Prozesse in das Gitter des Substrates erfolgen kann, ohne das spindynamisch aktive Oxid zu beeinflussen.

Deshalb haben wir ein Material gewählt, das eine einfache Kristallstruktur besitzt, aber die Untersuchung der Oberflächenempfindlichkeit der SHG *und* der Korrelationseffekte ermöglicht. Es ist wichtig zu bemerken, dass die in dieser Arbeit entwickelten Methoden und erzeugten Resultate auch auf andere Oxide übertragen werden können.

Symmetrieanalyse: Der erster Teil der Arbeit (Kapitel 2) betrifft die gruppentheoretische Analyse der optischen Frequenzverdopplung an den Oberflächen antiferromagnetischer Oxide. Die bisher existierenden wichtigen Arbeiten zur gruppentheoretischen Klassifizierung antiferromagnetischer *Volumen*-Spinstrukturen lassen eine gewisse konzeptionelle Lücke zwischen den vorhergesagten Tensorelementen einerseits, und dem experimentell erwarteten Ergebnis andererseits. Wenn man sich aber vor Augen führt, dass erst 1994 erstmals Volumen-Domänen in einem Antiferromagneten (dem Oxid Cr_2O_3) experimentell abgebildet werden konnten und dass der zugrundeliegende Mechanismus noch nicht einmal in seinem Symmetrie-Ursprung (geschweige denn elektronisch) voll verstanden ist, wird rasch klar, dass selbst auf dem Niveau der Symmetrie-Analyse für antiferromagnetische oxidische Grenzflächen noch viele Fragen offen bleiben. Ein Teil davon wird in der vorliegenden Arbeit beantwortet. Im Unterschied zur Analyse des Antiferromagnetismus in Volumen konzentriert sich unsere Arbeit auf die niedrig indizierten Oberflächen kubischer Antiferromagnete und kann sich daher auf diejenige Beiträge zur optischen Frequenzverdopplung beschränken, welche von elektrischen Dipolanteilen herrühren. Daher wenden wir die Gruppentheorie an, um die nicht-verschwindenden Elemente des Tensors $\chi_{el}^{(2\omega)}$ für verschiedene antiferromagnetisch geordnete Oberflächen zu bestimmen. Die Zahl der unterscheidbaren Spinkonfigurationen ist verschieden je nach der Oberflächenorientierung. Darüber hinaus betrachten wir Gitterverzerrungen des magnetischen und nichtmagnetischen Untergitters und Einheitszellen mit zwei Arten magnetischer Atome. Letzterer Aspekt stellt eine wichtige Vorarbeit im Hinblick auf das (z. B. von den Hochtemperatur-Supraleitern) bekannte nichtstöchiometrische Verhalten oxidischer Materialien (Sauerstoff-Verluste) dar.

Unsere Ergebnisse zeigen, dass in den verschiedenen antiferromagnetischen Spinkonfigurationen oftmals unterschiedliche nicht-verschwindende Elemente des Tensors $\chi_{el}^{(2\omega)}$ auftreten. Damit erlaubt die optische Frequenzverdopplung nicht nur die Unterscheidung der antiferromagnetischen *Phase* von der para- oder ferromagnetischen Phase, sondern gestattet darüber hinaus in vielen Fällen sogar die Identifikation der detaillierten antiferromagnetischen *Spinkonfiguration*. Die zuvor erwähnten Verzerrungen lassen sich ebenfalls mittels SHG detektieren.

Ein weiteres wichtiges Resultat unserer Arbeit besteht darin, dass die optische Frequenzverdopplung antiferromagnetische *Oberflächendomänen* an kubischen Oxiden abbilden kann, ohne auf einen externen Referenzstrahl zurückgreifen zu müssen (wie etwa bei YMnO_3). Unsere Methode beruht darauf, dass einige Tensorelemente beim Übergang von einer Domäne zur anderen ihr Vorzeichen wechseln, während andere gleich bleiben. Dadurch besitzt die Intensität des reflektierten SHG-Lichtes einen Interferenzterm, der zum Domänenkontrast führt.

Ein wichtiger Beitrag zur Symmetrieklassifizierung der nichtlinearen Optik, der in dieser Arbeit entwickelt wurde, besteht aus der sorgfältigen Analyse der Rolle der Zeitumkehr. Bisher wurde diese Operation oftmals als gleichbedeutend mit Magnetisierungskehr be-

handelt. In vielen Arbeiten wurde das innere magnetische Feld der Probe anders betrachtet als das der elektromagnetischen Welle, und dadurch ging der Unterschied zwischen Zeitumkehr-Symmetrie und Reziprozität verloren. Unsere Analyse zeigt jedoch, dass die Nicht-Reziprozität sich aus der Tatsache ergibt, dass das Licht auf die magnetischen Momente verschiedener Orientierung verschieden wirkt, während aber die Zeitumkehr *beide* Elemente, d.h. das Licht sowie die magnetische Ordnung der Probe beeinflusst. Diese Ursache ist für die SHG an Antiferromagneten von großer Bedeutung, weil (i) Zeitumkehr den Ordnungsparameter eines Antiferromagnets *nicht* notwendigerweise umkehrt und (ii) die SHG keine Dissipation im Sinne eines Abzugs der Strahlungsenergie besitzt. Dagegen ist eine andere Art der Dissipation, die einer Umverteilung der Frequenzen entspricht, in SHG vorhanden und verursacht eine Zeitumkehr-Asymmetrie der SHG. Wir schließen daraus, dass SHG einen *dynamischen* Prozess darstellt und Zeitumkehr nicht in dessen Analyse verwendet werden darf.

Ferner führt die Anwendung des Zeitumkehr in der Symmetrieanalyse zu Aussagen über die komplexe Phase eines Tensorelements. Diese Feststellungen (eine feste 90° -Phasendifferenz zwischen verschiedenen Tensorelementen) lassen sich aufgrund der elektronischen Theorie nicht bestätigen und führen zu falschen Ergebnissen für die Domänenabbildung. Unsere Theorie leidet nicht an diesen Mängeln.

Elektronische Theorie: Von den Ergebnissen der Symmetrieanalyse ausgehend, entwickeln wir eine elektronische Beschreibung der hochangeregten Zustände in NiO (Kapitel 3 der Dissertation). Dazu betrachten wir die elektronische Konfigurationen $3d^8$, $3d^74s$, und $3d^64s^2$ von Nickel. Unsere Theorie, die auf die Einbeziehung der Korrelationen durch ein Vielteilchenverfahren zielt, lässt sich auch für andere Elemente (z.B. CoO, FeO) anwenden, so dass nur wenige Systeme, nämlich solche mit einer d^5 Konfiguration oder mit offener f-Schale (noch) nicht durch unsere Theorie erfasst werden können.

Wir betrachten die Bandlücken-Zustände von NiO und vernachlässigen deren Dispersion.

Zuerst werden die Zwei-, Drei-, und Vierteilchenfunktionen bestimmt, die die angeregten Zustände eines Nickelions beschreiben. Diese Funktionen bilden die Basis für unseren Hamiltonoperator, der eine volle Kugelsymmetrie besitzt. Danach führen wir ein Ligandenfeld ein, damit die Symmetrie schrittweise auf kubische Symmetrie (Volumen des kubischen Kristalls) und Quadratsymmetrie (Oberfläche des Kristalls) reduziert wird. Die Werte der Ligandenfeldparameter erhalten wir durch eine Anpassung an die experimentellen Werte der Energie. Der Hamiltonoperator beschreibt dann die angeregten Zustände einer NiO-Oberfläche und dient zur Ableitung der nichtlinearen Spektren dieses Materials.

Die Ergebnisse dieser Methode zeigen, dass die nichtverschwindenden Tensorelemente *linear* im antiferromagnetischen Ordnungsparameter sind. Die Spektren weisen einige für nichtlineare Optik günstige Linien auf, dazwischen auch solche, die für Magneto-Optik gebraucht werden. Die Tensorelemente sind von gleicher Größenordnung, was gute Möglichkeiten zur Domänenabbildung bietet.

Antiferromagnetische Spindynamik: Die Weiterentwicklung dieser elektronischen Beschreibung in Hinblick auf dynamische Phänomene ermöglicht die experimentelle "pump-probe"-Methode der Laseroptik zu simulieren. Dazu präparieren wir das System in einem

hoch-angeregten Anfangszustand. Dieser Anfangszustand entwickelt sich zeitlich gemäß der Schrödingergleichung. Diese Entwicklung erfordert ein quantenmechanisches Verfahren. Anschließend berechnen wir den nichtlinearen optischen und magnetischen Response für jede feste spätere Zeit im Zeitfenster zwischen 0 und 500 fs.

Unsere Resultate beweisen eine schnelle Dynamik (innerhalb von Femtosekunden), ähnlich zu den früheren Ergebnissen für Metallen. Im Gegensatz zu jenen Ergebnissen, dauert die Kohärenz des angeregten Zustandes in NiO bis in den Pikosekunden-Bereich. Ein solches Verhalten wurde als charakteristischer Vorteil von Halbleitern angesehen. Die antiferromagnetischen Metalloxide zeigen den gleichen vorteilhaften Zeitverlauf, bedürfen jedoch keiner Spin-Injektion, weil sie eine hohe permanente Ladungs- und Spindichte besitzen, und können daher trotz langlebiger Kohärenz schneller als Halbleiter geschaltet werden.

Diese Ergebnisse lassen uns feststellen, dass antiferromagnetische Übergangsmetalloxide viele reizvolle und für künftige Anwendungen wichtige Merkmale besitzen, und dass die optische Frequenzverdopplung eine einzigartige Methode ist, um diese Merkmale zu untersuchen.

Streszczenie

Niniejsza praca zawiera teoretyczny opis generacji drugiej harmonicznej fali świetlnej (SHG) na powierzchni antyferromagnetycznych tlenków metali.

Nowe dziedziny technologii, jak magnetyczne pamięci komputerowe lub obliczenia kwantowe, wymagają nowych materiałów. Na przykład, element TMR (tunneling magnetoresistance), przewidziany jako część nowych pamięci komputerowych, jest zbudowany z "kanapki" trójwarstwowej, gdzie warstwa środkowa składa się z tlenku metalu. Magnetyczne właściwości tego (często antyferromagnetycznego) tlenku wpływają na działanie całego elementu, zatem badanie magnetycznej struktury warstwy środkowej ma duże znaczenie. Wygodną metodą do badania takich głębiej położonych warstw tlenków jest optyczna generacja drugiej harmonicznej (SHG). W związku z tym, bardzo ważne jest rozwinięcie teorii opisującej to zjawisko i pozwalającej precyzyjnie przewidzieć wyniki przyszłych eksperymentów na takich strukturach.

Fakt, że SHG zachodzi tylko na powierzchniach został już potwierdzony doświadczalnie, jako że powierzchnia materiału łamie symetrię środkową. Z drugiej strony, pojawiły się interesujące prace eksperymentalne dotyczące obrazowania domen antyferromagnetycznych z objętości materiałów, które nie posiadają środka symetrii (Cr_2O_3). W związku z tym powstaje pytanie, czy SHG jest zdolna badać strukturę magnetyczną *powierzchni* takich antyferromagnetyków, które (jak np. tlenek niklu NiO) posiadają środek symetrii. Na to pytanie odpowiada niniejsza praca.

Wiele eksperymentów na *ferromagnetycznych* metalach wykazało różnymi optycznymi metodami zmniejszenie się magnetyzacji w czasie krótszym niż pikosekunda, jak również odstępstwa od zachowania przewidywanego przez teorię cieczy Fermiego (zmiana magnetyzacji nie odbywa się przy udziale sieci krystalicznej). Oczekuje się, iż *antyferromagnetyczne* powierzchnie tlenków wykażą równie interesujące zjawiska w zakresie femtosekund, stosownie do spodziewanych zastosowań ultraszybkich procesów w magento-elektronice. Powierzchnie tlenków nadają się szczególnie do badania dynamiki spinów w skali femtosekund, ponieważ: (i) mają bogaty diagram fazowy, (ii) prezentują system o dużej gęstości stanów (przy istotnej roli korelacji elektronowych) i o dużej przerwie energetycznej, (iii) na granicy metal - tlenek może zachodzić odpływ ciepła (generowanego przez laser) z intensywnością wystarczającą do tego, aby wzrost temperatury nie wpłynął na właściwości tlenku.

Dlatego wybraliśmy materiał o prostej budowie krystalicznej, który jednakże umożliwia studia nad zdolnością SHG do badania samej powierzchni *oraz* nad wpływem korelacji. Należy zaznaczyć, że metody przedstawione w tej pracy jak i wyniki w niej uzyskane mogą

zostać przeniesione na inne tlenki metali przejściowych.

Analiza symetrii. Pierwsza część pracy (rozdział 2) poświęcona jest analizie optycznej generacji drugiej harmonicznej z powierzchni antyferromagnetycznych tlenków z punktu widzenia teorii grup. Dotychczasowe prace dotyczące klasyfikacji (z punktu widzenia teorii grup) antyferromagnetycznych struktur spinowych w *objętości* kryształów zostawiają pewną lukę koncepcyjną między przewidzianymi elementami tensora z jednej strony, a oczekiwanymi rezultatami eksperymentalnymi z drugiej. Biorąc pod uwagę, że domeny w objętości antyferromagnetyka zostały zwizualizowane dopiero w 1994 roku, że pochodzenie kontrastu między SHG z różnych domen nie zostało jeszcze wyjaśnione na gruncie analizy symetrii (a co dopiero teorii elektronowej), staje się jasne, że jeszcze wiele jest otwartych pytań nawet na poziomie analizy symetrii antyferromagnetycznych powierzchni. Na niektóre z tych pytań odpowiada niniejsza praca. W przeciwieństwie do dotychczasowych analiz antyferromagnetyzmu w objętości kryształów, nasza praca koncentruje się na prostych powierzchniach sześciennych antyferromagnetyków. Używamy przybliżenia dipola elektrycznego. Stosujemy metody teorii grup aby określić nieznikające elementy tensora $\chi_{el}^{(2\omega)}$ dla różnych powierzchni o uporządkowaniu antyferromagnetycznym. Liczba odróżnialnych konfiguracji spinowych zależy od orientacji badanej powierzchni. Ponadto uwzględniamy zniekształcenia sieci krystalicznej atomów magnetycznych oraz niemagnetycznych, badamy też wpływ obecności dwóch rodzajów atomów magnetycznych. Ten ostatni aspekt ma związek z przewidywanymi (na podst. eksperymentów z nadprzewodnikami wysokotemperaturowymi) odstępstwami od stechiometrii w tlenkach metali przejściowych (wakancje tlenowe).

Nasze wyniki wykazują, że w różnych konfiguracjach spinowych występują różne nieznikające elementy tensora $\chi_{el}^{(2\omega)}$. W ten sposób SHG umożliwia nie tylko odróżnienie antyferromagnetycznej *fazy* materiału od fazy para- lub ferromagnetycznej, ale również (w wielu wypadkach) identyfikację dokładnej *struktury spinowej*. Wspomniane zniekształcenia również dają się wykryć przy pomocy SHG.

Innym ważnym rezultatem naszej pracy jest przewidzenie możliwości wizualizacji domen antyferromagnetycznych na *powierzchni* kryształów o strukturze sześcianu. Wizualizacja ta może być dokonana bez udziału wiązki odniesienia, w odróżnieniu od materiałów jak YMnO_3 . Zaproponowana przez nas metoda korzysta z faktu, iż niektóre elementy tensora zmieniają znak przy przejściu z jednej domeny do drugiej, podczas gdy inne elementy pozostają bez zmian. To powoduje pojawienie się składnika interferencyjnego w odbitym świetle SHG. Ta interferencja prowadzi do kontrastu między domenami.

Ważnym przyczynkiem do klasyfikacji nieliniowej optyki z punktu widzenia symetrii, przedstawionym w tej pracy, jest uważana analiza roli operacji odbicia czasu. Dotychczas traktowano tę operację jako równoważną odwróceniu magnetyzacji. W wielu wypadkach wewnętrzne pole magnetyczne próbki było traktowane inaczej niż pole fali elektromagnetycznej przez nią propagującej, przez to zostało utracone rozróżnienie między “symetrią odbicia czasu” a “dwukierunkowością” (reciprocity). Nasza analiza wykazuje, że brak dwukierunkowości (non-reciprocity) jest skutkiem tego, iż światło oddziałuje różnie na momenty magnetyczne o różnej orientacji, natomiast operacja odbicia czasu wpływa na *oba* elementy, tj. propagację światła i magnetyczne uporządkowanie próbki. Ten fakt jest

szczególnie ważny dla SHG z antyferromagnetyków, gdyż (i) odbicie czasu nie koniecznie odwraca parametr uporządkowania antyferromagnetycznego oraz (ii) w SHG nie występuje dyssypacja w sensie przekształcania energii promienistej w ciepłą. Jednakże występuje inny rodzaj dyssypacji, który odpowiada redystrybucji częstotliwości światła, i to właśnie powoduje asymetrię odbicia czasu w SHG. Wnioskujemy z tego, że SHG jest procesem *dynamicznym* i w jego analizie odbicie czasu nie powinno być stosowane.

Ponadto, stosowanie operacji odbicia czasu w analizie symetrii prowadzi do nieprawidłowych wniosków odnośnie zespolonej fazy elementów tensora. Te wnioski (różnica fazy między magnetycznymi i niemagnetycznymi elementami równa 90°) nie są potwierdzone przez teorię elektronową oraz fałszują rozważania dotyczące eksperymentalnej wizualizacji domen. Nasza teoria nie posiada takich wad.

Teoria elektronowa. Bazując na wynikach naszej analizy symetrii rozwinęliśmy formalizm do opisu stanów silnie wzbudzonych w NiO (rozdział 3 pracy). Bierzemy pod uwagę elektronowe konfiguracje niklu $3d^8$, $3d^7 4s$, i $3d^6 4s^2$. Nasza teoria, która uwzględnia korelacje elektronowe poprzez użycie stanów wielocząstkowych, może być łatwo przystosowana także do innych substancji (np. CoO, FeO). Na obecnym etapie nasza teoria nie daje się zastosować do opisu nielicznej klasy materiałów, mianowicie tych w których występują konfiguracje d^5 oraz tych z otwartą powłoką f. Istnieją jednak możliwości rozszerzenia tego opisu, aczkolwiek nie zajmujemy się tym w niniejszej pracy.

Używamy stanów leżących w przerwie energetycznej NiO, zaniedbując ich dyspersję.

Najpierw określamy funkcje falowe dwu-, trzy-, i cztero-cząstkowe, które opisują stany wzbudzone jonu niklu. Te funkcje tworzą bazę dla naszego Hamiltonianu, który posiada pełną symetrię sferyczną. Następnie wprowadzamy pole ligandów, aby stopniowo zredukować symetrię do sześcienną (objętość kryształu) i kwadratowej (powierzchnia kryształu). Wartości parametrów pola ligandów otrzymujemy przez dopasowanie do doświadczalnych wartości energii. Wówczas Hamiltonian opisuje stany wzbudzone na powierzchni tlenku niklu i służy do otrzymania nieliniowego spektrum tego materiału.

Wyniki tych obliczeń pokazują, że nieznikające elementy tensora są *wprost proporcjonalne* do antyferromagnetycznego parametru uporządkowania. Spektra ukazują linie widmowe przydatne dla optyki nieliniowej, w tym takie, które się szczególnie nadają dla magneto-optyki. Elementy tensora są tego samego rzędu wielkości, co jest korzystne dla wizualizacji domen antyferromagnetycznych.

Antyferromagnetyczna dynamika spinów. Rozwinięcie wyżej przedstawionego elektronicznego formalizmu w kierunku zjawisk dynamicznych umożliwia symulację metody doświadczalnej zwanej “pump-probe”. W tym celu przygotowujemy stan silnie wzbudzony systemu w chwili początkowej. Ewolucja tego stanu początkowego zachodzi według równania Schrödingera, jest to więc proces typowo kwantowo-mechaniczny. Następnie obliczamy nieliniową magneto-optyczną odpowiedź systemu dla każdej ustalonej chwili między 0 a 500 fs.

Nasze rezultaty potwierdzają szybką dynamikę (zachodzi w ciągu femtosekund), podobną do wcześniejszych wyników symulacji dla metali. W przeciwieństwie jednak do tamtych wyników, koherencja odpowiedzi magneto-optycznej stanów wzbudzonych w NiO trwa aż do reżimu pikosekund. Dotychczas takie cechy dynamiki były znane dla półprzewodników.

Antyferromagnetyczne tlenki metali wykazują podobne, korzystne dla zastosowań cechy, lecz dodatkowo nie wymagają iniekcji spinów, gdyż posiadają trwale wysoką gęstość spinów i ładunków.

Te wyniki pozwalają nam stwierdzić, iż antyferromagnetyczne tlenki metali przejściowych posiadają cechy bardzo istotne z punktu widzenia przyszłych zastosowań, oraz że optyczna generacja drugiej harmonicznej jest unikalną metodą do badania tych właściwości.

Summary

This work contains the theoretical description of the optical Second Harmonic Generation from antiferromagnetic oxide surfaces.

New technology fields, such as magnetic computer memories (MRAMs) or quantum computing, require new materials. For example, a tunneling magnetoresistance (TMR) element, proposed as a part of the new computer memories, has a trilayer structure. The central layer consists of an oxide sandwiched between a soft and a hard magnetic layer. Magnetic properties of this (often antiferromagnetic) oxide influence the performance of the whole component, thus investigations of the magnetic structure of this layer are of technological relevance. A useful method for investigation of such buried oxide interfaces is optical Second Harmonic Generation (SHG). Consequently, development of a theory to describe this phenomenon and to predict experimental response from such structures is of importance.

Surface sensitivity of SHG has been experimentally proven, since the presence of a surface breaks the inversion symmetry. On the other hand, there is a couple of experiments showing the possibility of antiferromagnetic domain imaging in the bulk of the materials without the center of inversion (Cr_2O_3). An important question is if SHG is also sensitive to antiferromagnetism at surfaces of cubic antiferromagnets, where, due to the preserved inversion symmetry in the bulk, SHG originates from surfaces only. An answer to this question is provided by this work.

Many experiments on *ferromagnetic* metals show by different optical methods a magnetisation decay within times shorter than a picosecond. It is predicted that *antiferromagnetic* oxide interfaces show equally interesting behavior, relevant to their expected applications in the magneto-electronic ultrafast processes. Oxide surfaces are particularly suited for the investigations of femtosecond spin dynamics, since: (i) they have a rich phase diagram, (ii) they exhibit high state density (with the important role of electronic correlations), (iii) heat transfer through the metal-oxide interface can be intensive enough to prevent the laser-generated heat from influencing the sample.

For these reasons we chose a material with a simple crystal structure which however allows for studying applicability of SHG to surface antiferromagnetism. It is necessary to point out that the methods used in this work as well as the results can be translated to other transition metal oxides.

Symmetry analysis. The first part of this work (Chapter 2) is devoted to group theoretical analysis of the SHG response from the surfaces of cubic antiferromagnets. Till now, the group theoretical classification of the antiferromagnetic spin structures in the *bulk*

leave a conceptual gap between the predicted tensor elements on one hand and expected experimental results on the other. Taking into account that the antiferromagnetic bulk domains were visualized only in 1994, and that the origin of the SHG domain contrast has not been explained from the symmetry point of view (to say nothing about an electronic description) it is clear that many questions on the level of the symmetry analysis remain open. This work answers some of these questions. We concentrate on low index surfaces of cubic antiferromagnets and restrict ourselves to the electric dipole approximation. We use group theoretical methods to determine the nonvanishing elements of $\chi_{el}^{(2\omega)}$ tensor for various antiferromagnetically ordered surfaces. The number of distinguishable spin configurations depends on the surface orientation. Moreover, we take into account distortions of the magnetic and nonmagnetic atom sublattices, we investigate also the influence of a second kind of magnetic atoms. This is related to the predicted non-stoichiometries (oxygen vacancies) in transition metal oxides.

Our results show that different spin configurations exhibit different nonvanishing elements of $\chi_{el}^{(2\omega)}$ tensor. In this way it is possible not only to distinguish the magnetic *phase* of the surface, but in many cases to identify the particular *spin structure*. The abovementioned distortions can be also detected by SHG.

Another important result of our work is the possibility of *surface* domain imaging. This can be done without the reference beam, in contrast to materials such as YMnO₃. The method proposed by us uses the fact that some tensor elements change sign from one domain to another, while other tensor elements remain invariant. This results in an interference component in the SHG response, which leads to the domain contrast.

An important contribution to the classification of the nonlinear optics from the symmetry point of view is the analysis of the role of time-reversal operation. Till now this operation has been treated as equivalent to magnetisation reversal. In many cases, the internal magnetic field of a sample has been treated differently than the field of the electromagnetic wave propagating through the sample. In this way a difference between “time-reversal symmetry” and “reciprocity” has been lost. Our analysis shows that non-reciprocity results from a different interaction of light with magnetic moments of a different orientation, while the time-reversal operation influences *both* elements, i.e. beam propagation and magnetic ordering of the sample. This fact is especially important for SHG from antiferromagnets, since (i) time reversal does not necessarily revert the antiferromagnetic order parameter and (ii) the dissipation in the meaning of conversion the radiative energy into heat is absent in SHG. There exists another type of dissipation, however, corresponding to the irreversible redistribution of optical frequencies, and exactly this causes the time-reversal asymmetry in SHG. We conclude that SHG is a *dynamical* process and time-reversal operation should be excluded from the analysis of this process.

Moreover, using time-reversal operation in the symmetry analysis leads to wrong conclusions concerning the complex phase of the tensor elements. These conclusions (complex phase difference exactly 90° between magnetic and nonmagnetic tensor elements) cannot be justified by an electronic calculation and lead to false predictions with respect to domain imaging. Our theory is free from these disadvantages.

Electronic theory. Based on the results of our symmetry analysis we developed a

formalism for the description of highly excited states in NiO (Chapter 3 of the work). We take into account Nickel electronic configurations $3d^8$, $3d^74s$, and $3d^64s^2$. Our theory takes into account correlations by use of many-body states and can be easily adapted to other, similar substances (e.g. CoO, FeO). At the current stage our theory cannot be applied to a limited class of materials, namely those with d^5 configuration and those with the open f shell. There are possibilities of extending our description, nevertheless our work does not concern them.

We use the gap states of NiO and neglect their dispersion.

First we determine the two-, three-, and four-body wavefunctions which describe the excited states of a Ni ion. These functions form a basis for our Hamiltonian, which exhibits a full spherical symmetry. Next we introduce a ligand field to reduce the symmetry to cubic (bulk material) and square (crystal surface). We fit the ligand field parameters to the experimental energy values. Then the Hamiltonian describes excited states at the NiO surface and allows for obtaining the nonlinear spectrum of the material.

The results show that the nonvanishing tensor elements are proportional to the antiferromagnetic order parameter. Spectra show lines suitable for nonlinear optics, also for magneto-optics. The tensor elements are of the same order of magnitude, which is favorable for the antiferromagnetic domain imaging.

Antiferromagnetic spin dynamics. An extension of this formalism towards dynamical phenomena allows for the simulation of a pump-probe experiment. For this purpose, we prepare a highly excited state of the system at the time $t=0$. The evolution of this initial state is governed by the Schrödinger equation, thus it is a typical quantum-mechanical process. Next, we calculate the nonlinear magneto-optical response for each fixed moment between 0 and 500 fs.

Our results confirm a fast dynamics (within femtoseconds), similarly to the earlier simulations for metals. In contrast to those results, however, the coherence of the magneto-optical response from the excited states in NiO lasts till the picosecond regime. Till now, these features have been known for semiconductors. Antiferromagnetic metal oxides show similar, favorable for applications features, but additionally do not require spin injection, since they possess a permanently high spin and charge density.

These results allow to conclude that antiferromagnetic transition metal oxides present features that are very important for the future applications, and that the optical Second Harmonic Generation is a unique method to address these features.

Erklärung

Hiermit erkläre ich, dass ich diese Dissertation selbstständig und ohne fremde Hilfe verfasst habe. Ich habe keine anderen als die angegebenen Quellen und Hilfsmittel benutzt. Die den benutzten Werken wörtlich oder inhaltlich entnommen Stellen habe ich als solche kenntlich gemacht.

Halle (Saale), den 6. März 2000

Lebenslauf

06.02.1974	geboren in Warszawa, Polen
1980-1988	Grundschule in Warszawa
1988-1992	J. W. Goethe Oberschule in Warszawa
1992-1997	Physikstudium an der Warschauer Polytechnik
1997	Diplomarbeit "Caracteristique d'une liaison optique-microonde" an der Universität Lille, Frankreich
01.09.1997-01.03.2000	Doktorand am Max-Planck-Institut für Mikrostrukturphysik in Halle (Saale)